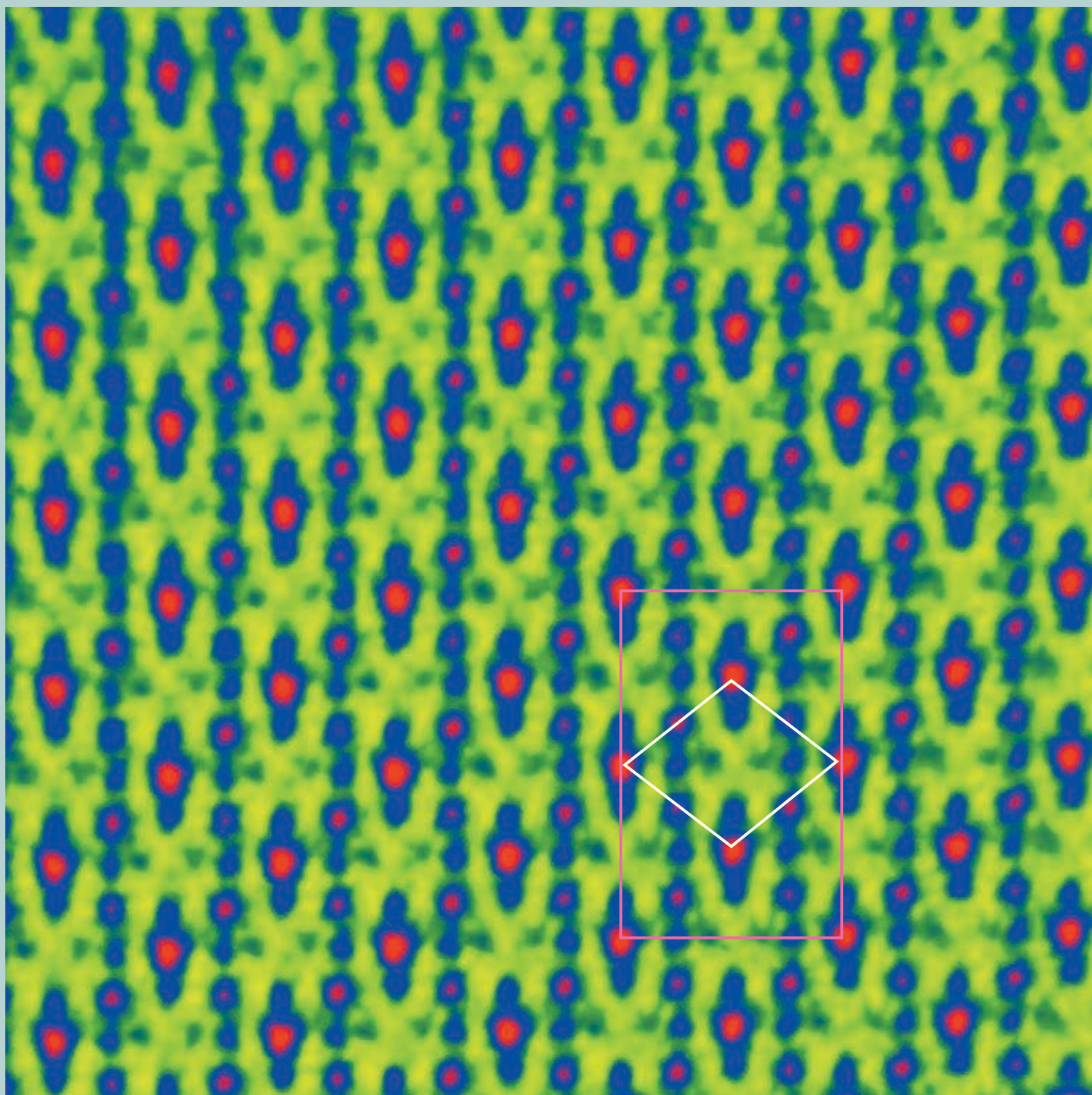


JEOL news

July 2010 Vol. **45** No. **1**



Lithium Atom Microscopy at Sub-50pm Resolution by R005

Contents

Lithium Atom Microscopy at Sub-50pm Resolution by R005	2
Atomic-Resolution Elemental Mapping by EELS and XEDS in Aberration Corrected STEM	8
Application of a Helium-Cooled Cryo-Electron Microscope for Single Particle Analysis	16
Ultrahigh-Resolution STEM Analysis of Complex Compounds	20
Development and Applications of a Frequency Modulation Atomic Force Microscopy for High-resolution Imaging in Liquids ..	24
JEM-2100: Applications in Nanotechnology	28
Development of JMS-S3000: MALDI-TOF/TOF Utilizing a Spiral Ion Trajectory	34
Rapid Characterization of Bacteria Using ClairScope™ and SpiralTOF™	38
Micro Area Analysis with JXA-8530F (FE-EPMA)	42
Analysis of Insulator Samples with AES	47

Cover micrograph

ABF (annular bright field) STEM image of LiV₂O₄ crystal with spinel structure, viewed from the [110] direction. Dots indicate vanadium (α - and β - sites), oxygen, and lithium columns. (See page 5)

K.Takayanagi[†], Y. Oshima^{††}, T.Tanaka[†], Y.Tanihshiro[†], H.Sawada^{†††}, F.Hosokawa^{†††}, T.Tomita^{†††}, T.Kaneyama^{†††}, and Y.Kondo[†]

[†] Department of Physics , Tokyo Institute of Technology

^{††} Department of Materials Science and Engineering, Tokyo Institute of Technology

^{†††} EM Business Unit, JEOL Ltd.

Introduction

To solve modern issues in materials sciences and nanotechnology, aberration corrected electron microscopy has yielded rich results, which could not be realized without a correction technique. Thus, aberration corrected (AC) electron microscopes is obviously becoming "conventional instruments" in transmission electron microscopy (TEM) [1] and scanning transmission electron microscopy (STEM) [2] for studies of materials and matter. As Feynman [3] and many scientists [4] have dreamed, imaging of individual atom is now reality, but visualizing individual atoms of light elements has yet to be resolved and localization of individual atoms (three dimensional imaging) in matrices has yet to be imaged.

Aberration corrected STEM can realize an electron probe as sharp as the diffraction limit, $0.61 \lambda/\theta$, where λ is the wavelength of the electrons and θ is convergent semi-angle of the probe, maximum of which had been determined by geometrical aberrations. Since the scattered intensity of an individual atom in molecules depends on the atomic number (light elements scatter with less intensity than heavy elements), a sharp probe enabled by aberration correction enhances imaging of atoms. Further technical developments of an aberration corrector can detect even individual lithium atom in matter, which has been elusive for electron microscopy and other experimental techniques.

Herein we report the development of a

new aberration corrected microscope* that achieves a sub-50 pm resolution [5]. The microscope with a cold field emission gun (CFEG) operates at 300 keV and can form a 46 pm electron probe with a 30 mrad semi-angle. This new electron microscope, which is named R005 (Resolution double oh five), has allowed us to detect various atoms; lithium, carbon, nitrogen, oxygen, silicon, arsenic, copper, germanium, silicon, gallium, tungsten, and gold in AC-STEM imaging.

New R005 microscope

Figure 1 shows the view of the new microscope, including the new cold-field emission gun (CFEG) and aberration correctors. A sub-50 pm resolution has been confirmed by imaging '47 pm separated' atomic columns in a germanium crystal [5]. **Figure 2** shows the STEM image, where the "dumbbell" image for the atomic columns along [114] are resolved. The observed image accords with the simulation, where the STEM probe has 46 pm FWHM; the coherent probe with the convergent semi-angle of 30 mrad is blurred by the incoherent Gaussian probe of 16 pm diameter. To compare the length scales, **Figure 3** displays high angle annular dark field (HAADF)-STEM images of the dumb-

*The project, named "development of a 50 pm resolution aberration-corrected EM for studies of phenomena in materials and matter" was conducted in collaboration with JEOL and Tokyo Tech. with the support of Japan Science and Technology Agency (JST).

[†] 2-12-1 H-51, Oh-okayama, Meguro-ku, Tokyo, 152-8551 Japan

takayang@phys.titech.ac.jp



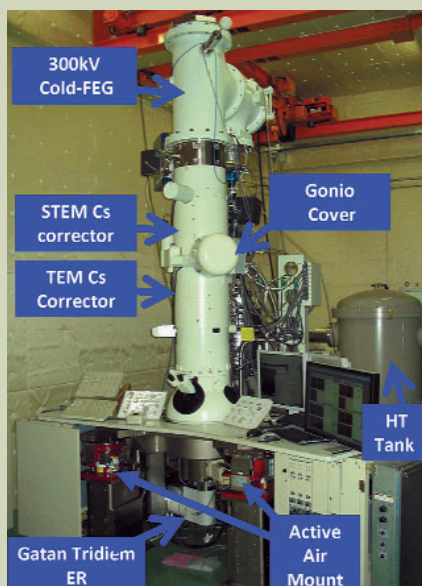


Fig.1 R005 microscope for STEM-TEM imaging at sub-50 pm resolution.

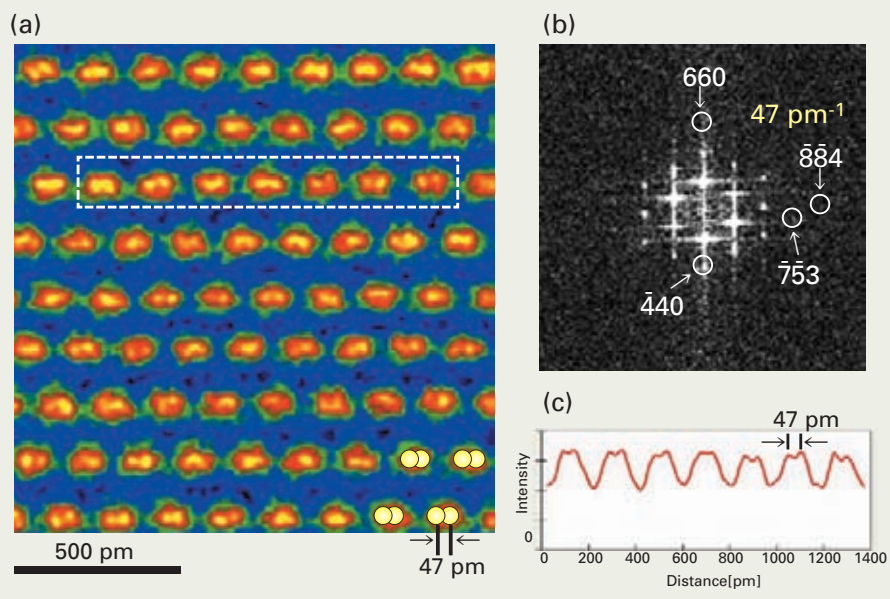


Fig.2 47 pm spaced dumbbell image of germanium crystal. Each dumbbell are the pair of the [114] atomic columns. (a) HAADF (high angle annular dark field) image, (b) Fourier transform of HAADF image, (c) intensity profile of the boxed area in (a).

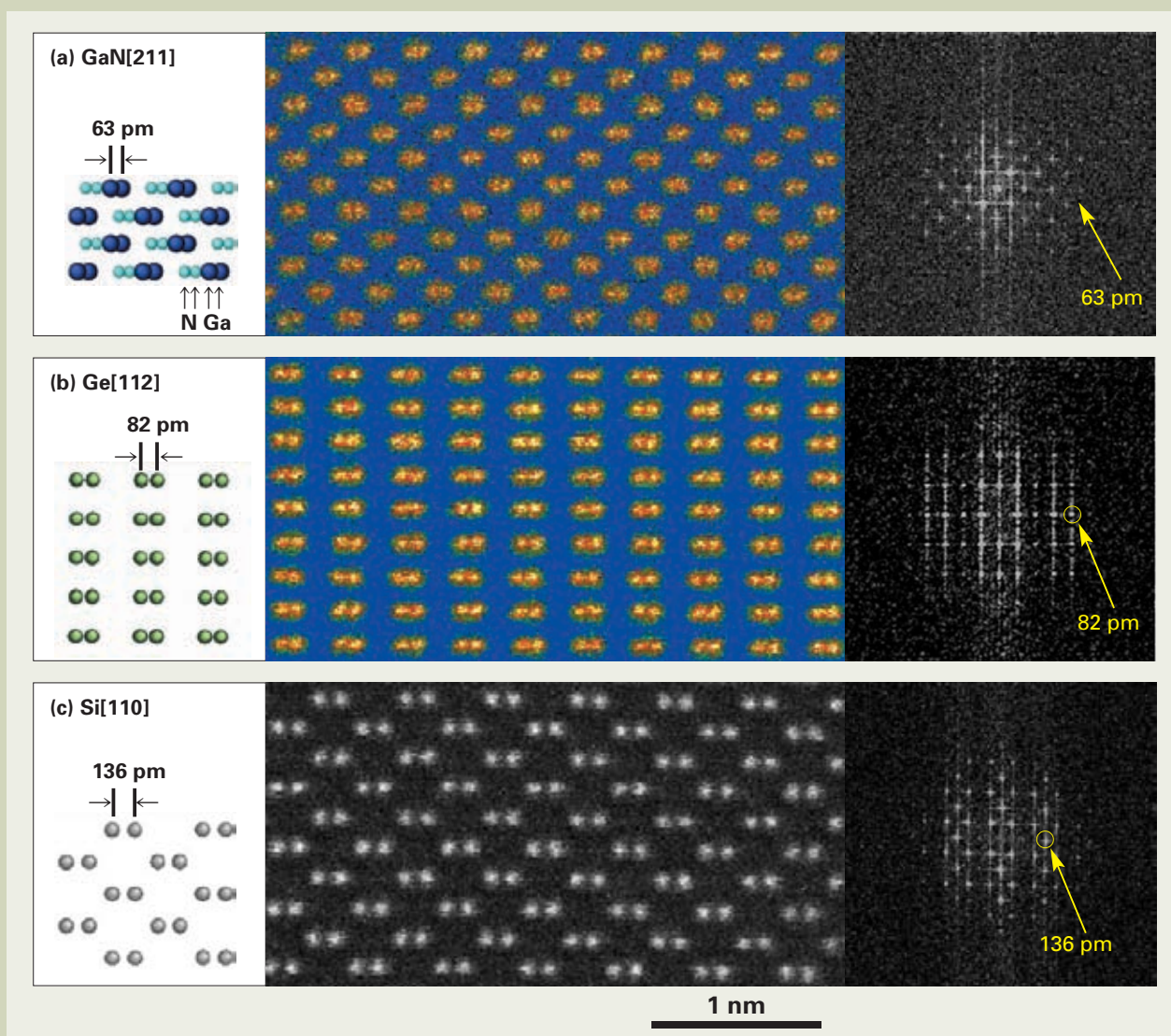


Fig.3 Dumbbell images of [hkl] atomic columns for (a) gallium nitride [211], (b) germanium [112] and (c) silicon [110]. Three panels are displayed with the same length scale; the spacing of the dumbbells are (a) 63 pm, (b) 82 pm, and (c) 136 pm.

bells for the '63 pm' separated [112] Ga columns in a GaN crystal [6], '82 pm' separated [112] germanium columns in a Ge crystal, and '136 pm' separated [110] silicon columns in a Si crystal.

The high performance of the R005 microscope is mainly due to the development of new spherical aberration correctors. The correctors are installed in both probe and image forming systems, namely STEM-Cs and TEM-Cs correctors. Both STEM and TEM Cs correctors have been newly designed to incorporate into the lens system of the microscope, which is dedicated for the present aberration correction system. Each of the aberration correctors is an asymmetrical dodeca-pole system, basically uses a hexapole field to correct spherical aberration as shown in Fig. 4. The asymmetric system allows us to reduce the higher order parasitic aberrations as well as increase of chromatic aberration generated in the transfer lens system resulting in the small increase of chromatic aberration ($\Delta Cc = 0.2$ mm) for probe and image forming systems.

A new automatic correction system has been developed to optimize the imaging condition [7]. The system (named Segmental Ronchigram Autocorrelation Matrix (SRAM)) uses Ronchigrams taken from an amorphous area of the specimen to find and correct the aberrations: Auto correlation functions obtained from several segments of the Ronchigram give quadric patterns correlated to the aberrations. The quadric patterns in segments are analyzed to estimate the aberration of the probe as shown in Fig. 5.

Development and design of a new CFEG, a microscope column, stable electronic circuits, and anti-vibration mechanical system have also contributed to the high performance of the R005 microscope. The new CFEG has achieved a constant emission current in excess of eight hours of continuous observations. The long-life and stable emission has enabled quantitative studies in quantitative imaging and in chemical analyses by EELS and EDS to be realized.

The R005 microscope has a new objective lens which has low chromatic aberration coefficients, $Cc = 1.65$ mm in probe forming system and $Cc = 1.54$ mm in image forming system, leaving a wide gap space of the objective pole-piece. Moreover, the objective lens is redesigned to observe specimens in aberration corrected STEM and TEM without changing the specimen height. More importantly, the R005 microscope allows any type of side-entry specimen holder that fits conventional JEOL electron microscopes (the models after JEM-2100F). Furthermore, the R005 microscope is capable of in-situ studies.

Lithium atom detection

Lithium atoms and ions have increasingly received interest due to their behaviors for applications in rechargeable batteries [8]. Although elaborate studies on TEM imaging of lithium atom columns [9, 10] have been conducted, lithium atoms and ions

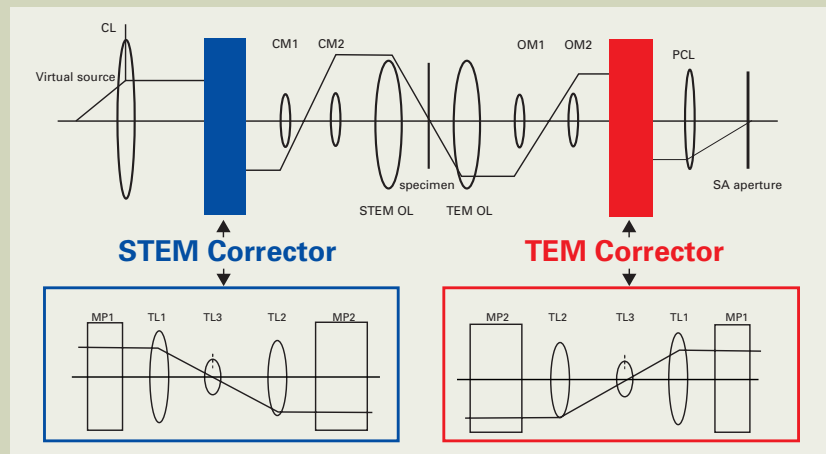


Fig.4 Asymmetric aberration corrector.

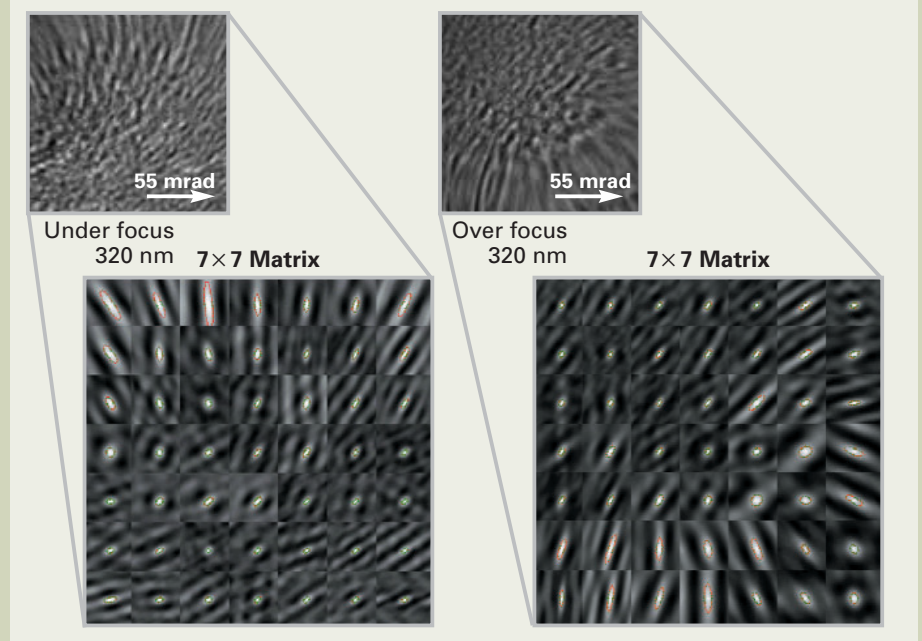


Fig.5 SRAM system for automatic aberration correction.

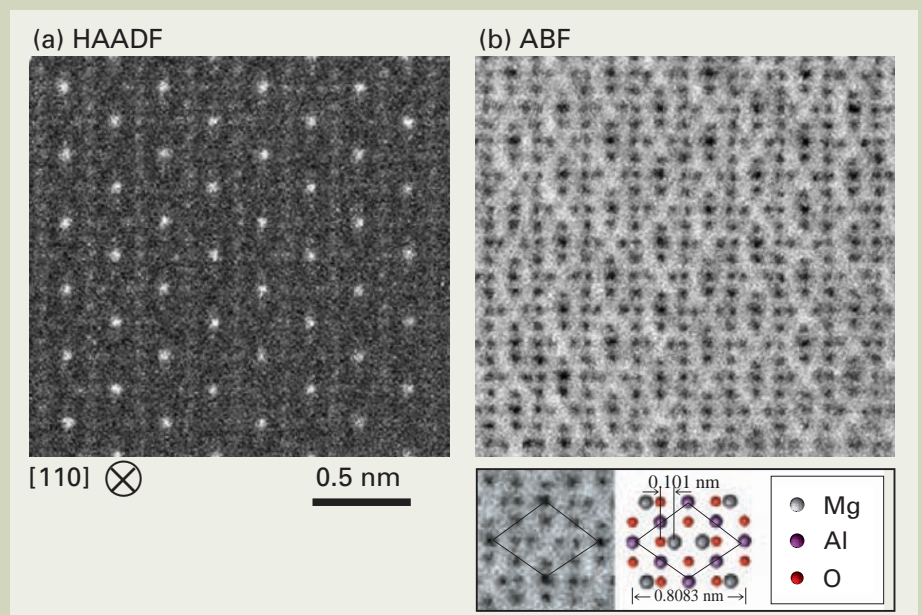


Fig.6 (a) HAADF image and (b) ABF (annular bright field) image of $MgAl_2O_4$. Inset shows the unit cell structure viewed along the [111] direction, and the corresponding ABF image, where magnesium ($Z=12$), aluminum ($Z=13$), and oxygen ($Z=8$) columns are resolved as dark dots. The separation between magnesium and oxygen columns is 0.101 nm.

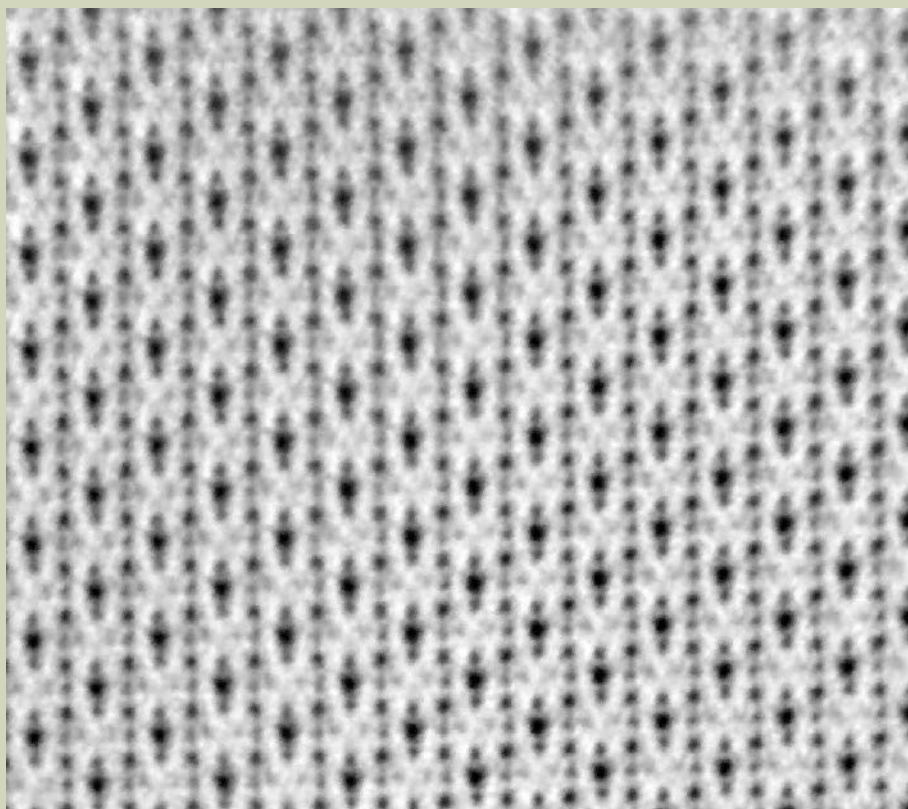


Fig.7 ABF (annular bright field) STEM image of LiV_2O_4 crystal, viewed from the $[110]$ direction. Dark dots indicate vanadium columns (α - and β -sites), oxygen columns, and lithium columns (see atomic structure model in Fig.8(c)). The lithium atomic columns are located at 0.1 nm separated from the oxygen column. Specimen becomes thick from the left to the right of the ABF image.

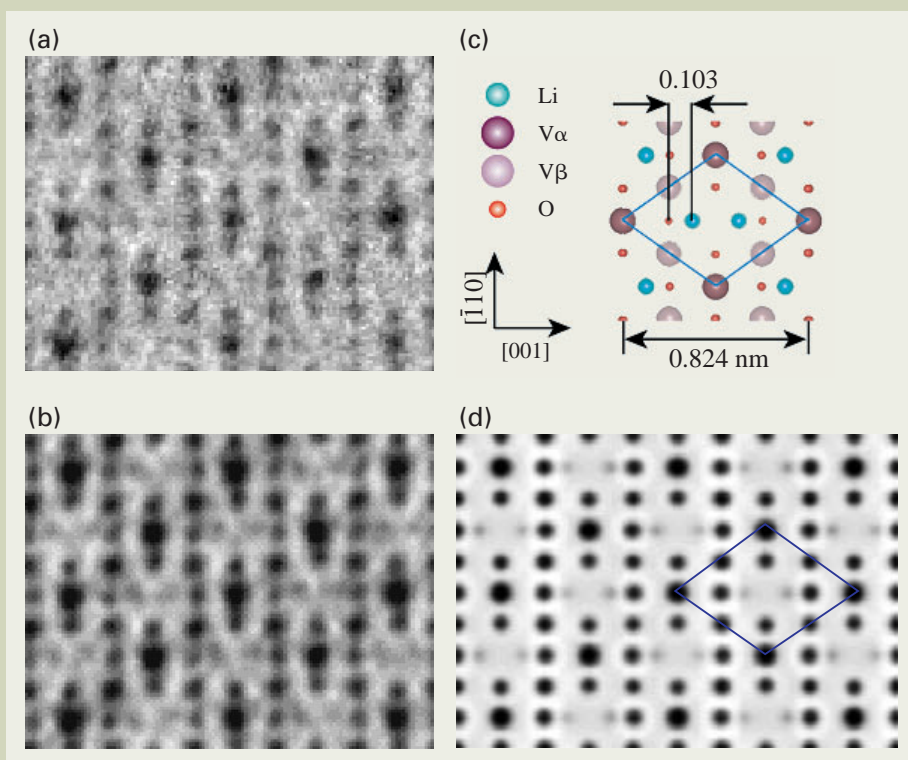


Fig.8 ABF images of LiV_2O_4 , (a) raw image and (b) processed image. (c) structure model, viewed from the $[110]$ direction. (d) multi-slice simulation of the model structure. Note that dark dots of the lithium columns are observable even in (a). The simulated image for specimen thickness of 3 nm reproduces ABF images overall in (a) and (b).

have yet to be detected one by one with electron microscopy. Herein we report STEM imaging of individual lithium atoms and detection of a few lithium atoms aligned in a column using the R005 microscope [11].

The R005 microscope with a new CFEG that enables a large convergent angle of the incident probe benefits annular bright field (ABF) STEM imaging, which is analogous, by reciprocity, to the bright field TEM using hollow-cone illumination [12]. **Figure 6** shows an ABF image of oxygen columns in MgAl_2O_4 crystal, where Mg, Al and O columns appear with different darkness after their atomic number difference as recent reports on ABF [13,14].

Figure 7 shows an ABF image of a LiV_2O_4 $[110]$ crystal with spinel structure (space group, $Fd-3m$) (cf. Fig. 8(c)). In this view, each dark dot is the image of the $[110]$ atomic column aligned parallel to the incident electron beam direction. Each column contains only vanadium (V), oxygen (O), or lithium (Li) atoms, so that the atomic species of the column can be determined from the darkness of the column image. In Fig. 7 the lithium atomic columns are observable. The image was processed by radial difference filter and low-pass frequency filter on the original raw image to eliminate impeditive noises. To demonstrate that the present filtering does not cause artifacts on the raw image, but reduce the speckled noise of the background, **Figs. 8(a)** and **(b)** show the raw image and the filtered image, respectively, while **Figs. 8(c)** and **(d)** show the structure model and the simulated image at a 3 nm thickness, respectively. The positions of dark dots agree well with the projected structure of LiV_2O_4 and the simulated image. The simulation reproduces the observed intensity profile as given in Ref [11], although the oxygen columns are not as intense as theoretically predicted.

The ABF and annular dark field (ADF) images, observed simultaneously, were simulated by multi-slice calculations [15,16] to determine specimen thickness in the observation area varying from zero to 3 nm. The ABF images in **Figs. 8(a)** and **(b)** are reproduced well by the simulated image for a specimen thickness of 3 nm. Assuming 3 nm thickness, the estimated number of lithium atoms is five, because the lithium atoms are aligned every 0.58 nm after the model structure in Fig. 8(c). Surprisingly, lithium columns in Fig.7 are visible at thinner area than Fig.8. At such a thin area below 2 nm thickness, each column can contain only a few lithium atoms.

The lithium column and oxygen column are separated by 0.1 nm (c.f., Fig. 8(c)). Thus, the 50 pm resolution is critical for lithium imaging. Therefore, without the present CFEG, which provides a small Gaussian probe of 16 pm diameter, lithium atomic column imaging is not possible. Although aberration correction can improve resolution, a large source size like a Schottky emitter can blur the image and reduce image contrast of the lithium column (see, discussion in ref [5]).

The R005 microscope with a new CFEG has an imaging capability of a few lithium atoms in ABF-STEM, and is promising for lithium microscopy and microanalysis.

Arsenic dopant detection in silicon crystal

The localization and inhomogeneity of atoms and clusters in materials have been the subjects of research for decades [17], because they become more dominant in controlling the materials properties as the length scale decreases. Except for SIMS (secondary ion mass spectroscopy) and ATP (atom probe), few methods are capable of visualizing the three-dimensional distribution of atoms. Here we demonstrate the visualization of individual arsenic dopant atoms in a silicon crystal using AC-STEM. Because high-speed, high-density and economic feasibility are always issues in silicon based transistors, and three-dimensional distribution of arsenic dopants in silicon-based transistors have long been of major interest. Thus, a key to visualizing dopant atoms in silicon devices, which have commercial and research gate lengths of 45 nm and 20 nm, respectively, is to determine how dopants are distributed and how they are clustered to give rise to localization and inhomogeneity. The performance of the R005 microscope should be capable of detecting individual arsenic dopants, although antimony and other heavy dopants have already observed by the STEM [18,19].

Figure 9 schematically depicts how a 50 pm probe receives signals from a dopant atom substituted at the silicon crystal. Additional scattering signals due to the replacement of a silicon atom by a heavy atom is detected in the HAADF images; the

scattering signal is intense when the 50 pm probe is focused at (or slightly above) the dopant. Thus, columns with a high intensity, provide a location map of the dopant atoms [20]. Here, CFEG with a small source is critical, because the Gaussian probe size of the source blurs the STEM images [21, 22].

Figure 10 shows a HAADF image [16] of a silicon crystal doped with arsenic atoms at a concentration of $10^{20}/\text{cm}^3$ (6%), viewed from the [100] direction of the silicon crystal. Thus, the bright dots correspond to the atomic columns arranged into a square lattice with ~ 0.2 nm spacing. The rainbow colors denote the intensities where red (most intense) discriminates columns with a single arsenic atom around the focal point. The red-colored columns indicate that some neighboring pairs have particular arrangements for the dopant clusters illustrated in **Fig. 11**. For example, the red-pair with the 2nd nearest neighbor distance in Fig. 10 represents the DP2 cluster [23] illustrated in Fig. 11. Figure 10 has a new arrangement, where the pair that looks like the letter 'L', two steps horizontally and one step vertically (or two steps vertically and one step horizontally), represents the FDP cluster [24]. Thus, arsenic dopants in a silicon crystal have been detected. Both CFEG and the high performance of the objective lens of the R005 electron microscope aid in this successful detection which has never been done before.

Single atom detection

Detection of atoms and/or adsorbed atoms

on a surface is of interest, particularly in catalysis and crystal growths. The R005 microscope has detected individual atoms of silicon, copper, germanium, silver, tungsten, and gold deposited on an amorphous carbon surface in HAADF-STEM. TEM has also imaged individual atoms, i.e., carbon atoms in a graphene sheet. Here we demonstrate TEM imaging of gold atoms and particles deposited on an amorphous carbon film.

Figure 12 shows a high resolution TEM image of gold deposits observed by the R005 microscope. Isolated atoms, clusters and particles are clearly detected. This image, a shot at the in-focus imaging condition, demonstrates "real" existence of gold atoms. The black dotted images that are dispersed around gold particles are single gold atoms. Their image intensity agrees with the multi-slice simulation. Dynamics of atomic motions are observable by AC-TEM through CCD camera systems. *In-situ* experiments in AC-TEM give rich information about dynamics of atoms and clusters, aided by the high performance of the R005 microscope.

Concluding Remarks

Aberration corrected electron microscopy with a sub-50 pm resolution has enabled individual atoms, including lithium atoms, to be detected. The advances of the R005 microscope include long-life CFEG, anti-symmetric AC, and an objective pole piece with a very low chromatic aberration. These

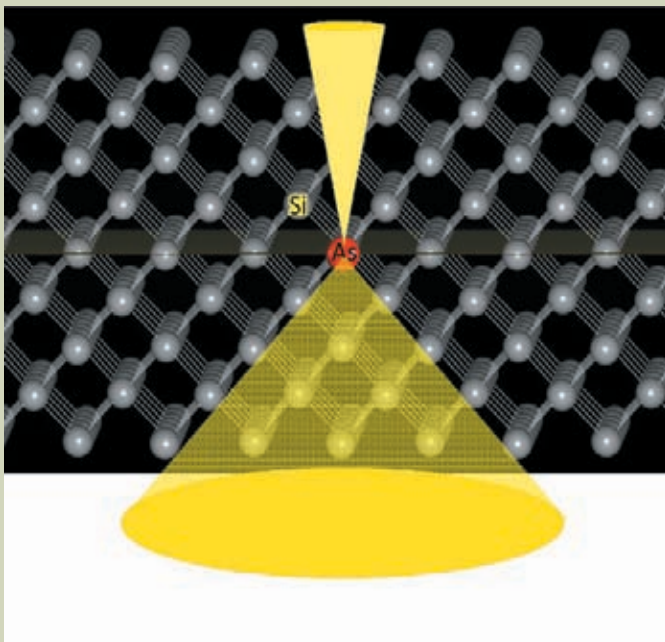


Fig. 9 Scheme of dopant imaging by AC-STEM.

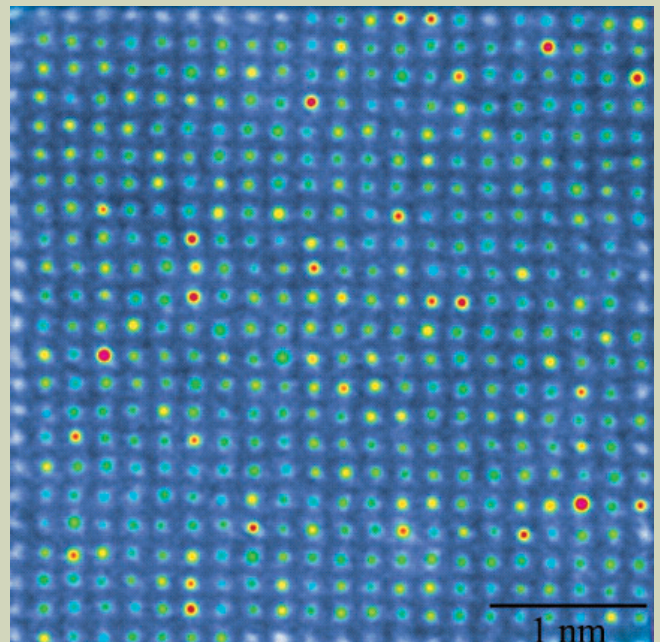


Fig.10 AC-STEM image of silicon crystal with arsenic dopants, viewed from the [001] direction. Intensities of the [001] atomic columns are displayed by rainbow color, where red color indicates the highest intensity. Atomic columns make square lattice of 0.2 nm spacing.

advances provide atomic imaging capability in both STEM and TEM modes of operation, which is the first step towards realizing hydrogen imaging.

Acknowledgements

The authors are grateful for collaborations with T. Ishizawa, M. Kawazoe, T. Sannomiya, and T. Nakamichi, during the development of the R005 microscope. Thanks are also to Y. Hashimoto, S. Kim, Y. Abe, Y. Gimbo, K. Sano, and N. Ohashi. This work was supported by CREST program from Japan Science and Technology Agency (JST).

References

- [1] Haider, M, et al: *Nature* **392**, 768 (1998).
- [2] Krivanek, O L, et al: Atom-by-atom structural and chemical analysis by annular dark-field electron microscopy, *Nature* **464**, 571 (2010).
- [3] Feynman R P: Feynman's 1959 talk "there's plenty of room at the bottom" available <<http://www.zyvec.com/nanotech/feynman.html>>
- [4] Crewe, A V: A system for the correction of axial aperture aberrations in electron lenses, *Optik* **60**, 271 (1982).
- [5] Sawada, H, et al: STEM imaging of 47 pm separated atomic columns by a spherical aberration corrected electron microscope with a 300 keV cold field emission gun, *J. electron. Micro.* **108**, 357 (2009).
- [6] Sawada, H, et al: Achieving 63 pm resolution in scanning transmission electron microscope with spherical aberration corrector, *Jpn. J. Appl. Phys.* **46**, L568 (2007).
- [7] Sawada, H, et al: Measurement method of aberration from Ronchigram by auto-correlation function, *Ultramicroscopy*, **108**, 1467 (2008).
- [8] Thackeray, M M, et al: Spinel electrodes from the Li-Mn-O system for rechargeable lithium battery application, *J. Electrochem. Soc.*, **139**, 363 (1992).
- [9] Rossell, M D, et al: Atomic-resolution imaging of lithium in Al_3Li precipitates, *Phys.Rev. B* **80**, 024110 (2000).
- [10] Shao-Horn Yang, et al: Atomic resolution of lithium ions in $LiCoO_2$, *Nat. Mater.* **2**, 464 (2003).
- [11] Oshima, Y, et al: Direct imaging of lithium atoms in LiV_2O_4 by spherical aberration-corrected electron microscopy, *J. Electron. Micro.*, **1**, 5 doi:10.1093/jmicro/dfq017 (2010).
- [12] Cowley J M: "diffraction physics" 3rd Revised Edition, North Holland Personal Library, pp.316 (1995).
- [13] Okunishi, E, et al: *Microsc. Microanal.* **15** (suppl 2), 164 (2009).
- [14] Findlay, S D, et al: *Appl. Phys.Lett.* **95**, 191913 (2009).
- [15] Hosokawa, F, et al: unpublished
- [16] Ishizuka, K: A practical approach for

STEM image simulation based on the FFT multislice method, *Ultramicroscopy* **90**, 71 (2002).

- [17] Asenov A: Random dopant induced threshold voltage lowering and fluctuations in sub 50nm MOSFETs: a statistical 3D 'atomistic' simulation study, *Nanotechnology* **10**, 153 (1999).
- [18] Voyles, P M, et al: Atomic-scale imaging of individual dopant atoms and clusters in highly n-type bulk Si, *Nature* **416**, 826 (2002).
- [19] Voyles, P M, et al: Imaging individual atoms inside crystals with ADF-STEM, *Ultramicroscopy* **96**, 251 (2003).
- [20] Oshima, Y, et al: Detection of arsenic dopant atoms in a silicon crystal using a spherical aberration corrected scanning transmission electron microscope, *Phys. Rev. B* **81**, 035317 (2010).
- [21] Klenov, D O, et al: Influence of orientation on the contrast of high-angle annular dark-field images of silicon, *Phys. Rev. B* **76**, 014111 (2007).
- [22] LeBeau, J M, et al: Quantitative atomic resolution scanning Transmission electron microscopy, *Phys. Rev. Lett.* **100**, 206101 (2008).
- [23] Chadi, D J, et al: Fermi-level pinning defects in highly n-doped silicon, *Phys. Rev. Lett.*, **79**, 4834 (1997).
- [24] Mueller, D C, and Fichtner, W: Highly n-doped silicon: deactivating defects of donors, *Phys. Rev. B* **70**, 245207 (2004).

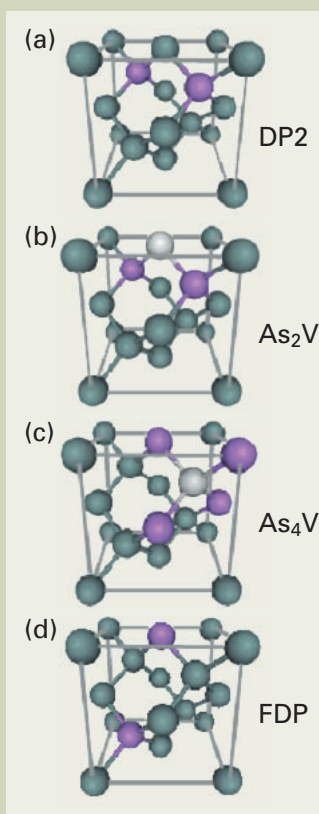


Fig.11 Structure models of arsenic dopant clusters, (a) DP2, (b) As₂V, (c) As₄V, and (d) FDP cluster.

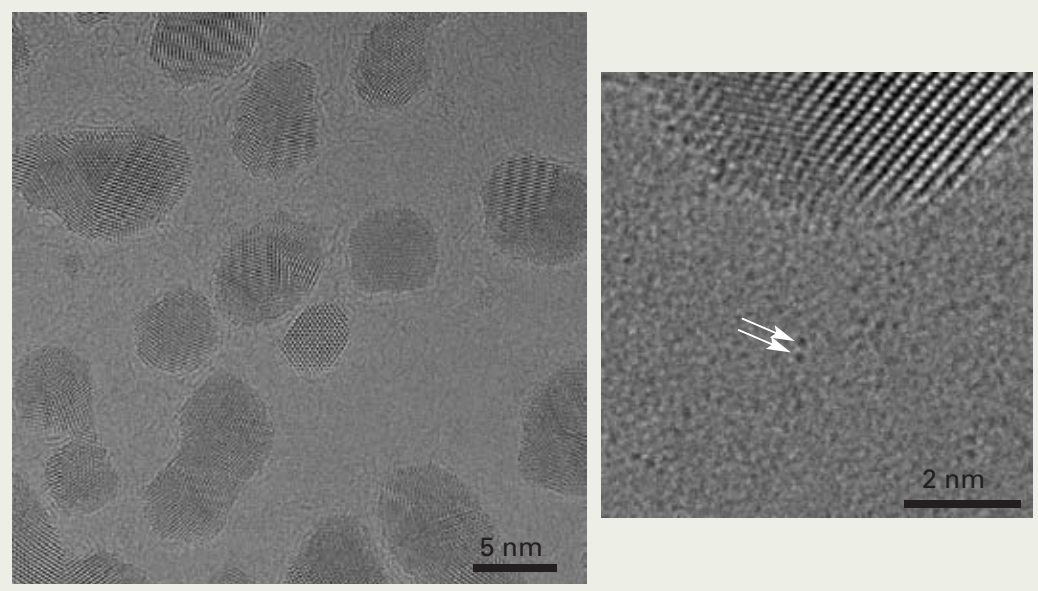


Fig.12 TEM image of gold atoms, clusters, and particles deposited on an amorphous carbon surface. Inset shows single gold atoms resolved clearly in the image.

Atomic-Resolution Elemental Mapping by EELS and XEDS in Aberration Corrected STEM

M. Watanabe[†], M. Kanno^{††} and E. Okunishi^{††}

[†] Department of Materials Science and Engineering / Center for Advanced Materials and Nanotechnology, Lehigh University

^{††} EM Business Unit, JEOL Ltd.

Recent improvements in aberration correction have brought tremendous advantages not only in high resolution imaging but also in high resolution analysis by electron energy-loss spectrometry (EELS) and X-ray energy-dispersive spectrometry (XEDS) in scanning transmission electron microscopy (STEM). Once the incident probe formation is optimized, atomic-resolution analysis can be performed by acquiring sufficient enough signals for appropriate chemical analysis while maintaining fine probe sizes. In addition, more sophisticated approaches of data acquisition and analysis, such as spectrum imaging (SI) and multivariate statistical analysis (MSA), are essential for atomic-resolution chemical analysis. In fact, it is possible to obtain atomic-resolution chemical images of materials since both the spatial resolution and analytical sensitivity are improved tremendously in combination of the aberration correction instrument with the advanced acquisition and analysis techniques. In this manuscript, the incident probe formation, data acquisition and data analysis are reviewed for atomic-resolution chemical analysis by EELS and XEDS in aberration-corrected instruments. Then, several applications of atomic-resolution chemical images obtained by the recently developed JEM-ARM200F aberration-corrected microscope are shown to address future trends in chemical analysis of materials.

Introduction

Chemical analysis at atomic-level spatial resolution with single-atom detection sensitivity is one of the ultimate goals in materials characterization. Such atomic-level materials characterization is now possible in the latest aberration-corrected electron microscopes. By aberration correction, image resolution has already reached half-Ångstrom levels by high-angle annular dark-field (HAADF) imaging in scanning transmission electron microscopy (STEM) and phase contrast imaging in transmission electron microscopy (TEM) [1, 2]. In addition, aberration-corrected STEM is also useful for chemical analysis by electron energy-loss spectrometry (EELS) and X-ray energy dispersive spectrometry (XEDS) since more probe current can be added into the aberration-corrected fine probe. Especially for EELS analysis, such higher beam currents may be sufficient to generate core-loss signals for reasonable analysis within a short acquisition time. Atomic-resolution EELS mapping has been already demonstrated in aberration-corrected STEM [3-5]. The aberration-corrected fine probe is also beneficial for XEDS analysis to analyze materials with improved spatial resolution of ~0.4 nm [6].

Elemental mapping in aberration-corrected

STEM/TEM is still limited by poor analytical sensitivity due to far much shorter acquisition time per pixel and to extremely small analyzed volumes. By simply increasing acquisition time, atomic-level resolution may be spoiled by spatial drifts of a specimen and/or an incident probe. Increased probe currents to improve analytical sensitivity result in degradation of resolution as the incident probe is enlarged with the current. Therefore, it is essential to optimize probe setting with an suitable probe currents for atomic resolution analysis. In addition, the poor analytical sensitivity can be offset by applying spectrum imaging (SI) in combination with advanced statistical approaches, such as multivariate statistical analysis (MSA). These methods succeed because the major noise components can be removed efficiently from spectrum acquired for a very short dwell time and then regular spectral processing is potentially applicable. The MSA noise reduction is also applicable to atomic resolution images as well.

In this paper, the optimum probe-formation is discussed first to perform atomic-resolution chemical analysis by EELS and XEDS in aberration-corrected instruments. Then, advantages to employ advanced SI and MSA approaches are demonstrated to extract unexpected information from datasets. Finally, several applications of atomic-resolution chemical images obtained by the recently developed JEM-ARM200F are shown to address future trends in chemical analysis of materials.

Optimum instrument settings for atomic resolution analysis

Spatial resolution in STEM imaging and analysis is directly related to an incident probe dimension; i.e., the shape and diameter in a certain fraction. Hence, the incident probe dimension is one of the most important factors in STEM. Most of the probe formation discussed in previous studies are focused on the geometric-aberration limited probe (dealt with a point source) and/or chromatic-aberration limited probe (which represent blurring of a point source). Note that the details about the geometric- and chromatic-aberration limited probe-formation can be found in the literature [e.g. 7-9]. Neither geometric- nor chromatic-aberration limited probe dimension contains any contribution of the finite source size (which is expressed through the source brightness and probe current). Therefore, the geometric- or chromatic-aberration limited probe sizes are useful only for operating conditions with a significantly limited probe current [10], such as high resolution HAADF-STEM imaging. However, for any analytical application by EELS and XEDS, the contribution of the finite source must be taken into account to probe formation since more currents are required to generate sufficient enough signals for appropriate EELS or XEDS analysis [6, 11]. In fact, the probe dimensions are enlarged as a function of the probe current.

5 E. Packer Ave., Bethlehem, PA 18015, USA.

masashi.watanabe@lehigh.edu

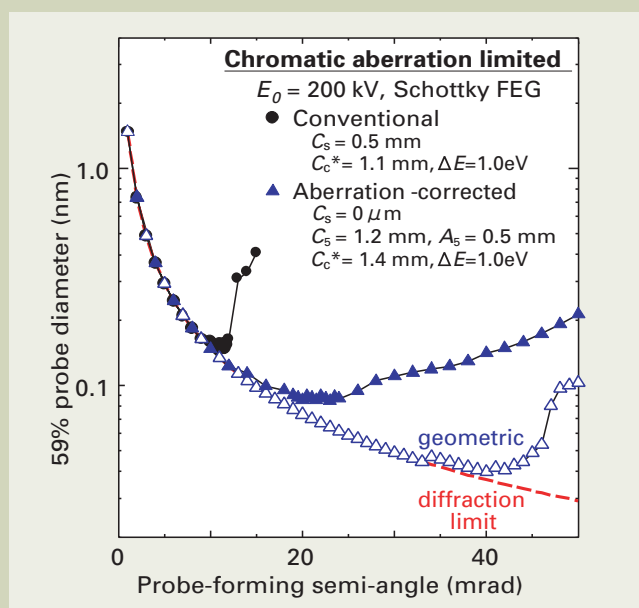


Fig. 1 Chromatic-aberration limited probe diameter contains 59% of the total intensity simulated for conventional and aberration-corrected 200 kV instrument with a Schottky FEG, plotted against the probe-forming semi-angle α . For comparison, the diffraction limit diameter and the geometric-aberration limited probe diameter in the aberration-corrected conditions are also plotted.

Hence, probe setting should be optimized carefully to maintain the high spatial resolution in atomic level with sufficient probe currents for better analytical sensitivity. Here, the optimum probe setting for atomic resolution analysis is discussed first [12].

Figure 1 shows the diameter containing 59% of total intensity $d(59\%)$, determined from the simulated intensity distribution of chromatic-aberration limited probe in conventional and aberration-corrected conditions for a 200 kV JEOL instrument equipped with a Schottky field-emission gun (FEG) source, which are plotted as a function of the probe-forming semi-angle, α . In the both conditions, the electron energy-spread (ΔE) of 1.0 eV that is a common value for the Schottky FEG was used. Note that the definition of $d(59\%)$ is originally derived from the Rayleigh criterion of intensity distribution in the aperture-diffraction limited probe, by which the image resolution can be defined as the minimum distance to distinguish the two point objects [9, 13, 14]. In the conventional condition, the simulation was performed for a 200 kV JEOL instrument with a ultra-high resolution pole-piece (the 3rd-order spherical aberration coefficient C_s of 0.5 mm and the chromatic aberration coefficient C_c^* of 1.1 mm). Even though these aberration coefficients are the best value available in commercial instruments without an aberration corrector, the major limit is the 3rd-order spherical aberration and the probe diameter can be at best 160 pm at $\alpha = 11$ mrad with a defocus of -28 nm. In contrast, the residual aberrations can be the 5th-order spherical aberration (C_5) and six-fold astigmatism (A_5) after complete aberration tuning in a CEOS hexapole-based corrector system [15, 16]. With the residual aberrations of $C_5 = 0.5$ mm and $A_5 = 1.2$ mm, the geometric-aberration limited probe size can reach to 40 pm at ~ 40 mrad as shown in Fig. 1 (open triangle). In the aberration-corrected condition, however, the major limitation can be the chromatic aberration and the optimum angle is reduced only to 23 mrad. Then, the optimum probe size is degraded to 85

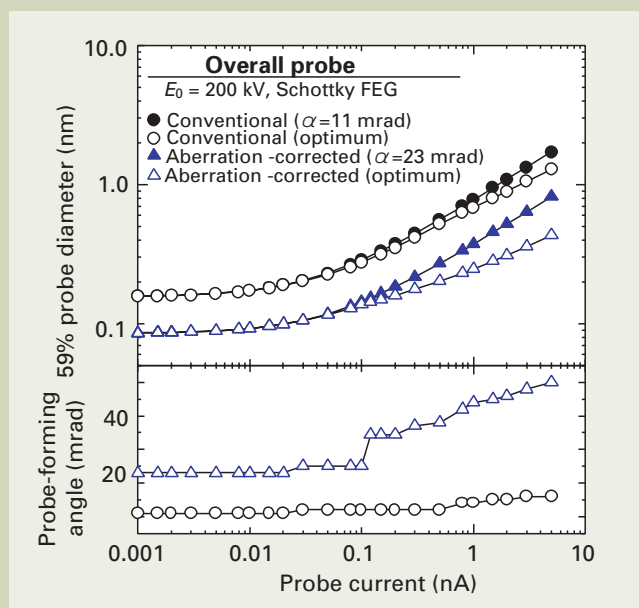


Fig. 2 Optimum angle for the overall probe in the conventional and aberration-corrected conditions summarized as a function of the probe current with the corresponding probe diameter $d(59\%)$ for the Schottky FEG [12].

pm from 40 pm due to the chromatic aberration. In this case, the probe diameter was determined with $\Delta E = 1.0$ eV and $C_c^* = 1.4$ mm (slightly increased due to the addition of aberration corrector).

As shown in Fig. 1, the optimum probe sizes are 160 pm at 11 mrad and 85 pm at 23 mrad in the conventional and aberration-corrected conditions, respectively. Again, these probe sizes are based on the chromatic-aberration limited intensity distribution and any contribution of the finite source size is not included. For analytical applications, the probe optimization should be performed with the probe current. The overall probe diameters at 11 and 23 mrad in both

conventional and aberration-corrected conditions (closed symbols) are plotted against the probe current in Fig. 2. The probe size is enlarged with an increase of the probe current in both conditions. In addition, the optimum overall diameters (open symbols) are also plotted in Fig. 2, which is calculated by determination of the optimum probe-forming angle. The optimum angle in the conventional condition is slightly increased with an increase of the current. Conversely, much larger probe-forming angle can be employed in the aberration-corrected condition especially when the probe current is higher than 100 pA, which is essential for EELS and XEDS analysis. Further details

about the probe optimization can be found elsewhere [12, 17].

Figure 3 shows simulated intensity distributions and extracted line profiles of the overall probes at probe currents of (a) 30, (b) 120 and (c) 500 pA in an aberration-corrected 200 kV instrument with a Schottky source. These selected probe currents are typical values for HAADF-STEM imaging, EELS analysis and XEDS analysis, respectively. The simulation was performed at optimum convergence angles for corresponding probe currents, as shown in Fig. 2. Both the intensity distributions and the profiles are normalized with the peak intensity at 500 pA. Therefore, the peak intensities at lower current conditions are correspondingly lower (i.e., ~57% at 30 pA and ~70% at 120 pA against the peak intensity at 500 pA). In the profiles, the normalized chromatic-aberration limited profiles are also plotted as dashed lines. At 30 pA, the dominant contribution is chromatic/geometric aberrations to the final probe formation. However, at higher currents for analysis applications, finite source size is the dominant factor for probe formation. Simulated $d(59\%)$ values at 30, 120 and 500 nA are 118, 152 and 220 pm, respectively.

Figure 4 shows HAADF-STEM images of Si<110> recorded at (a) 30, (b) 120 and (c) 500 pA in an aberration-corrected 200 kV JEOL JEM-2200FS STEM with a Schottky FEG at Lehigh. Intensity profiles extracted from the individual images are also inserted in Fig. 3. At 30 pA, the intensity reduction between the atomic column of the Si dumbbell reaches over 25%, which satisfies the Rayleigh criterion as described previously. The intensity reduction is slightly degraded at 120 pA, and no reduction can be observed at 500 pA. These experimental results are superimposed with the simulated $d(59\%)$ values as shown in Fig. 3.

For atomic-resolution chemical analysis, the probe optimization is the crucial factor. In addition, spatial resolution caused by the convolution of the incident probe with probe broadening must be maintained in atomic level. Since the beam broadening is strongly dependent on the specimen thickness, the spatial resolution should be evaluated as a function of the specimen thickness. In addition, since analytical signals of X-ray and energy-loss electrons are generated from the whole analyzed volume, it would be more appropriate to employ 90% of the total intensity rather than 59% for evaluation of the spatial resolution. In the evaluation, therefore, the selected incident probe diameters of 1.2 and 0.4 nm for the conventional and aberration-corrected cases, respectively, (which correspond to the $d(90\%)$ values in optimum probe-forming conditions at a current of 500 pA) are used. **Figure 5** shows the spatial resolution (90%) calculated for a Cu thin specimen in the conventional and aberration-corrected conditions at 200 kV based on the Gaussian probe broadening model [18-20], plotted against the specimen thickness. Obviously, a finer probe size in the aberration-corrected condition provides better spatial resolution. In the aberration-corrected condition, the spatial resolution remains below 1 nm for specimen thicknesses up to ~30 nm in pure Cu. More importantly, the spatial resolution can reach atomic dimensions below thicknesses of 20 nm. Conversely, thicker specimen > 50 nm in Cu

ends up with similar spatial resolution in both the conditions, which implies that there is no significant benefit to use an aberration-corrected STEM for improved spatial resolution if a thicker specimen is analyzed. For atomic resolution analysis, therefore, thinner specimens are essential. It should be noted that electron channeling was not taken into account for evaluation of spatial resolution. If a crystalline thin specimen is oriented near a highly symmetric zone axis, the incident probe-specimen interaction can be localized near a single atomic-column or surrounding neighbor columns due to the electron channeling, which may result in better spatial resolution rather than simple evaluation based on the Gaussian beam-broadening.

Advanced data acquisition and analysis procedures

As predicted above, thinner specimens are essential for atomic-resolution chemical analysis. This means that the analyzed volume is extremely restricted, and hence generated signals for appropriate analysis are also limited. In addition, signal fluctuations are not completely predictable in atomic resolution analysis as shown later. Therefore, advanced approaches for data acquisition and analysis are essential to detect such signal fluctuations from limited signals under relatively high noise in atomic reso-

lution analysis.

Spectrum imaging (SI) has been developed to expand and improve conventional elemental mapping [21, 22], which requires prior knowledge of the specimen to set particular energy windows. In SI, a full spectrum is continuously recorded at each pixel. Thus, the SI method offers post-acquisition treatments of elemental maps including regular spectral-processing methods, such as background subtraction and signal deconvolution. Therefore, it is possible to map out unexpected minor elements that are not even considered for mapping beforehand if the signals from such minor elements are successfully identified. However, for characterization of elemental fluctuations in atomic resolution, elemental mapping including SI in STEM still suffers from limited signals. Furthermore, there might be many variables even in a single SI dataset: some could be expected and others are totally unaware. It is essential to find out those variables in the dataset, which can be performed by employing multivariate statistical analysis (MSA).

The MSA method is a useful family of statistical-based techniques to analyze large datasets. The general concept of MSA is to reduce the dimensionality of an original large dataset by finding a minimum number of variables that describe the original dataset without losing any significant information [e.g., 23, 24]. This approach is useful for large, complicated data such as XEDS or EELS SI datasets,

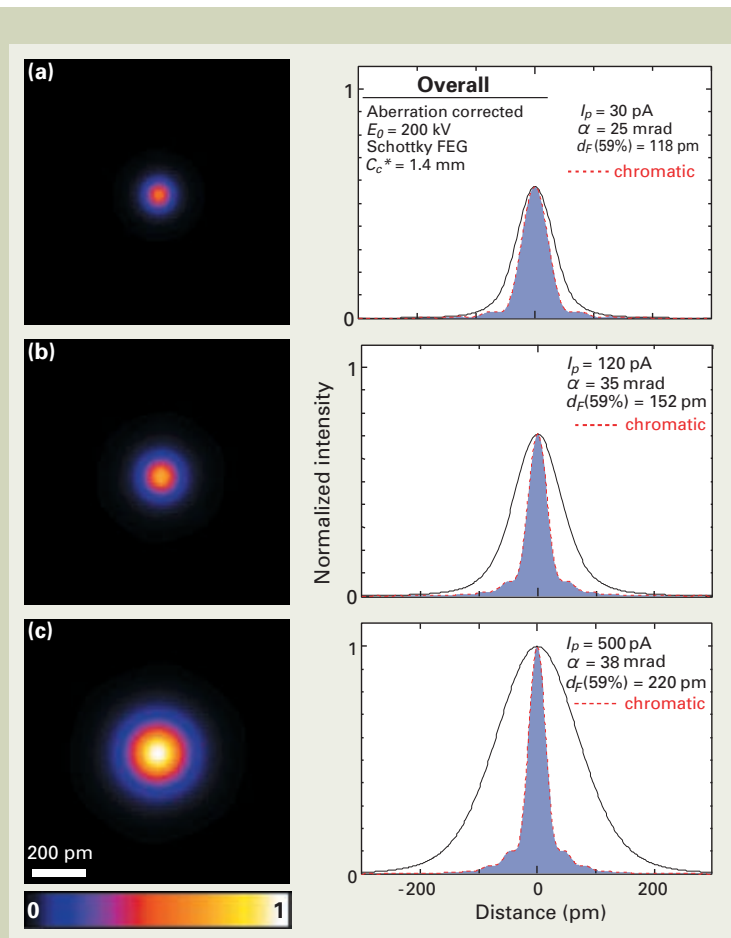


Fig. 3 Simulated intensity distributions and extracted line profiles of the overall probes at the probe currents of (a) 30, (b) 120 and (c) 500 pA in an aberration-corrected 200 kV instrument with a Schottky FEG. Normalized chromatic-aberration limited intensity profiles simulated at corresponding probe-formation conditions are also plotted as dashed lines in the profiles [17].

which has been successfully demonstrated by Koluta et al. [25].

For example, a STEM-EELS SI dataset was taken from SrTiO₃ in an aberration-corrected JEM-2200FS instrument at 200 kV. A HAADF-STEM image from a SrTiO₃ thin specimen is shown in Fig. 6(a) [26]. The bright and slightly darker spots in the image correspond to the Sr and Ti-O columns in the [001]-projected perovskite structure, respectively, and an EELS-SI data was acquired from the region indicated as a dashed square with 13×13 pixels for a dwell time of 0.1 s per pixel. Two spectra at the Sr and Ti-O column positions extracted from the SI are compared in Fig. 6(b). Although the spatial difference spectrum (Fig. 6c) between the spectra from the Sr and Ti-O columns shows a reduction in the vicinity of the Sr M_{2,3} edge and an enhancement in the Ti L_{2,3} edge, both spectra seem almost identical and it would be harder to distinguish one spectra from another. To confirm the difference in the spectra between the Sr and Ti-O columns, MSA was applied to the dataset. By applying the MSA method, the SI dataset can be decomposed to loading and score matrices: the former contains spectral feature uncorrelated to other row information and the later represents the spatial amplitude of the corresponding loading spectrum. In Fig. 7,

pairs of the loading spectrum and the corresponding score image of the (a) first and (b) second components are compared. The most significant component in the dataset is always the average (i.e., the average information is repeated at every pixel), and hence the loading spectrum of the first component represents the average spectrum of the SI dataset. Sr M_{2,3} and Ti L_{2,3} edges can be seen in this SI dataset. Any component after the first component indicates the difference from the average. Therefore, loading spectra after the first component contain positive and negative regions. The brighter regions in the score image of second component correspond to the Ti-O atom-

pairs of the loading spectrum and the corresponding score image of the (a) first and (b) second components are compared. The most significant component in the dataset is always the average (i.e., the average information is repeated at every pixel), and hence the loading spectrum of the first component represents the average spectrum of the SI dataset. Sr M_{2,3} and Ti L_{2,3} edges can be seen in this SI dataset. Any component after the first component indicates the difference from the average. Therefore, loading spectra after the first component contain positive and negative regions. The brighter regions in the score image of second component correspond to the Ti-O atom-

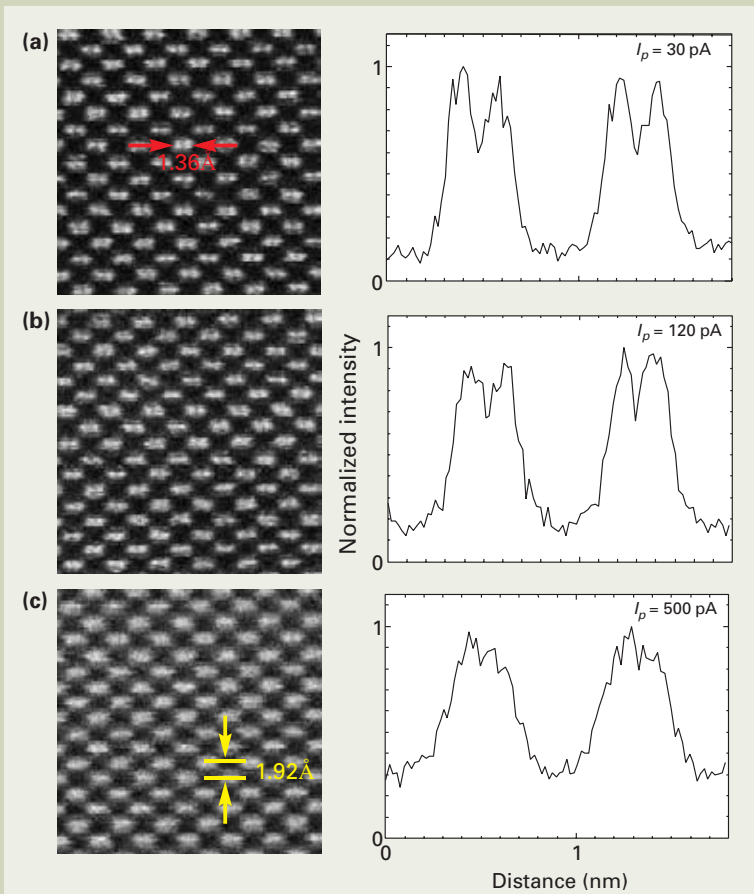


Fig. 4 HAADF-STEM images of [110]-projected Si recorded at (a) 30, (b) 120 and (c) 500 pA in an aberration-corrected 200 kV JEOL JEM-2200FS STEM with a Schottky FEG. Normalized intensity profiles extracted from the individual images are also inserted for comparison [17].

Fig. 6 (a) HAADF-STEM image of a [001]-projected SrTiO₃ specimen. From a region indicated as a dashed square, an EELS-SI data was acquired with 13×13 pixels for a dwell time of 0.1 s per pixel. (b) Two spectra at the Sr and Ti-O column positions extracted from the SI are compared. (c) The spatial differential spectrum [26].

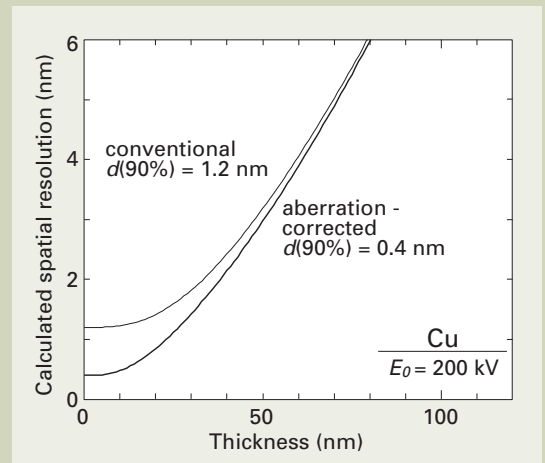
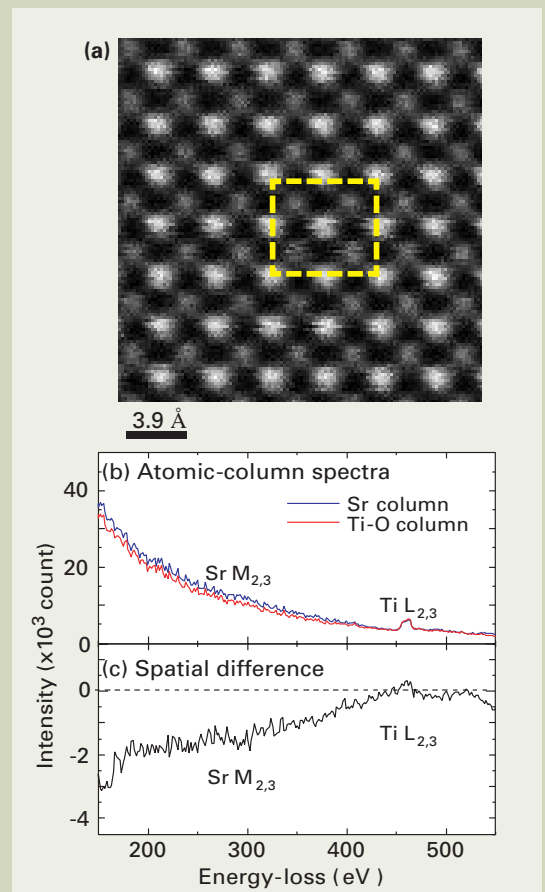


Fig. 5 Spatial resolution (90%) calculated for a Cu thin specimen in conventional and aberration-corrected conditions at 200 kV based on the Gaussian probe broadening model, as plotted against the specimen thickness [17].



ic-columns, where the Ti L_{2,3} edge signal is more enhanced and the Sr M_{2,3} edge signal is reduced. This second component agrees well with the spatial difference spectrum shown in Fig. 6(c), i.e. the Ti L_{2,3} edge signals are clearly increased at the Ti-O columns in SrTiO₃. Therefore, the signal fluctuation in different atomic-columns is real and essentially one of the dominant features repeated a number of times in the dataset.

In addition, MSA may reveal unexpected features in the dataset as well. **Figure 8** shows another example of the MSA application to atomic-column EELS SI dataset taken from a [0001]-projected Si₃N₄ specimen by an aberration-corrected JEM-2010F STEM at 200 kV [27]. The SI dataset was recorded with 50×45 pixels and 670 energy-channels (with binning 2) using a Gatan Enfina spectrometer for a dwell time of 20 ms. The first two components extracted from the dataset by MSA are shown in Fig. 8. Again, the average is the most frequently repeated information in the dataset (component #1) as shown in Fig. 8a. In the component #2 (Fig. 8b), the brighter regions in the score image correspond to the Si atom positions in the six-fold ring. Surprisingly, this enhancement at Si atom positions occurs not at the Si L_{2,3} edge, but after the Si L₁ edge as shown in the spectrum of component #2. This resolution difference in a different energy-loss region can be due to the delocalization-effect dependence on the offset energy from the ionization edge, as recently discussed by Kimoto et al. [28]. Such unique correlations of spectral features with specific spatial locations might not be identified accurately unless these correlations are well known prior to data acquisition/analysis. However, by applying MSA, these unexpected features can be automatically revealed, based on numbers that the features are repeated.

After dominant features are identified in the dataset, the original dataset can be described with a limited number of the featured components, and then random noise that is not repeated at all can be efficiently removed from the dataset. The data reconstruction without random noise components results in the enhancement of weak signals in SI datasets. In the SI dataset from atomic-resolution Si₃N₄, the noise reduction was applied by subtracting noise components. **Figure 9** compares Si L_{2,3} edge (a) and Si L₁ edge (b) maps extracted with background subtraction from the original and MSA-reconstructed datasets. This comparison of maps from the original and reconstructed datasets clearly demonstrates the efficient removal of the noise. The reconstructed maps from both the Si L_{2,3} and L₁ edges maps show Si atom arrangement with a six-fold ring. The Si atom arrangement in the six-fold ring is more clearly pronounced in the Si L₁ map, and the individual Si atomic columns can be clearly distinguished, as expected from component #2 shown in Fig. 8(b).

Recently, one of the authors (MW) has developed the MSA software package as a series of plug-in for Gatan DigitalMicrograph Suite [29]. This particular MSA plug-in package has been applied for various SI datasets acquired by EELS and XEDS [3, 5, 29-32]. This package is now available through HREM Research Inc. Further information can also be found at the company's

web site [33] or the author's web site [34].

Applications of atomic-resolution chemical mapping in the JEM-ARM200F

STEM-EELS based chemical imaging

For atomic-level analysis, the STEM probe must be positioned above individual atomic

column sites during acquisition, which requires relatively long-term instrumental and environmental stabilities. Two examples of atomic-resolution EELS imaging shown above were taken from the 1st generation JEOL aberration-corrected STEMs, which were constructed by adding the CEOS correctors to existing microscope columns. The newly developed JEOL JEM-ARM200F aberration-corrected STEM instrument is designed to perform the atomic-level chemical analysis with improved instru-

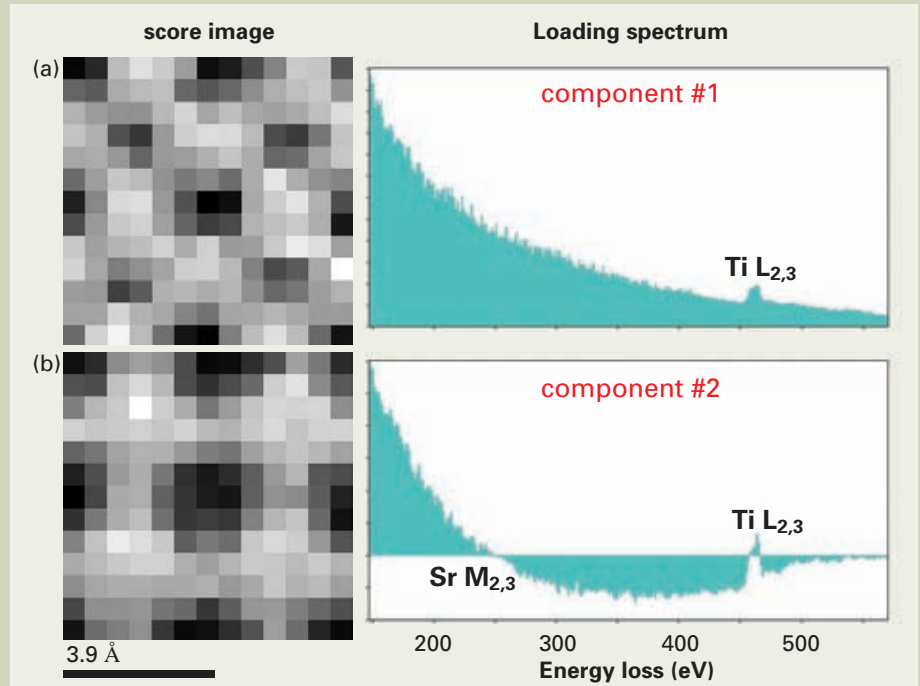


Fig. 7 Pairs of loading spectrum and corresponding score image of component #1 (a) and #2 (b) of an atomic-resolution STEM-EELS SI dataset from SrTiO₃ [26].

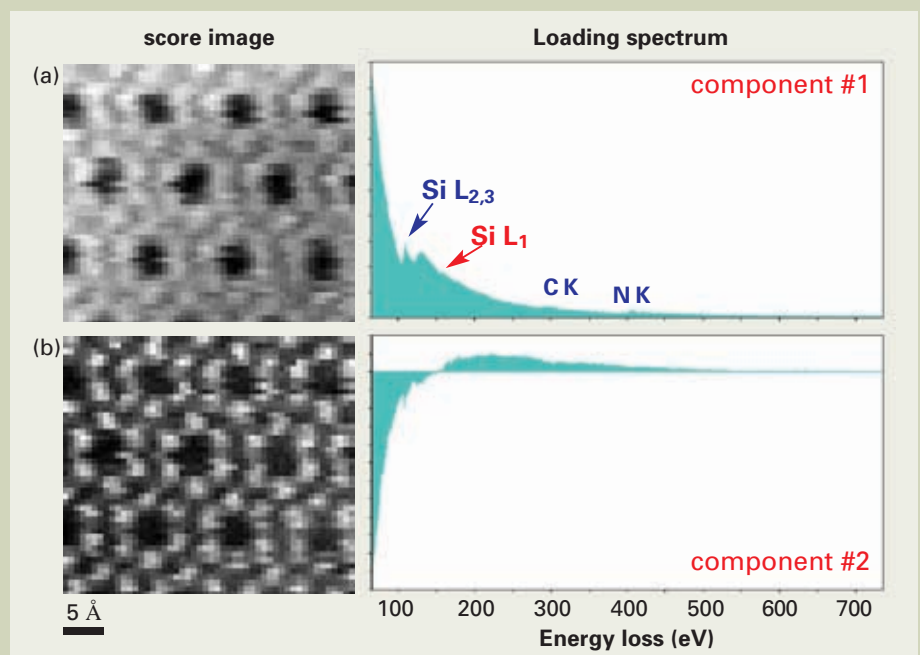


Fig. 8 Pairs of loading spectrum and corresponding score image of component #1 (a) and #2 (b) of an atomic-resolution STEM-EELS SI dataset from Si₃N₄ [27].

mental stabilities. Some of the major improvements of the JEM-ARM200F are: (i) significantly reduced mechanical instabilities by optimizing the column stiffness to accommodate the probe corrector; (ii) efficient suppression of external influences, such as stray electro-magnetic fields, temperature/pressure fluctuations, air flows and sound vibrations, by the incorporation of a heat insulation shield, a magnetic shield and an external mechanical cover; and (iii) reductions in instabilities of the accelerat-

ing voltage, objective/condenser lens currents and deflector coils by a factor of 2 from the first generation instruments[35]. The spatial drift rate in the new instrument is 0.5 nm/min.

The improved performance for atomic-resolution analysis in the newly developed JEM-ARM200F is shown in Fig. 10, as an example. An HAADF-STEM image from an interface in a $\text{LaMnO}_3/\text{SrTiO}_3$ multilayer thin-film is shown in Fig. 10(a). The bright and slightly fainter spots appearing in this HAADF-STEM

image correspond to heavy atomic columns of La or Sr and to Ti-O or Mn-O columns in the perovskite structure, respectively. An EELS SI data was acquired from the same field of view with 186×26 pixels and 1350 channels for a dwell time of 0.1 s using a Gatan Enfina spectrometer. After applying MSA, elemental maps were extracted by power-law background subtraction. From the extracted elemental maps, two RGB color-overlay images were constructed as shown in Fig. 10(b, Red: Ti $L_{2,3}$, Green:

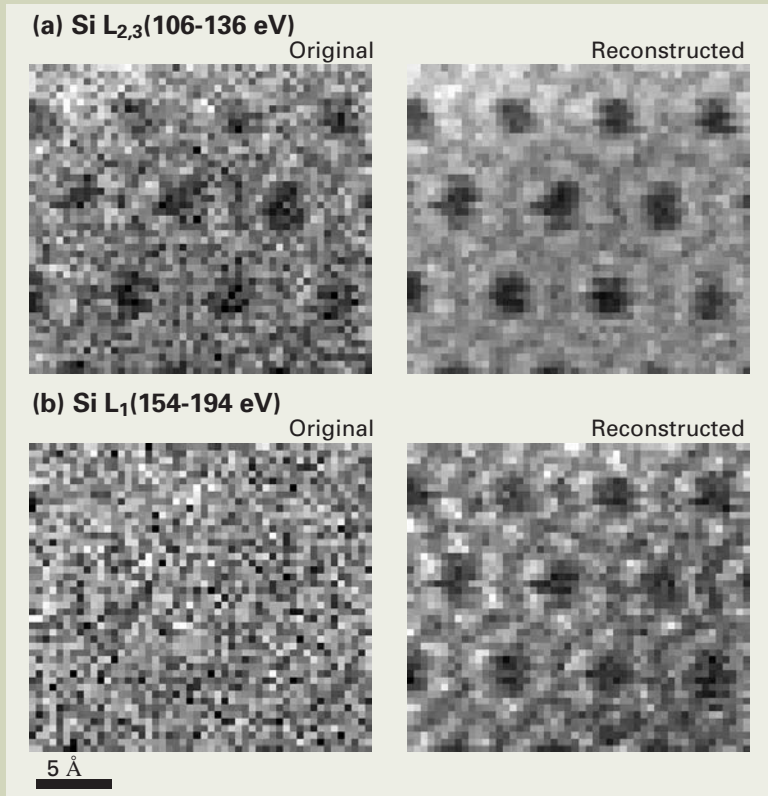


Fig. 9 Comparison of characteristic signal maps of (a) Si $L_{2,3}$ and (b) Si L_1 edges extracted from the original and MSA-reconstructed SI datasets of Si_3N_4 with background subtraction [27].

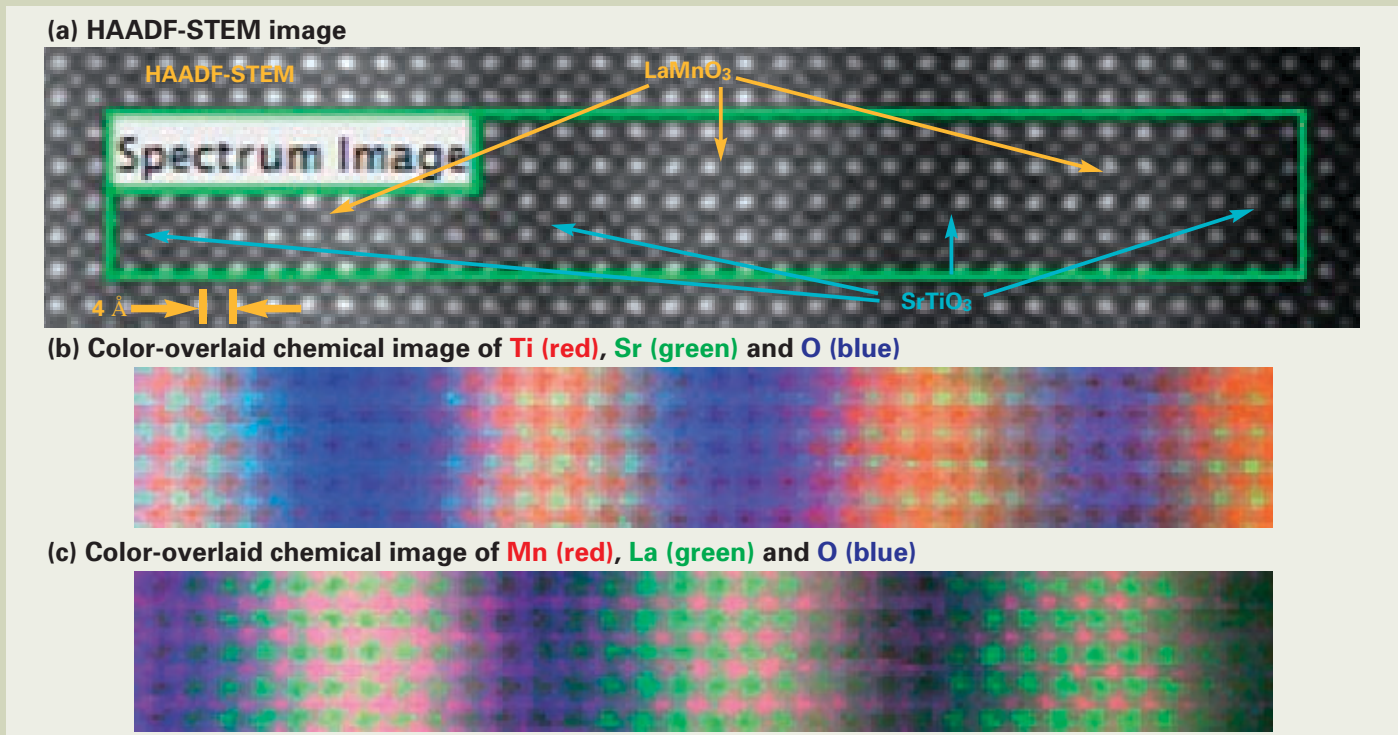


Fig. 10 (a) HAADF-STEM image from a $\text{LaMnO}_3/\text{SrTiO}_3$ interface, (b) RGB color-overlay image of SrTiO_3 and (c) RGB color-overlay image of LaMnO_3 , obtained by the EELS approach (Specimen courtesy of Drs. Maria Varela and Ho Nyung Lee at Oak Ridge National Lab.) [36].

Sr $M_{2,3}$ and Blue: O K) and 1(c, Red: Mn $L_{2,3}$, Green: La $M_{4,5}$ and Blue: O K), which represent $SrTiO_3$ and $LaMnO_3$ layers, respectively [36]. Elemental distributions can be obtained from much larger fields of view, which is only possible in the improved stability in the JEM-ARM200F. In addition, at individual atomic columns can be clearly distinguished. Especially the Ti distribution is terminated at the $LaMnO_3/SrTiO_3$ interfaces relatively sharply, whereas the Mn distribution seems diffused toward $SrTiO_3$ layers.

STEM-XEDS-based Chemical Imaging

As shown above, atomic-resolution EELS imaging is routinely applicable in aberration-corrected STEM with better resolution and improved stability [e.g., 3-5]. For X-ray analysis, such atomic-column analysis or even atomic-column mapping has not even been attempted, mainly because atomic-resolution STEM images are not obtainable with the higher probe currents (and consequent large probes) required for X-ray analysis in conventional STEM instruments due to poorer signal collection efficiency as discussed above (~100 times worse than EELS). However, since the aberration correction makes it possible to reduce the incident probe size while maintaining higher currents, it may be feasible to perform atomic-column X-ray analysis. In fact, the spatial resolution of X-ray analysis is improved to ~0.4 nm [6] and the detectability limit may approach a few atoms [17], which implies atomic-level analysis/mapping by X-ray analysis is feasible in aberration-corrected STEM.

Using the JEM-ARM200F microscope, GaAs was analyzed at an atomic scale by the XEDS approach [36]. **Figure 11** (a) shows an atomic-resolution HAADF-STEM image of [001]-projected GaAs. In this projection, the Ga and As layers are separated, as shown schematically in Fig. 11 (b) (drawn by Vesta [37]). Since the difference in the atomic number is only two between Ga (31) and As (33), the Z-contrast between two elements may not appear unless a very thin specimen is observed. An XEDS SI dataset was recorded from the squared area shown in Fig. 11 (a), and then MSA was performed to improve weak signals in the dataset. In Fig. 11 (c), the second component extracted by MSA is shown as a pair comprising the loading spectrum and the score image. The loading spectrum shows positive K and L peaks of Ga and negative K and L peaks of As. Therefore, the brighter regions in the score image must correspond to the Ga columns, whereas the darker regions correspond to the As columns. Thus, this particular component definitely shows the signal separation between Ga and As. **Figure 12** shows a HAADF-STEM image (a) and X-ray maps of Ga $K\alpha$ and As $K\alpha$ lines with their color overlay image (b), X-ray maps of Ga L and As L lines with their color overlay image (c), and EELS maps of Ga $L_{2,3}$ and As $L_{2,3}$ edges with their color overlay image (c), which were also simultaneously recorded with the XEDS SI dataset. Although the signal levels are still very limited in comparison with EELS results, atomic-level XEDS analysis is now possible through the combination of aberration-corrected STEM and MSA. If the detection efficiency of X-ray signals is improved, atomic-column X-ray mapping would be routinely applicable.

Summary

In this manuscript, the optimum probe-formation in aberration-corrected STEMs was reviewed for atomic-resolution chemical analysis by EELS and XEDS. The new approaches for data acquisition by SI and for data analysis via MSA were discussed as well. By applying MSA, unexpected information hidden in a SI dataset can be revealed. In addition, random noise in the datasets can be efficiently reduced by MSA. This combination of SI with MSA is very useful for analysis of atomic-column datasets, where unexpected signal correlations might be hidden over relatively high random noise due to the short acquisition time and the small analytical volume, as shown in several examples. It is now possible to perform atomic-resolution chemical imaging by STEM-EELS and STEM-XEDS methods in the latest aberration-corrected instrument, such as the JEM-ARM200F. In near future, the atomic-resolution chemical imaging approach would be routinely available for materials characterization.

Acknowledgements

One of the authors (MW) wishes to acknowledge the support of the National Science Foundation through grant (DMR-0804528). The authors would also like to thank Prof. David Williams (currently at the Univ. of Alabama, Huntsville) for his thoughtful supervision for many years. In addition, the author would like to thank Prof. Christopher Kiely and Mr. David Ackland at Lehigh for long-term collaboration, Dr. Kazuo Ishizuka and Mr. Kenta Yoshimura at HREM Research Inc. for development of the MSA plugin, Dr. Hidetaka Sawada at JEOL Ltd. for discussion in probe simulation, and Dr. Maria Varela and Dr. Ho Nyung Lee at Oak Ridge National Lab. for providing the $LaMnO_3/SrTiO_3$ multilayer specimen.

References

- [1] R. Emi, et al., *Phys. Rev. Lett.*, **102**, 096101 (2009).
- [2] H. Sawada, et al., *J. Electron Microsc.*, **58**,

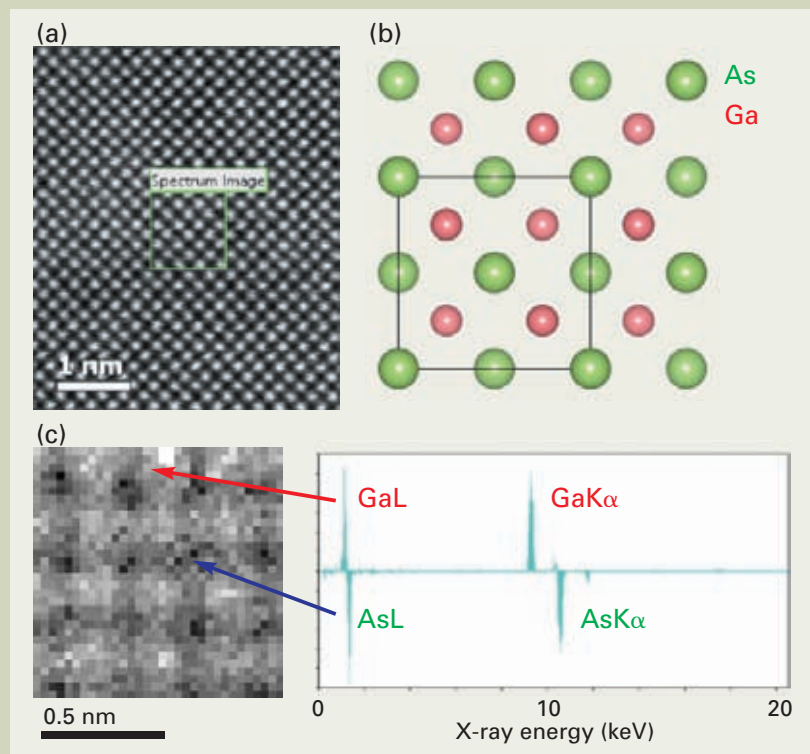


Fig. 11 (a) HAADF-STEM image taken from a [001]-projected GaAs specimen. An X-ray SI dataset was acquired from the selected squared region in the aberration-corrected JEM-ARM200F; (b) a schematic diagram of arrangements of Ga and As atoms in the [001]-projected GaAs, as drawn by Vesta [39]. (c) a pair of loading spectrum and score image of a statistically significant component extracted from the X-ray SI dataset by applying MSA [36].

- 357, (2009).
- [3] M. Bosman, et al., *Phys. Rev. Lett.*, **99**, 086102 (2007).
- [4] D.A. Muller, et al., *Science*, **319**, 1073 (2008).
- [5] M. Varela, et al., *Phys. Rev. B*, **79**, 085117 (2009).
- [6] M. Watanabe, et al., *Microsc. Microanal.* **12**, 515 (2006).
- [7] E. Munro, in *Proc. 8th Int. Congr. on X-Ray Optics and Microanalysis* (ed. by R. Ogilvie and D. Wittry), paper no. 19. (NBS, Washington DC, 1977).
- [8] C. Colliex, C. Mory, in *Quantitative Electron Microscopy*, ed. by J.N. Chapman, A. Craven, (Scottish University Summer School in Physics, Glasgow, Scotland, 1984), p. 149
- [9] M. Haider, et al., *Ultramicroscopy* **81**, 163 (2000)
- [10] J.E. Barth, P. Kruit, . *Optik* **101**, 101 (1996).
- [11] L.M. Brown, *J.Phys. F: Metal Phys.* **11**, 1, (1981).
- [12] M. Watanabe, H. Sawada, *Ultramicrosc.*, (submitted).
- [13] J. Fertig, H. Rose, *Optik*, **54**, 165 (1979).
- [14] H. Rose, *Nuclear Inst. Methods*, **187**, 187 (1981).
- [15] H. Müller, et al., *Microsc. Microanal.*, **12**, 442 (2006).
- [16] H. Sawada, et al., *J. Electron Microsc.*, **58**, 341 (2009).
- [17] M. Watanabe, "X-ray Analysis in Aberration-Corrected Analytical Electron Microscopes" in *Scanning Transmission Electron Microscopy: Imaging and Analysis*, Eds. Stephen J. Pennycook and Peter D. Nellist (in print).
- [18] P. Doig, et al., *Philos. Mag. A* **41**, 761 (1980).
- [19] P. Doig, P.E.J. Flewitt, *Met. Trans. A* **13**, 1397 (1982)
- [20] E. Van Cappellan, A. Schmitz, *Ultramicrosc.* **41**, 193 (1992).
- [21] C. Jeanguillaume, C. Colliex, *Ultramicrosc.*, **28**, 252 (1989).
- [22] J.A. Hunt, D.B. Williams, *Ultramicrosc.*, **38**, 47 (1991).
- [23] I.T. Jolliffe, *Principal component analysis*. 2nd ed. Springer, New York, (2002).
- [24] E.R. Malinowski, *Factor analysis in chemistry*. 3rd ed. Wiley, New York, (2002).
- [25] P.G. Kotula, et al., *Microsc. Microanal.* **9**, 1 (2003).
- [26] M. Watanabe, et al., *Microsc. Microanal.* **13** (2007), Suppl. 2, 1264.
- [27] M. Watanabe, et al., *Microscopy and Analysis*, **23**, Issue 7, 5, (2009).
- [28] K. Kimoto, et al., *Micron*, **39**, 257, (2008).
- [29] M.G. Burke, et al., *J. Mater. Sci.* **41**, 4512, (2006).
- [30] M. Bosman, et al., *Nanotechnology* **18** 165505 (2007).
- [31] T. Yaguchi, et al., *Ultramicrosc.*, **108**, 1603, (2008).
- [32] M. Bosman, et al., *Carbon*, **47**, 94, (2009).
- [33] <http://www.hremresearch.com/Eng/plugin/MSAEng.html>.
- [34] <http://www.lehigh.edu/~maw3/research/msamain.html>.
- [35] I. Ishikawa, et al., *Microsc. Microanal.*, **15**, Suppl. 2, 188 (2009).
- [36] M. Watanabe, et al., *Microsc. Microanal.* **16** (2010), (in press).
- [37] K. Momma, F. Izumi, *J. Appl. Crystallogr.*, **41**, 653 (2008).

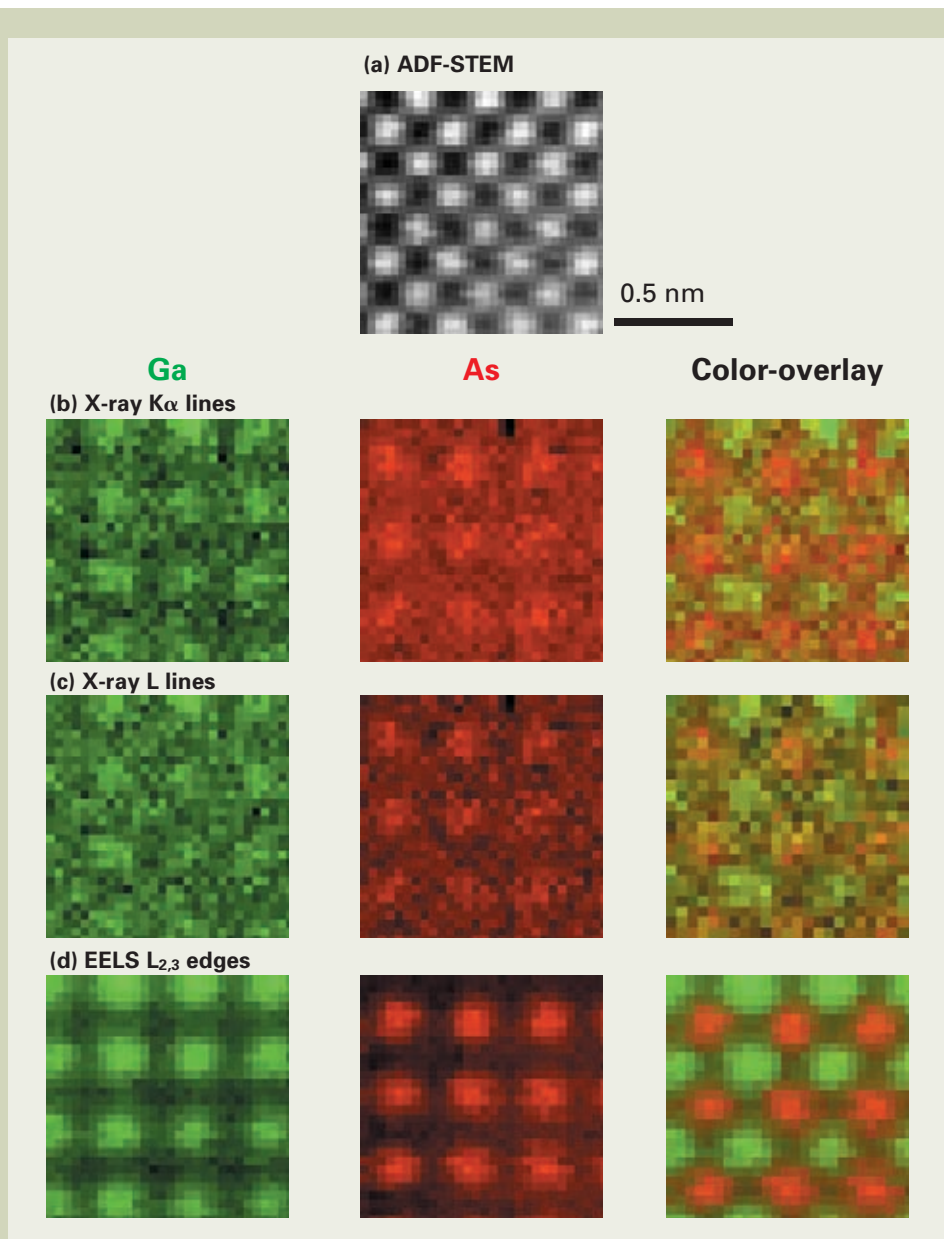


Fig. 12 (a) HAADF-STEM image of the [001]-projected GaAs simultaneously recorded during SI acquisition; a set of a Ga maps, an As map and a color-overlay map of K α X-ray lines (b), L X-ray lines (c) and EELS L_{2,3} edges (d) [36].

Application of a Helium-Cooled Cryo-Electron Microscope for Single Particle Analysis

Kaoru Mitsuoka

Biomedical Information Research Center,
National Institute of Advanced Industrial Science and Technology

Single particle analysis can determine three-dimensional structures of biological molecules at high resolution without the crystals. The principle obstacle for high-resolution structural analysis in electron microscopy is irradiation damage of the biological specimen, and cooling the specimen to cryogenic temperatures can reduce the effects of irradiation damage. To achieve higher resolution structures by reducing the irradiation damage, even in single particle analysis, a new cryo-electron microscope with a liquid helium-cooled stage for single particle analysis was developed, and we utilized it in two studies using single particle analysis. For the application, we slightly modified the sample preparation technique developed for the high-resolution image collection from the tubular crystals, using the liquid helium-cooled stage. The first application was to determine the structure of the GroEL-GroES-substrate complex from *Thermus thermophilus*. We observed a density corresponding to the folding substrates inside the complex. The second application was the three-dimensional reconstruction from tubular crystals of a membrane protein, human erythrocyte band 3. Iterative helical real-space reconstruction, which is a modification of single particle analysis for tubes with helical symmetry, was used for this purpose. These two examples clearly show that the three-dimensional structures of a broad range of targets can be analyzed by single particle analysis.

Introduction

Cryo-electron microscopy (cryo-EM) is a powerful tool in structural biology for a broad range of targets and resolutions. Electron crystallography can yield maps with better than 2 Å resolution from two-dimensional (2D) crystals of membrane proteins [1]. Tubular crystals of membrane proteins are grown during the 2D crystallization trials of membrane proteins, and helical reconstruction can provide the three-dimensional (3D) structures at atomic resolution in those cases [2]. The resolution of single particle analysis of protein complexes has been improving [3], and an atomic model was recently proposed from a 3D structure determined by this method [4]. While all three of these methods can determine the atomic model from the 3D reconstruction, single particle analysis does not require crystals for the structural determination, and therefore it is considered to be the most general method. In addition, because the particles in different states can be distinguished by image classifications in the single particle method, we can analyze the structures in an equilibrium of different states. Thus, the range of targets for high-resolution structural analysis can be expanded by single particle analysis.

The principle obstacle for high-resolution structural analysis in electron microscopy is irradiation damage of the biological specimen by incident electrons. Cooling the specimen to cryogenic temperatures can reduce the effects of irradiation damage. A comparison of the decay of intensities from tRNA and catalase crystals by electron diffraction revealed that the irradiation damage was reduced to about 1/4 and 1/10 of the value at room temperature,

when the specimens were cooled below 100 K and 20 K, respectively [5]. Therefore, a liquid helium-cooled stage for electron crystallography, where the resolution is mainly determined by electron diffraction patterns, was developed [6], and thus we obtained many atomic models of membrane proteins using the helium stage [7]. Although it is not clear whether the enhanced protection at 20 K is quantitatively the same as in the conditions of electron

microscopy, it may be possible to achieve higher resolution structures by using a liquid helium-cooled stage to minimize the irradiation damage, even in single particle analysis.

To explore this possibility, a new cryo-electron microscope with a liquid helium-cooled stage for single particle analysis was developed and utilized to study the GroEL-GroES-substrate complex. Here we will describe how we optimized the specimen preparation

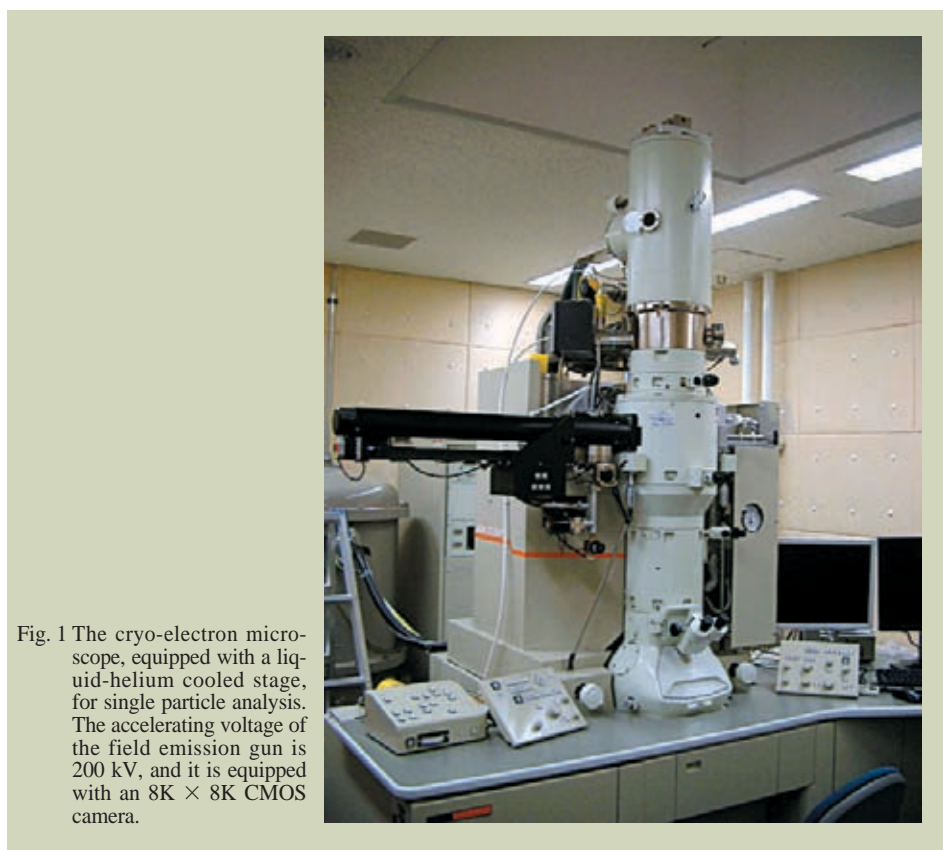


Fig. 1 The cryo-electron microscope, equipped with a liquid-helium cooled stage, for single particle analysis. The accelerating voltage of the field emission gun is 200 kV, and it is equipped with an 8K × 8K CMOS camera.

2-3-26, Aomi, Koto-ku, Tokyo, 135-0064 Japan

kaorum@ni.aist.go.jp

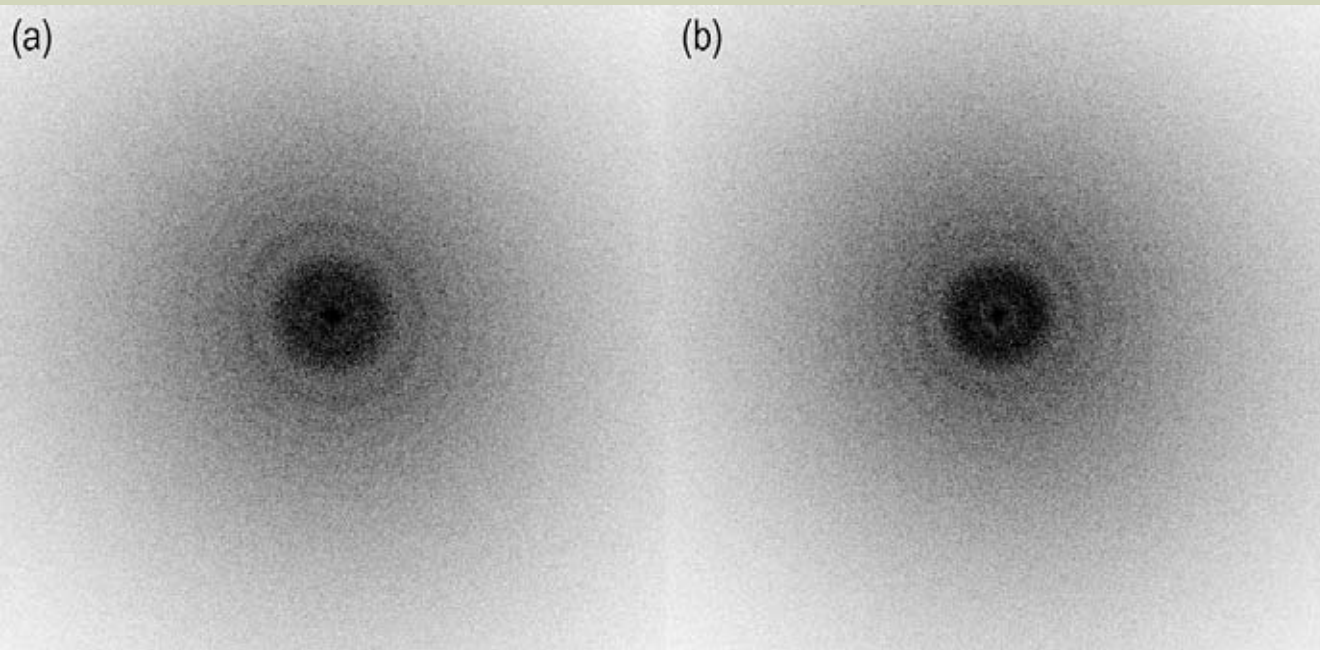


Fig. 2 Typical Fourier transforms from good and poor images. These were calculated from a $4K \times 4K$ area with a pixel size of about 1.8 \AA and a defocus value of about $2 \mu\text{m}$. (a) Fourier transforms from a good image. The Thon rings are clear and symmetrical. (b) Fourier transforms from a poor image. The Thon rings do not extend to the higher resolution and are asymmetrical.

for single particle analysis using the liquid-helium cooled stage, and the resulting structure we obtained using the protein complexes from *Thermus thermophilus*. In addition, we recently applied the single particle analysis to the tubular crystals of a membrane protein, and those results will also be discussed.

Helium-cooled cryo-electron microscope for single particle analysis

While the new JEOL cryo-electron microscope equipped with a liquid-helium cooled stage for single particle analysis has almost the same cryo-stage as those of the cryo-electron microscopes used for electron crystallography [11], the accelerating voltage of the field emission gun is 200 kV, and it is equipped with a CMOS camera with pixel sizes of 8k by 8k (TemCam-F816, TVIPS, Gauting, Germany). The advantage of the 8K camera for single particle analysis is clear. We can collect more particle images from one exposure, and therefore the data collection is more efficient. The choice of the accelerating voltage is also related to the camera. The point-spread function of the camera becomes better at 200 kV, as compared with the accelerating voltage of 300 kV, which we usually use for electron crystallography. Therefore, we can use a lower magnification, which also improves the efficiency of the data collection. The new cryo-electron microscope for single particle analysis installed in our institute is shown in **Figure 1**.

In addition, the lower accelerating voltage also enhances the image contrast. At the lower accelerating voltage, more electrons can interact with the materials. The ratio of the intensity formed by zero-loss electrons, which can be used for image formation, to the total intensity of the direct beam can be determined by the

elastic mean free path. The elastic mean free paths in ice for 200 kV electrons and 300 kV electrons are 500 nm and 622 nm, respectively, using equation (1) in Langmore and Smith [12]. Assuming these values and an ice thickness of 100 nm, which is sufficiently large for the size of the GroEL-GroES complex (about 20 nm), the ratios of the electrons used for the imaging are 0.18 and 0.15, respectively.

Since we can irradiate with more electrons when using 300 kV, this comparison is not related to the signal-to-noise ratio. However, this enhancement of the ratio of the image-forming electrons to the total intensity has a clear effect on the image contrast of the GroEL-GroES-substrate complexes. We can calculate the image contrast, using the following equation and the experimental values obtained for the GroEL-GroES complexes,

$$\text{Contrast} = \frac{|Ave_{sg} - Ave_{bg}|}{Std_{bg}}$$

where Ave_{sg} is the average of the pixel values in the particle images, Ave_{bg} is the average of the pixel values in the background area, and Std_{bg} is the standard deviation of the background area. The calculated values are 0.11 and 0.045 for 200 and 300 kV, respectively, and thus the image contrast is much better at 200 kV than at 300 kV. Since the contrast of the cryo-images is very weak, the improvement in the number of electrons for the imaging could clearly enhance the image contrast.

Sample preparation for helium-cooled cryo-electron microscopy

The preparation of the EM grids to yield good images for image processing, using the liquid helium-cooled stage, is also important. The sig-

nificant difference between the nitrogen and helium temperatures lies in the conductivity of the specimen. Since the resistance of carbon is significantly increased at 4 K, some care must be taken to minimize the beam-induced movement by specimen charging. The procedures described here were developed for the high-resolution image collection from tubular crystals of nicotinic acetylcholine receptor [13], and we used the techniques with only slight modifications. Electron irradiation usually results in charging of biological specimens, which causes beam-induced movement. The inelastic scattering causes the emission of secondary and Auger electrons, which render the specimen positively charged. A clean, $30 \mu\text{m}$ diameter gold foil objective aperture can be used to emit electrons to neutralize the positive charge.

The preparation of the high conductivity carbon film was also important to minimize the beam-induced movement. When we used Quantifoil R1/4 holey grids (Quantifoil Micro Tolls GmbH, Jena, Germany), we deposited carbon (99.9999% purity) onto the grids, with minimal sparking, in a vacuum of $<10^{-5}$ mbar during deposition, after washing the Quantifoil grids by immersing them in purified water over several hours. After the deposition, the grids were washed again by immersing them in ethyl acetate for 20 minutes. The carbon-coated grids were then irradiated by 100 kV electrons with a total dose of over $100 \text{ e}^-/\text{\AA}^2$ for more than 3 hours. This pre-exposure could improve the conductivity of the carbon.

Finally, symmetrical imaging conditions, with the beam entirely covering the hole all the way to the carbon, were used. However, even after these considerations, our ability to obtain good images was still marginal. To evaluate the images, we calculated the Fourier transforms from the center area of the hole. As shown in **Figure 2**, the Fourier transforms calculated from a good image show clear and symmetrical

Thon rings, while the Thon rings from a poor image do not extend to the high-resolution range and are asymmetrical. From this calculation, we can determine the ratio of good images. To achieve a success rate of over 50 % from almost all of the grids after these treatments, we usually use a pre-exposure time of 1.0 second for a 2.0 s exposure. We consider the damage from this irradiation to be acceptable, because of the 2.5-fold reduction in the damage by using liquid helium, as compared to liquid nitrogen.

Single particle analysis of the GroEL-GroES-substrate complex

We used the microscope and the techniques described above to analyze the structure of the GroEL-GroES-substrate complex [14]. GroEL is a molecular chaperone, which helps other proteins to fold properly, and is called a chaperonin. It works as an essential mediator for folding in eubacteria, mitochondria, and chloroplasts. The co-chaperonins GroES and ATP are required for GroEL to exert its full activity, and they form a large complex [15]. The complex consists of two heptameric rings of GroEL stacked back-to-back and seven subunits of GroES, which form a dome-shaped structure on top of the GroEL rings. The formation of this complex creates a large hydrophilic cavity, and the folding polypeptide is considered to be encapsulated in the cavity so that it can be correctly folded into the native conformation without the risk of aggregation. However, the folding substrate inside the cavity has never been visualized. Therefore, we used the native chaperonin complex from *Thermus thermophilus*, a thermophile, to visualize the substrate inside the cavity, because the complex from the thermophile is quite stable, and at least 24 different substrate proteins were identified from the purified complexes.

The structures of GroEL and its complexes have been studied extensively by single particle analysis [16]. Single particle analysis by cryo-electron microscopy has the advantage that it can solve the structure under any solution conditions. In addition, heterogeneous samples can be analyzed by this method, because the averaged structure of the similar but heterogeneous specimens can be calculated, and the images can be classified into several different structures. Thus, it could be much easier to calculate the intermediate structures by single particle analysis, rather than crystallographic methods. Here we averaged the complex with different folding substrates, because many different folding substrates are folded by GroEL. However, the classification of several different structures and the calculation of those structures are also possible using GroEL, and those results were published at almost the same time as our result [17].

We accumulated 28,188 particle images, which were selected as GroEL-GroES complexes as judged from their shape, using 336 pictures, and performed the single particle analysis. The 2D alignment and classification processes were performed by the MRA and MSA techniques, using the IMAGIC program packages. The parameters for CTF correction were determined by *ctfit* in the EMAN package. The 3D structure of the complex, which was calculated by the 3D filtered back projection, is

shown in **Figure 3**. The reconstructed 3D map clearly showed a density corresponding to the substrate proteins at almost the center of the cavity. A comparison of the GroEL-GroES complex with that from *E. coli*, which was reconstructed without the folding substrates, confirmed that the density in the cavity was not observed for *E. coli* complex, and therefore it is not an artifact from image processing.

This density is located in the center of the cavity and is surrounded by acidic residues. Since this density is the average of many substrates, the fine details about their interactions with the chaperonin are unknown. However, considering the result that the density is not scattered throughout the cage, but is concentrated in the center of the cavity, the majority of the substrate proteins are restricted in a limited space. Thus, the observed position of the substrates indicates the electrostatic repulsion effects for most of the GroEL substrates. In fact, most GroEL substrates have a negative net charge. The protein folding might be assisted by this interaction between the interior walls of the cavity and the substrate proteins.

Application of single particle analysis to the tubular crystal of a membrane protein

The single particle method can be applied not only to protein complexes but also to various samples. For example, the 3D structures of the tubular crystals of membrane proteins can be analyzed by modifying this method. Iterative helical real-space reconstruction (IHRSR) uses single-particle image analysis, in combination with imposed real-space helical symmetry, to allow the effective analysis of tubular crystals with such properties as poorly ordered helical symmetry, bent tubes, or low signal-to-noise ratios on electron microscopy images [18]. Here, we show the 3D structure of the membrane domain of erythrocyte band 3 in an inhibitor-stabilized, outward-open conformation at 18 Å resolution, which was determined by this method [19].

Erythrocyte band 3 (anion exchanger 1, or AE1) mediates the electroneutral exchange of ions such as chloride and bicarbonate across the erythrocyte plasma membrane. Band 3 contains functionally independent cytoplasmic and membrane domains. The cytoplasmic domain functions to anchor the cytoskeleton to the plasma membrane, while the membrane domain allows anion exchange. We purified the band 3 protein with the anion transport inhibitor 4,40-diisothiocyanatodihydrostilbene-2,20-disulfonic acid (H₂DIDS). Stilbene compounds, such as H₂DIDS, reportedly stabilize band 3 in the outward-open form. Using the purified H₂DIDS-bound, outward-open membrane domain of band 3 (hB3MD) and a dialysis procedure, we obtained tubular crystals with a diameter of 37 nm, and applied IHRSR to the crystals.

Figure 4 shows the overall 3D map of the band 3 tubular crystal. Two hB3MD molecules, which form a dimer, are enclosed within blue and green boxes. All of the hB3MD dimers in the tubular crystals are oriented in the same direction relative to the tube axis and appear to be in close contact with each other. An immunoelectron microscopy analysis using 2A8 IgG antibodies revealed that the outer and inner surfaces of the tubular crystal corresponded to the

intracellular and extracellular portions of hB3MD, respectively. The membrane domain of band 3 is thought to consist of several subdomains, because a projection image of the 3D map of the hB3MD dimer perpendicular to the membrane plane showed two high-density regions, suggesting that the domain is composed of at least two subdomains. However, it is currently not possible to determine which segment of the molecule belongs to each subdomain. The anion transport mechanism of band 3 has been explained by a "ping-pong" model, which postulates that there is only one transport site, which faces either intracellularly (inward-open form) or extracellularly (outward-open form). Conformational changes between these forms only occur if a substrate is bound to the transport site. The 3D structure of the outward-open form, which consists of at least two domains, is consistent with this model, but a higher resolution structure is required to determine the relationship between the structural features revealed here and the function of band 3.

Conclusion

A new JEOL cryo-electron microscope, equipped with a liquid-helium cooled stage, was developed and used for the structural analysis of the GroEL-GroES-substrate complex and the 3D reconstruction from tubular crystals of human erythrocyte band 3 membrane protein. These results clearly showed the benefits of applying single particle analysis to various heterogeneous samples. The advantages of the liquid-helium cooled stage for single particle analysis should be explored in future experiments. Further improvements in sample preparation and image collection at the liquid helium temperature will enable higher resolution structural analyses by the single particle method.

Acknowledgments

The author would like to thank all of the collaborators who performed the studies described here, who are authors in the referenced papers. The development of the microscope and these studies were supported by NEDO grants.

References

- [1] T. Gonen, Y. Cheng, P. Sliz, Y. Hiroaki, Y. Fujiyoshi, S. C. Harrison, T. Walz, *Nature*, **438**, 633, (2005)
- [2] A. Miyazawa, Y. Fujiyoshi, N. Unwin, *Nature*, **423**, 949, (2003)
- [3] X. Yu, L. Jin, Z. H. Zhou, *Nature*, **453**, 415 (2008)
- [4] J. Zhang, M. L. Baker, G. F. Schröer, N. R. Douglas, S. Reissmann, J. Jakana, M. Dougherty, C. J. Fu, M. Levitt, S. J. Ludtke, J. Frydman, W. Chiu, *Nature*, **463**, 379, (2010)
- [5] Y. Fujiyoshi, *Adv. Biophys.*, **35**, 25, (1998)
- [6] Y. Fujiyoshi, T. Mizusaki, K. Morikawa, H. Yamagishi, Y. Aoki, H. Kihara, Y. Harada, *Ultramicroscopy*, **38**, 241, (1991)
- [7] Y. Kimura, D. G. Vassilyev, A. Miyazawa, A. Kidera, M. Matsushima, K. Mitsuoka, K. Murata, T. Hirai, Y. Fujiyoshi, *Nature*, **389**, 206, (1997)
- [8] K. Murata, K. Mitsuoka, T. Hirai, T. Walz, P. Agre, J. B. Heymann, A. Engel, Y. Fujiyoshi, *Nature*, **407**, 599, (2000)

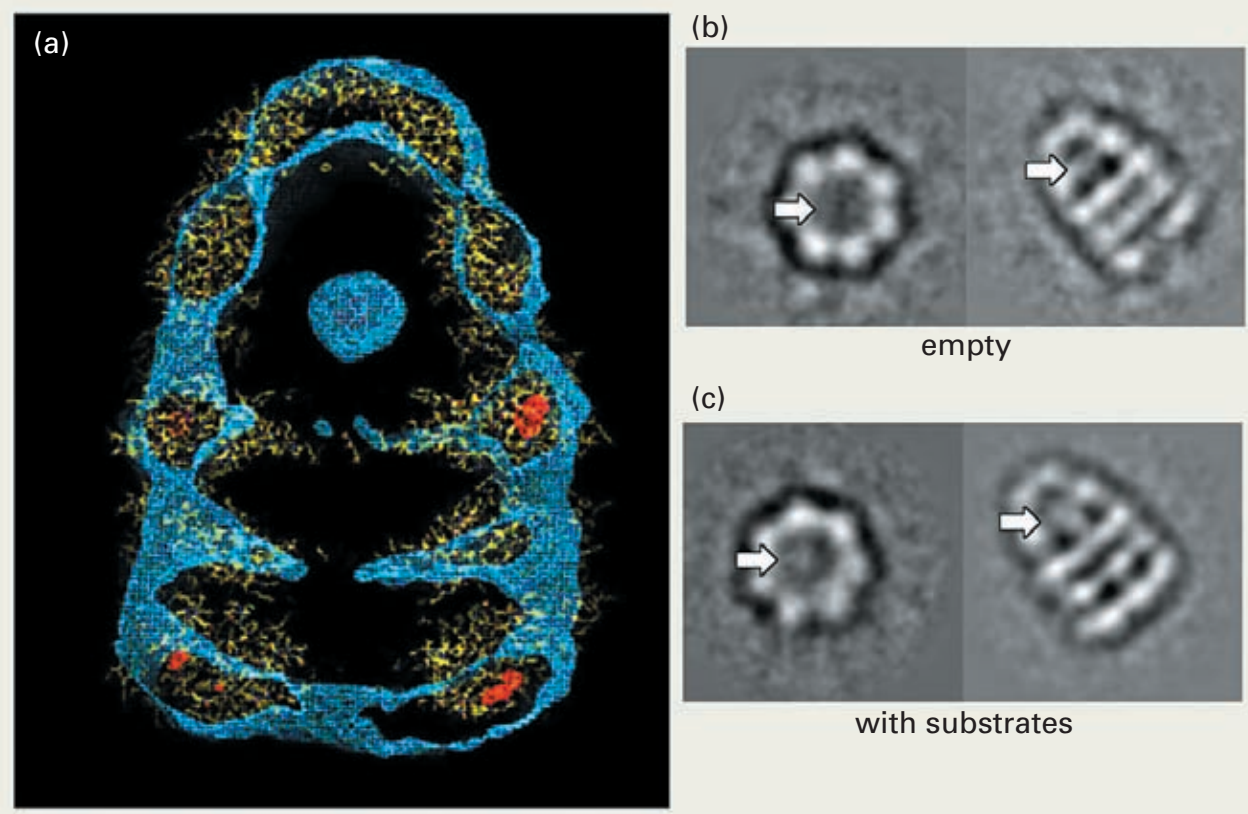


Fig. 3 The overall structure of the GroEL-GroES-substrate complex. (a) Side view of the 3D map, and the fitted atomic model. (b) Comparison of the empty chaperonin complex from *E. coli* with the native complex from *Thermus thermophilus*.

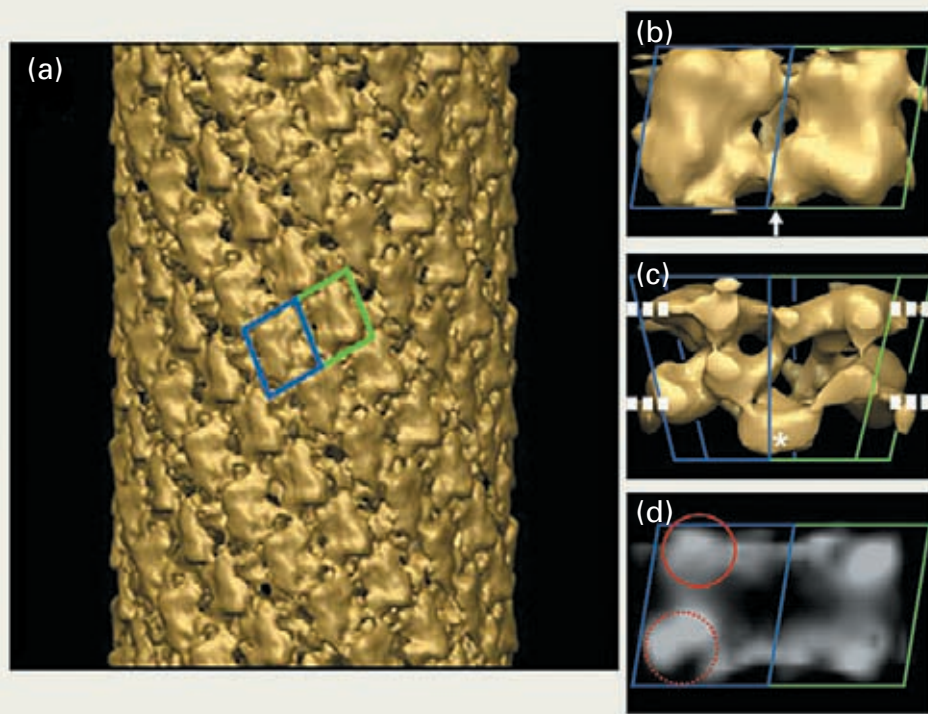


Fig. 4 The 3D image reconstruction of the hB3MD tubular crystal. (a) Side view of the tubular crystal. Two molecules in a possible dimer are enclosed in blue and green boxes. (b) The intracellular surface of a unit cell containing an hB3MD dimer. (c) The 3D map of an hB3MD dimer, viewed in the direction parallel to the tube axis. (d) Projection image of the 3D map from the intracellular side. The two high-density regions are indicated by solid and dashed red circles, to suggest the presence of two subdomains.

- [9] Y. Hiroaki, K. Tani, A. Kamegawa, N. Gyobu, K. Nishikawa, H. Suzuki, T. Walz, S. Sasaki, K. Mitsuoka, K. Kimura, A. Mizoguchi, Y. Fujiyoshi, *J. Mol. Biol.* **355**, 628, (2006)
- [10] P. J. Holm, P. Bhakat, C. Jegerschöld, N. Gyobu, K. Mitsuoka, Y. Fujiyoshi, R. Morgenstern, H. Hebert, *J. Mol. Biol.* **360**, 934, (2006)
- [11] C. Jegerschöld, S. C. Pawelzik, P. Purhonen, P. Bhakat, K. R. Gheorghe, N. Gyobu, K. Mitsuoka, R. Morgenstern, P. J. Jakobsson, H. Hebert, *Proc. Natl. Acad. Sci. USA*. **105**, 11110, (2008)
- [12] J. P. Langmore, M. F. Smith, *Ultramicroscopy*, **46**, 349, (1992)
- [13] A. Miyazawa, Y. Fujiyoshi, M. Stowell, N. Unwin, *J. Mol. Biol.*, **288**, 765, (1999)
- [14] R. Kanno, A. Koike-Takeshita, K. Yokoyama, H. Taguchi, K. Mitsuoka, *Structure*, **17**, 287, (2009)
- [15] Z. Xu, A. L. Horwich, P. B. Sigler, *Nature*, **388**, 741, (1997)
- [16] S. J. Ludtke, D. L. Chen, J. L. Song, D. T. Chuang, W. Chiu, *Structure*, **12**, 1129, (2004)
- [17] D. K. Clare, P. J. Bakkes, H. van Heerikhuizen, S. M. van der Vies, H. R. Saibil, *Nature*, **457**, 107, (2009)
- [18] E. H. Egelman, *J. Struct. Biol.* **157**, 83, (2007)
- [19] T. Yamaguchi, T. Fujii, Y. Abe, T. Hirai, D. Kang, K. Namba, N. Hamasaki, K. Mitsuoka, *J. Struct. Biol.*, **169**, 406, (2010)

Ultrahigh-Resolution STEM Analysis of Complex Compounds

Eiji Abe[†], Daisuke Egusa, Ryo Ishikawa, and Takehito Seki

Department of Materials Science & Engineering, University of Tokyo

Aberration-correction of the objective lens has been successful in converging the electron beam into sub-Å scale, and the scanning transmission electron microscopy (STEM) now routinely provides a remarkably improved spatial-resolution both for imaging and spectroscopy. Here we demonstrate the powerful use of the ultrahigh-resolution STEM for the analysis of complex compounds, including long-period modulated and aperiodic quasicrystalline structures.

Introduction

Quantitative determination of local structures, including how dopant elements distribute within the materials, has been one of the challenging issues of electron microscopy. In this regard, scanning transmission electron microscopy (STEM) indeed provided a breakthrough with its significant atomic-number dependent contrast, termed Z-contrast [1], which is able to show up even the single atom embedded in a solid. Besides, STEM enables the spectroscopic analysis at very small scale; local measurements of energy-dispersive x-ray spectroscopy (EDXS) and electron energy loss spectroscopy (EELS) are possible by locating the atomic-sized electron probe on the regions of interest. Owing to recent development of an aberration corrector for the beam-converging lens, STEM is now capable of electron beam with sub-Ångstrom scale, which has remarkably improved its achievable resolution. In this article, we briefly describe some of our recent results to demonstrate the powerful use of the aberration-corrected STEM, which provides immediate insights into the veiled structural/chemical details of the complex compounds.

STEM Experiment

STEM observations were performed by the JEM-ARM200F (Cs-corrected 200 kV STEM/TEM, equipped with a Schottky-emission electron gun) and by the R005 microscope (Cs-corrected 300 kV STEM/TEM, equipped with a (cold) field-emission electron gun). The latter 300 kV-STEM/TEM was developed under a JST-CREST project "Development of the 0.05 nm-Resolution

(R005) Electron Microscope" (Leader, Prof. Takayanagi). The minimum full-width half-maximum (FWHM) of the STEM probes are calculated to be approximately ~ 0.9 Å and ~ 0.5 Å for 200 kV and 300 kV, respectively. Both STEM indeed provide sub-Ångstrom resolution [2-4], which are demonstrated by imaging the dumbbell atoms separated by less than 1 Å (they occur for the diamond-based structures when viewed along the [112] (or even higher index) direction).

Direct determination of a long-period modulated structure in a $\text{Mg}_{97}\text{Zn}_1\text{Er}_2$ Alloy

Mg alloys containing a small amount of Zn and RE (RE: Y and rare-earth atoms), e.g., $\text{Mg}_{97}\text{Zn}_1\text{RE}_2$ (at.%) alloys reveal excellent mechanical properties with high yield strength over than ~ 500 MPa and elongations better than $\sim 3\%$ at room temperature. One of the key microstructural features is formation of a novel type of long-period ordered (LPO) structure [5], which is long-period chemical-ordered as well as stacking-ordered. There exist several stacking polytypes denoted as 18R, 14H, 10H, 24R, all of which are composed of a common structural unit represented by local ABCA stacking where B- and C-layers are significantly enriched by Zn and RE (these particular layers are denoted as B' and C'-layers hereafter). It is found that a number of weak satellite spots appear in the diffraction pattern taken along the stacking direction (*c*-axis), suggesting that a further ordering within the close-packed B' and C'-layers with a six-times modulation along $\langle 12\bar{1}0 \rangle \alpha$. Using Cs-corrected STEM, we have investigated the detailed chemical order in the 14H-type LPO structure in the $\text{Mg}_{97}\text{Zn}_1\text{Er}_2$ alloy. Note that Er is a large Z element ($Z=68$) compared to the others (Mg: $Z=12$, Zn: $Z=30$), so that indi-

vidual Er atoms can be detected through Z-contrast even they are embedded in the complicated structure.

Cs-correction effects appear to be quite significant for the direct imaging of the dense-packed atomic structures, as obviously demonstrated in Fig. 1 (a) and (b). After Cs-correction, the fundamental reflections of $12\bar{1}0\alpha$ are clearly reproduced in the FFT pattern by accompanying a number of extra weak spots. Concerning that the Z-contrast image reflects a significantly enhanced chemical-potential differences, it can be deduced that the long-period modulation is predominantly due to a concentration modulation along $\langle 12\bar{1}0 \rangle \alpha$. To investigate its average features, we construct auto-correlation map from the observed image of Fig. 1(b), and the result is shown in Fig. 1(c). All the atomic sites are successfully reproduced in the auto-correlation map, and the average modulations can be directly derived from the intensity distributions. The short-range Er configurations should be related to the most intense spots in the map, showing that the Er-Er distance is at the second-nearest sites. This is reasonably attributed to a D_{019} -type short-range order, which is in fact frequently observed in the Z-contrast image of Fig. 1(b). By referring further details of the intensity distributions, we are able to construct an average model of the complex long-range modulated structure, as shown in Fig. 1(d).

Local chemistry of a hydrogen-storage $(\text{La}, \text{Y})_5\text{Ni}_{19}$ complex compounds

LaNi_x ($3 \leq x < 5$) complex compounds with a block-stacking superstructure have attracted increasing attentions due to their reasonably good hydrogen-storage properties at ambient conditions [6,7]. The block-stacking superstruc-

[†]7-3-1, Hongo, Bunkyo-ku, Tokyo, 113-8656, Japan

E-mail: abe@material.t.u-tokyo.ac.jp

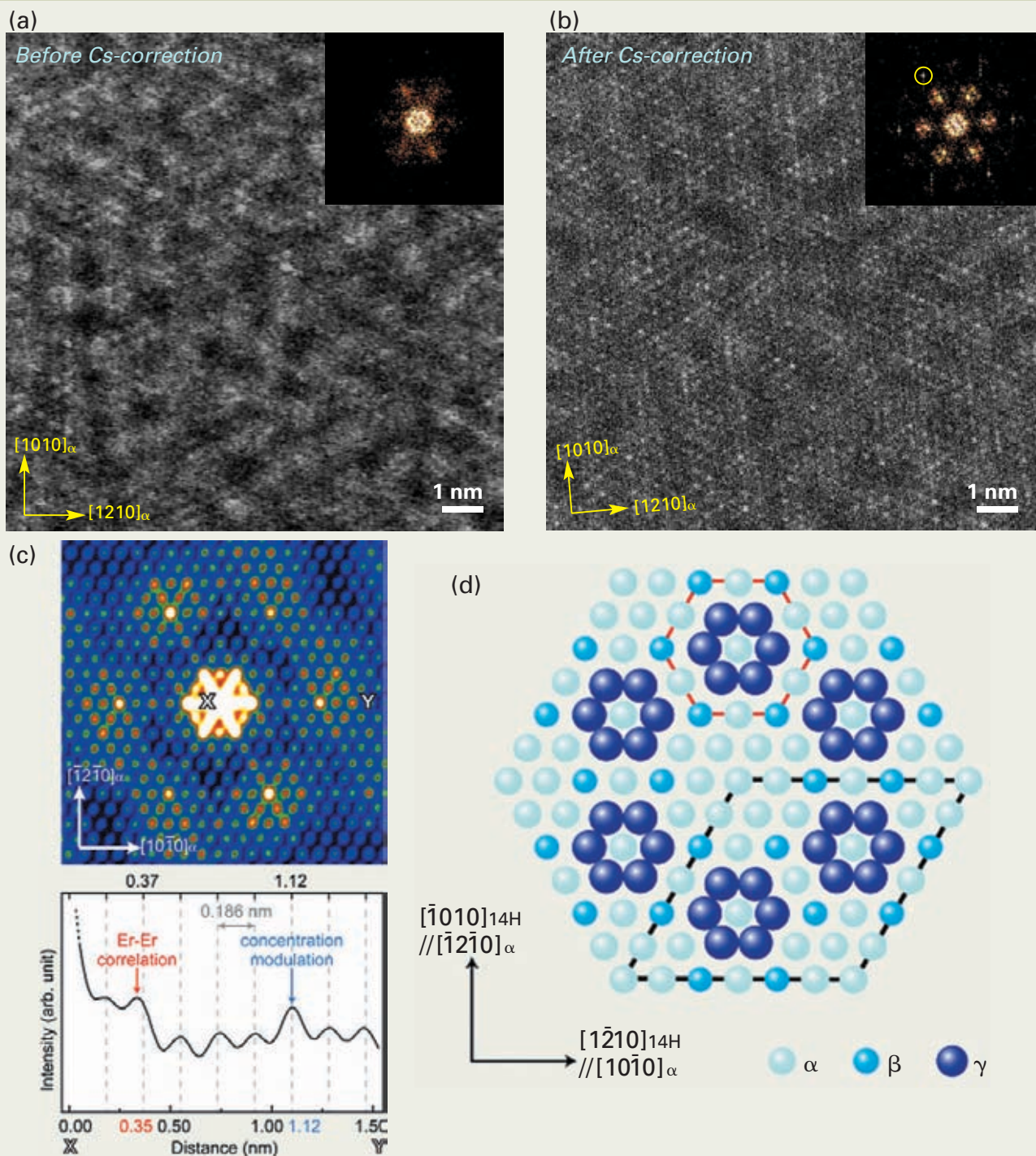


Fig. 1 Atomic-resolution Z-contrast images taken along [0001] axis of the 14H-Mg₉₇Zn₁Er₂, obtained with (a) non-Cs-corrected (JEOL JEM-2010F, Cs=0.5mm) and (b) Cs-corrected (JEOL JEM-ARM200F) STEM. (c) Auto-correlation map constructed from the Cs-corrected Z-contrast image of (b). The intensity profile across X-Y is shown below. (d) Average model of the modulated structure, where the composition at the equivalent sites are represented by α , β and γ .

tures are constructed by stacking the "structural blocks", which are represented by Haucke-unit (LaNi₅) and Laves-unit (LaNi₂). From the previous studies, it is shown that the hydrogen-storage properties of the block-stacking compounds are basically understood by different hydrogenation behaviors of the local Laves-unit/Haucke-unit within the superstructures. For controlling their compositions by the element substitutions to form the (La, X)Ni_x compounds, it becomes important to understand their favorable substitution sites and how they alter block-unit structures. These local issues are, of course, closely related to the macroscopic

hydrogen-storage properties.

Here we describe a change of local chemistry during the hydrogenations of the Y-doped (La_{0.6}Y_{0.4})₅Ni₁₉ block-stacking compound. This material is able to store the hydrogen up to ~1.1 H/M (mean number of hydrogen atoms per a constituent-metal atom), but almost the half of the stored-hydrogen will be still retained (~0.5 H/M) even after the discharging process. **Fig. 2** (a) and (b) show the atomic-resolution Z-contrast images of the (La_{0.6}Y_{0.4})₅Ni₁₉ compounds, taken from the specimens before and after a hydrogen charge-discharge process. It is clearly seen that an anisotropic lattice expansion along

the *c*-axis occurs only at the Laves (L) -unit, as shown by L'' in Fig. 2(b), suggesting that the retained-hydrogen are mostly captured in the original L-unit to transform it into the local L'' hydrides. In the L'' hydride layer, the Ni atoms originally located at the center in the L-unit are found to disappear during the hydrogenations (see the positions indicated by arrowheads in Fig. 2 (a) and (b)), revealing significantly dark Z-contrast as confirmed in the average intensity profiles (Fig. 2(c)). Interestingly, it is also noticed that the profile shows La/Y concentration modulations along the *c*-axis, which have been induced during the hydrogenation process

at room temperature. This is also confirmed by STEM-EDXS, showing significant deficiency/enrichment of Ni/Y at the L'' hydride layer, respectively (Fig. 2(d); note that the Ni concentration seems to modulate along the c-axis, but it could simply be due to a delocalization effect. We just draw the conclusion that the local Ni deficiency at the L'' layer is reasonably confirmed by STEM-EDXS with a practical spatial-resolution ~1 nm). Local hydrogen concentration can be successfully evaluated from the shift of the plasmon peaks (ΔE_p) observed between the L and L'' layers (Fig. 2(e)), estimating the possible number of hydrogen atoms to be 7~8 based on a simple free-electron approximation [8,9] and the local composition of the L'' layer as being (Y,La)₂Ni₃H₈. This is con-

firmed to be fairly reasonable values that can account for those determined by the macroscopic chemical analysis. From these systematic analyses by STEM, the change of local chemistry during the hydrogen charge-discharge process is schematically summarized in Fig. 2(f).

Direct determination of a complex quasicrystalline structure Al₇₀Mn₁₇Pd₁₃

Quasicrystals are aperiodically long-range ordered solids that exhibit rotational symmetries incompatible with conventional periodic lattice order. Their structure is often described

according to a hyperspace crystallography, which interprets the quasicrystal as a periodic structure embedded in a hyperspace. This mathematical recipe enables to calculate the diffraction intensity of any quasicrystal model structures, and accordingly the quasicrystal structures can be, in principle, determined by the x-ray diffraction analysis along the similar manner for periodic crystals.

Al-Mn-Pd alloys form a stable decagonal quasicrystal, a planar realization of the quasicrystalline order. Its structure had been intensively studied by single-quasicrystal X-ray diffraction analysis [10] as well as high-resolution phase-contrast electron microscopy [11,12], which led to the established model structure that reasonably satisfies both the observations.

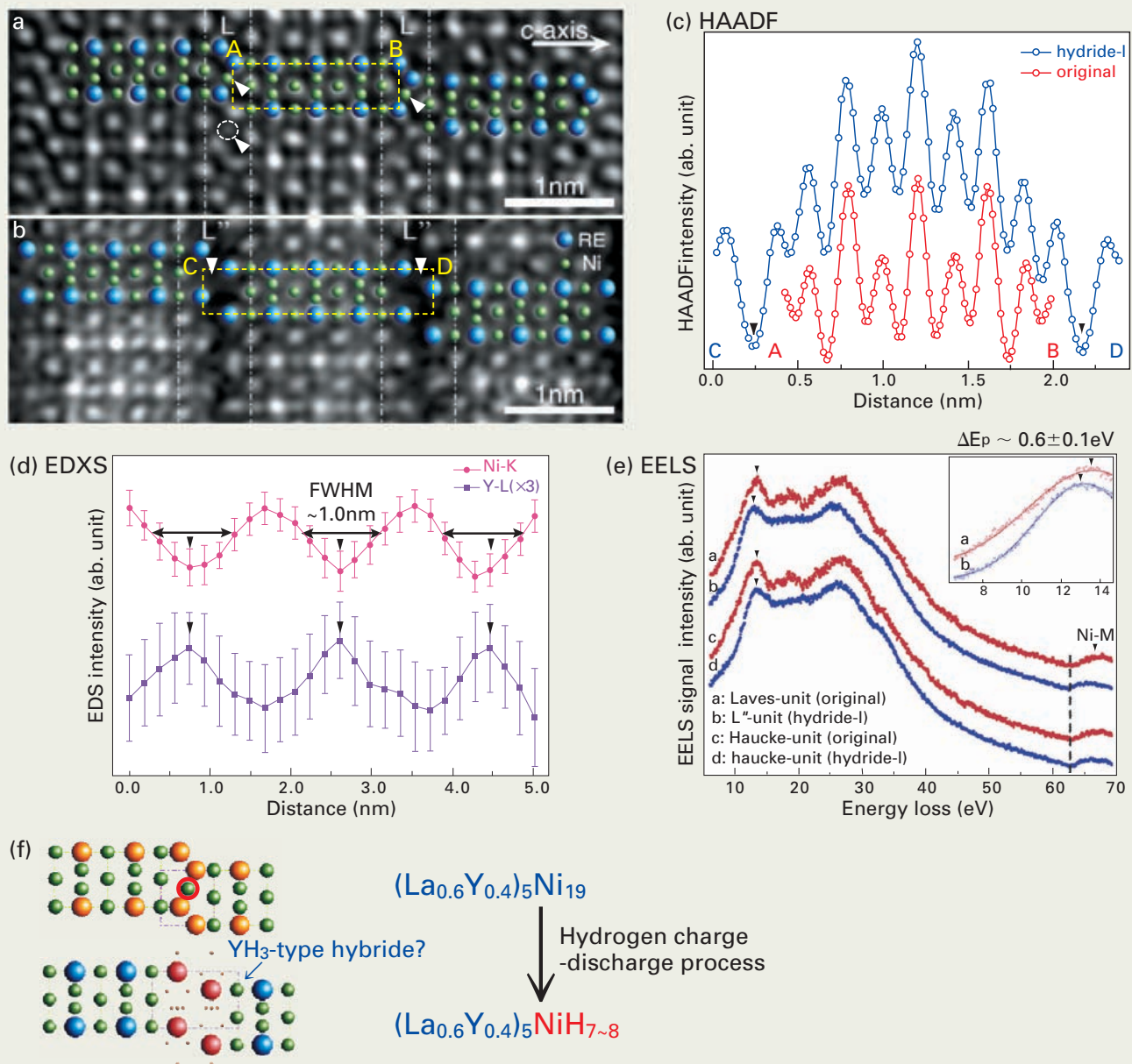


Fig. 2 Atomic-resolution Z-contrast STEM images obtained from the $(La_{0.6}Y_{0.4})_5Ni_{19}$ block-stacking compound; (a) original and (b) after the hydrogenation process. These images are taken by JEOL JEM-ARM200F. (c) HAADF/Z-contrast intensity profiles along the c-axis, obtained by integrating over the box regions A-B in (a) and C-D in (b). L'' positions are indicated by the arrowheads. (d) EDX intensity profiles along the c-axis for Ni (red) and Y (blue), where the L'' positions are indicated by arrowheads. These are taken using an electron beam with the size of approximately $\phi \sim 3$ Å (current density $> \sim 100$ pA/cm²). (e) Low-loss EEL spectra (< 70 eV) obtained from the Laves- and Haucke-units of the original and hydrogenated $(La_{0.6}Y_{0.4})_5Ni_{19}$ compounds, using the smallest electron probe ($< \sim 1.0$ Å). The origins of the spectra positions are corrected by referring the Ni-M edge (68 eV), which appears due to delocalization effects at relatively low-energy regions, even though there is no Ni atoms at the L'' layer. Significant peak shift is only observed between the original L- and L''-units, the amount of shift is estimated to be $\sim 0.6 \pm 0.1$ eV after the peak-fitting (inserted). (f) Schematic drawing of the local structural change during the hydrogenation process.

However, the ultrahigh-resolution Z-contrast STEM imaging has unveiled the local details that immediately forces to modify the existing model; see Fig. 3 (a) and (b). The observed Z-contrast distribution (Fig. 3(a)) cannot be reproduced by the simulation based on the model structure proposed by X-ray analysis [2] (Fig. 3(b)), forcing to modify the local chemical order of Al/Mn/Pd. It should be emphasized here that all the atomic sites, which are densely distributed within the complex quasicrystalline structure and occupied by the atoms of large atomic-number differences (Al: Z=13, Mn: Z=25, Pd: Z=46), are clearly imaged in Fig. 3(a) even under the Z-contrast condition. This demonstrates a remarkable performance of the present 300kV-STEM. As exemplified by the

decagonal clusters, the improved structure now fairly well reproduces the observed Z-contrast, as shown in Fig. 3(c). We are now attempting further modifications to describe the entire structure of the decagonal $\text{Al}_{70}\text{Mn}_{17}\text{Pd}_{13}$, with the aid of STEM-EELS to identify details of Mn/Pd occupations at each atomic site. The present results strongly demonstrate again the powerful use of STEM for the study of aperiodic quasicrystal structures [13-15].

Summary

We have demonstrated the remarkable performance of the state-of-the-art STEM, based on its successful application for elucidations of the multi-component complex structures. At the

age of computer-controlled aberration-corrected microscopy, for TEM/STEM experiments special master-hand techniques are not required any longer, and the sub-Å resolution is now routinely and practically available for many types of materials. Given with increasing opportunities for highly quantitative/precise microstructure analysis, we expect that the modern STEM will provide a considerable number of breakthrough results – definitely a new era of microscopic science!

References

- [1] S. J. Pennycook, D. E. Jesson, "High-resolution Z-contrast imaging of crystals", *Ultramicroscopy* **37**, 14-38 (1991).
- [2] E. Okunishi et al., *Microsc. Microanal.* **15**, (suppl. 2) 164 (2009).
- [3] H. Sawada et al., "Achieving 63pm resolution in scanning transmission electron microscope with spherical aberration corrector", *Jpn. J. Appl. Phys.* **46**, L568-L570 (2007).
- [4] H. Sawada et al., "STEM imaging of 47-pm-separated atomic columns by a spherical aberration-corrected electron microscope with a 300-kV cold field emission gun" *J. Electron Microscopy* **58**, 357-361, (2009).
- [5] E. Abe et al., "Long-period ordered structure in a high-strength nanocrystalline Mg-1at.% Zn-2at.% Y alloy studied by atomic-resolution Z-contrast STEM" *Acta Materialia*, **50**, 3845-3857 (2002).
- [6] K. Kadir, T. Sakai, I. Uehara, "Synthesis and structure determination of a new series of hydrogen storage alloys; RMg_2Ni_9 (R=La, Ce, Pr, Nd, Sm and Gd) built from MgNi_2 Laves-type layers alternating with AB_5 layers" *J Alloys Compd.* **257**, 115-121 (1997).
- [7] T. Kohno et al., "Hydrogen storage properties of new ternary system alloys: La_2MgNi_9 , $\text{La}_5\text{Mg}_2\text{Ni}_{23}$, $\text{La}_3\text{MgNi}_{14}$ " *J Alloys Compd.* **311**, L5-L7 (2000).
- [8] R. F. Egerton, *Electron Energy-Loss Spectroscopy in the Electron Microscope*, 2nd Edition, Plenum, New York, 1996.
- [9] C. Colliex et al., "Contribution of electron energy loss spectroscopy to the development of analytical electron microscopy" *Ultramicroscopy* **1**, 301-315 (1976).
- [10] S. Weber, A. Yamamoto, "Noncentrosymmetric structure of a decagonal $\text{Al}_{70}\text{Mn}_{17}\text{Pd}_{13}$ quasicrystal" *Acta Crystallographica A* **54**, 997 (1998).
- [11] K. Hiraga, M. Kaneko, Y. Matsuo, S. Hashimoto, "The structure of Al_3Mn : close relationship to decagonal quasicrystals" *Philosophical Magazine* **B67**, 193-205 (1993).
- [12] C. Beeli, S. Horiuchi, "The structure and its reconstruction in the decagonal $\text{Al}_{70}\text{Mn}_{17}\text{Pd}_{13}$ quasicrystal" *Philosophical Magazine* **B70**, 215-240 (1994).
- [13] E. Abe, A. P. Tsai, "Structure of quasicrystals studied by atomic-resolution electron microscopy" *JEOL news* **36E**, 18 - 21 (2001).
- [14] E. Abe, Y. Yan, S. J. Pennycook, "Quasicrystal as cluster aggregates" *Nature Materials* **3**, 759-767 (2004).
- [15] E. Abe, "Structure of Quasicrystals" in *STEM: Imaging and Analysis* (edited by P. Nellist and S. J. Pennycook, Springer, New York, 2010, in press).

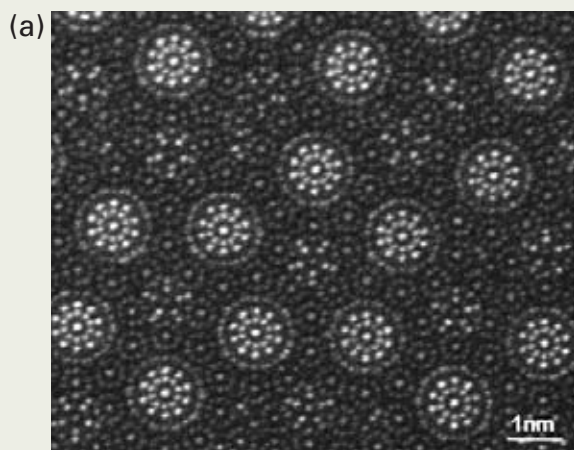
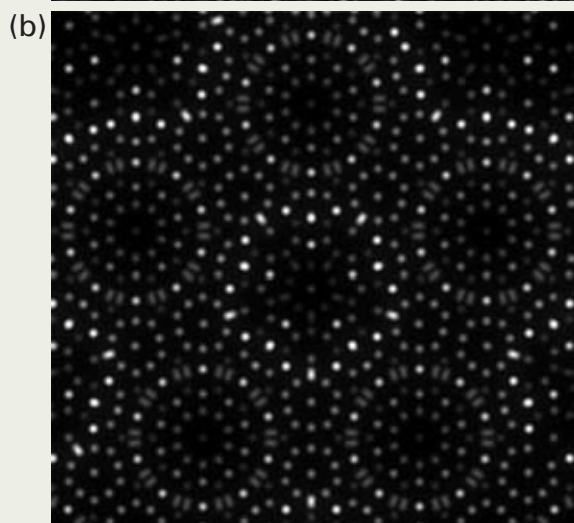
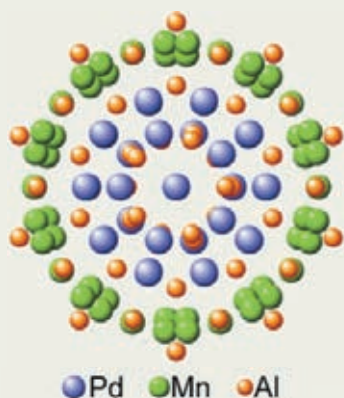


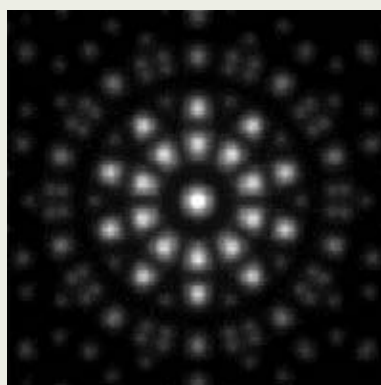
Fig. 3 (a) Atomic-resolution Z-contrast image of the decagonal quasicrystal $\text{Al}_{70}\text{Mn}_{17}\text{Pd}_{13}$, taken by the aberration-corrected 300 kV-STEM (R005 microscope equipped with the cold-field emission gun). (b) Calculated Z-contrast image based on the model structure proposed by x-ray analysis [10], revealing significantly different intensity distributions observed in (a). (c) Modified structure of the decagonal cluster and the corresponding simulated image.



(c) Revised Cluster



Simulation



Development and Applications of a Frequency Modulation Atomic Force Microscope for High-resolution Imaging in Liquids

Katsuyuki Suzuki[†], Shin-ichi Kitamura^{††},
Shukichi Tanaka^{†††}, Kei Kobayashi^{††††}, and Hirofumi Yamada^{†††††}

[†] SM Business Unit, JEOL Ltd.

^{††} Advanced Technology Department, JEOL Ltd.

^{†††} Kobe Advanced-ICT Research Center, NICT

^{††††} Innovative Collaboration Center, Kyoto University

^{†††††} Department of Electronic Science and Engineering, Kyoto University

Although dynamic mode atomic force microscopy (AFM) using frequency modulation (FM) detection technique is capable of atomic/molecular-resolution imaging in ultrahigh vacuum (UHV) environments, the imaging resolution of FM-AFM in liquids is extremely reduced by a large decrease in the Q-factor caused by hydrodynamic damping in liquids. We improved a commercial atomic force microscope (AFM) for high-resolution AFM imaging in liquids. The noise density of the improved optical beam deflection sensor was successfully decreased to 29 fm/ $\sqrt{\text{Hz}}$ at a laser power of 1 mW in liquid. In addition, the noise level and the bandwidth of the FM detector were also improved to 6 mHz/ $\sqrt{\text{Hz}}$ and 6 kHz, respectively. Thermal drift was reduced to less than 1 nm/min in air for a sufficiently long time without any special air conditioning. As a result, we succeeded in obtaining high-resolution images of a polypropylene sheet, Au thin films in water and DNA molecules in a buffer solution. The results indicated that liquid environments could provide a suitable condition for high-resolution FM-AFM imaging such as UHV environments.

Introduction

The dynamic mode atomic force microscope (AFM) using the frequency modulation (FM) detection technique [1] has been widely used for high-resolution imaging in ultrahigh vacuum (UHV) with the aid of a high Q-factor of the cantilever [2]. In fact AFM imaging in air, where the instrumental setup can be generally much simpler, is more suitable for various, practical applications. However, the true atomic/molecular resolution imaging by AFM in air is extremely difficult. A major difficulty in achieving such resolution in air AFM is that the specimen surface and/or the AFM tip can be damaged by the strong adhesion force acting between the tip and the surface due to a thin water layer of the surface. AFM imaging in liquid is a possible way for avoiding the adhesion problem and for the high-resolution imaging. High-resolution imaging with FM-AFM in liquid is again very difficult because of a large decrease in the Q-factor due to the hydrodynamic damping in liquid. Recently, several high-resolution images of mica surfaces and organic molecules including biomolecules have been successfully reported

using FM-AFM in liquids [3]. The success of high-resolution FM-AFM imaging in liquid encourages us to expand the applications of FM-AFM to new research fields.

In this study we improved a commercial AFM, JSPM-5200, and succeeded in obtaining high-resolution images of polypropylene sheet, Au thin film and DNA molecules in liquids. These results show that our improved FM-AFM has the capability of high-resolution imaging in liquids. This FM-AFM is expected to be used for a wide variety of industrial and scientific applications.

Discussion

A sufficient noise reduction in both cantilever deflection sensor and FM detection circuit is necessary for high-resolution imaging in liquids [4]. A commercial AFM (JSPM-5200) using the optical beam deflection method, as shown in **Figure 1**, was modified. **Figures 2** show photos of the improved AFM. To decrease the mode hop and the interference noises in the optical detection system, the coherence of the laser beam used for the cantilever deflection sensor was suppressed by adding a radio frequency modulation signal to the laser diode. Furthermore, the optical setup of the deflection sensor was also optimized, as shown in **Figure 3**. As a result, the noise den-

sity of the improved deflection sensor was reduced to 29 fm/ $\sqrt{\text{Hz}}$ in water at a laser power of 1 mW, which is compliant to class II a for the classification of performance standard for light-emitting products. This value is much smaller than those obtained with conventional instruments (typically 500-1000 fm/ $\sqrt{\text{Hz}}$). In addition, the noise of the phase-locked loop (PLL) circuit in the FM detector was also reduced while the frequency bandwidth was increased by the field programmable gate array (FPGA), as shown in **Figure 4**. The FM detector noise was reduced to 6 mHz/ $\sqrt{\text{Hz}}$ and the frequency bandwidth was expanded to 6 kHz. As a result, stable FM-AFM imaging in liquids can be conducted even with a small oscillation amplitude of less than 0.2 nm_{p.p.}. Moreover, the SPM head was placed in a vacuum thermo-stabilized chamber to reduce the thermal drift as shown in **Figure 5**. As a result, the thermal drift was kept at less than 1 nm/min in air for a sufficiently long time in an ordinary room where several people were walking around. Thermal drift in liquid was a little larger than in air because of the influence of the liquid evaporation. Consequently, sub-nanometer resolution images of muscovite mica surfaces in a buffer solution were successfully obtained by FM-AFM mode using our improved AFM with a small oscillation amplitude of 0.5 nm_{p.p.}, as shown in **Figure 6**.

Tokyo 196-8558, Japan

ksuzuki@jeol.co.jp



Fig. 1 JSPM-5200. The modified part is shown in Fig. 2.

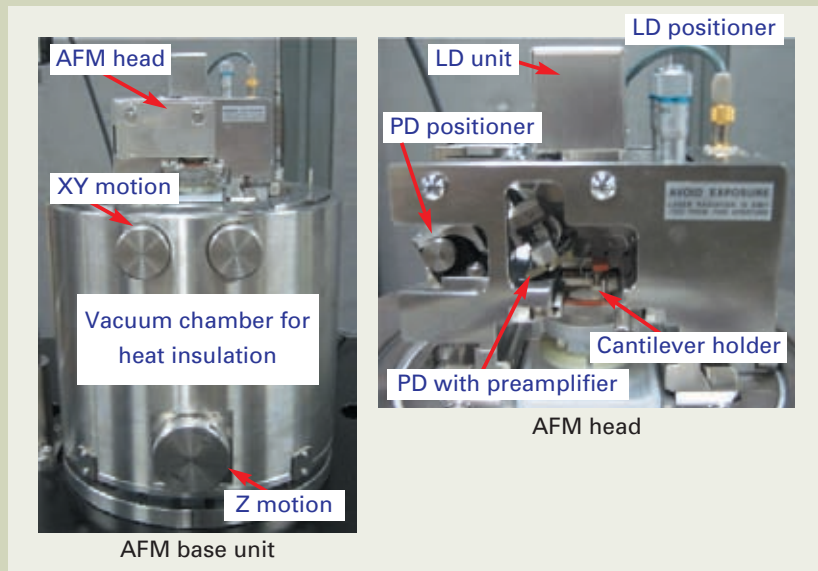


Fig. 2 High-resolution AFM for imaging in liquid.

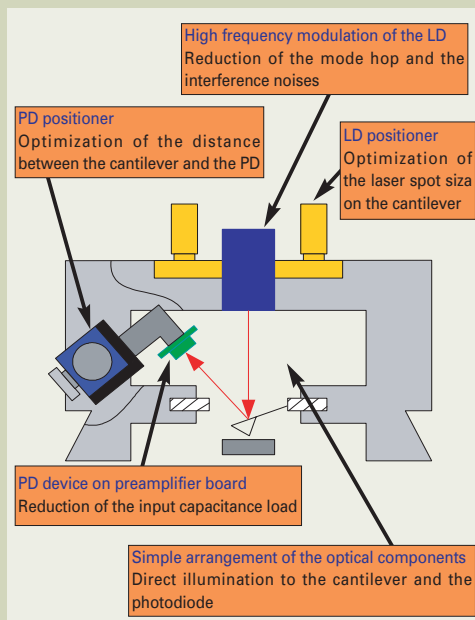


Fig. 3 Schematic diagram of the AFM head.

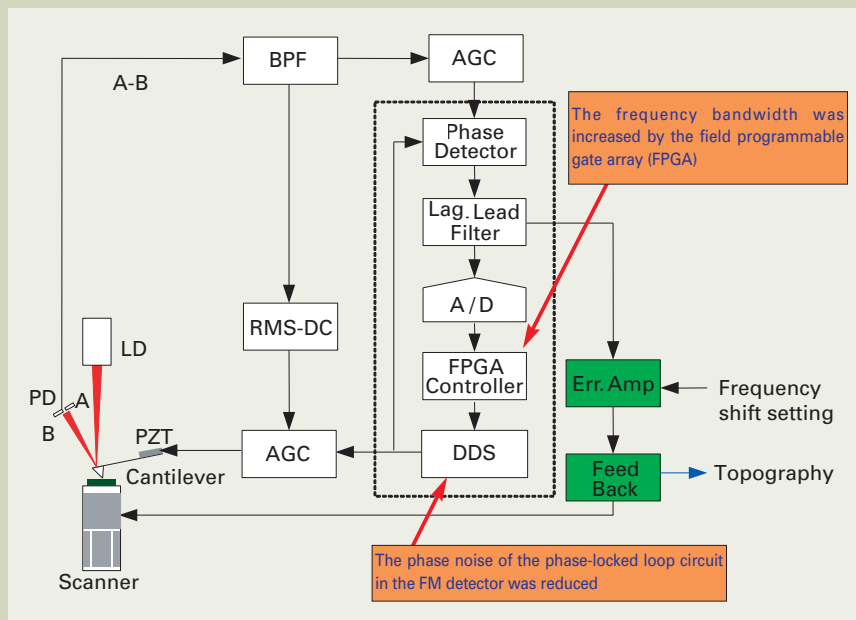


Fig. 4 The block diagram of the FM detection electronics.

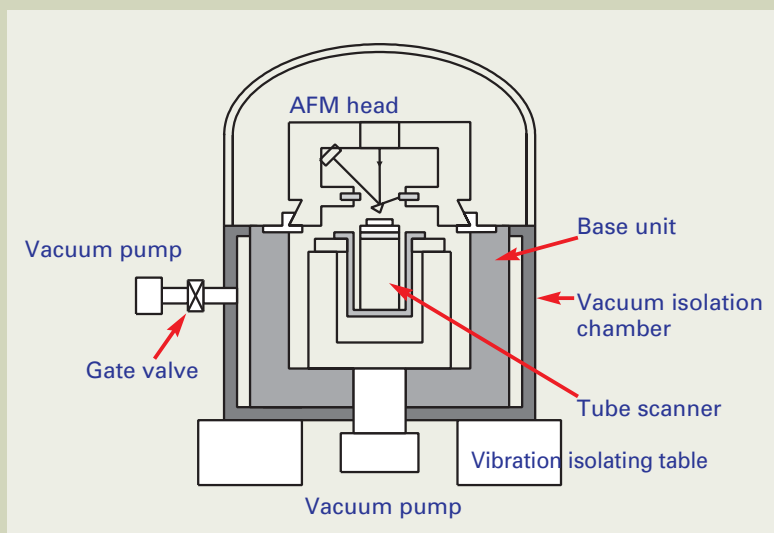


Fig. 5 Schematic diagram of the vacuum thermo-stabilized chamber.

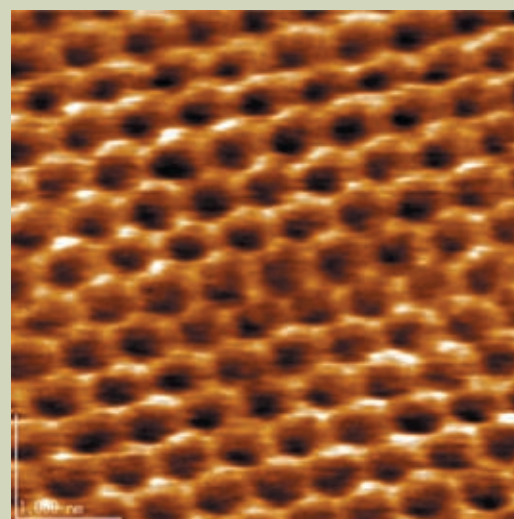


Fig. 6 FM-AFM image of a muscovite mica surface in a buffer solution (0.1mol/L KCl). Scan size is $5 \times 5 \text{ nm}^2$.

Using the improved AFM, we imaged surfaces of a polypropylene sheet and annealed Au thin films on a mica surface in a liquid. A highly doped n-Si cantilever (Nanoworld : NCH) was used as the force sensor. The peak-to-peak amplitude of the cantilever oscillation was set at a value ranging from 0.5 to 1.0 nm. First, the polypropylene sheet was observed in UHV. The results are shown in Figures 7. The polypropylene chains are clearly resolved, as shown in **Figure 7(a)**, on a (110) crystal facet in a magnified image of a fiber circled in **Figure 7(b)** [5]. **Figures 8(a)** and **(b)** show FM-AFM images of the same polypropylene sheet taken in a buffer solution (0.1mol/L KCl). An island composed of some terraces was observed in tangles of polypropylene fibers (**Fig.8(a)**). The periodic structure corresponding to the molecular array was also observed on a surface of the terrace (**Fig.8(b)**), whose spatial resolution seems to be almost comparable to the one obtained in UHV. As shown in **Figure 8(c)**, a high-resolution image was also obtained in air. However, the cantilever oscillation had to be five times larger than in the liquid to avoid the cantilever adhesion to the surface, which could have disturbed imaging of the fine structures of the sample.

Figures 9(a) and **(b)** show FM-AFM images of an annealed Au thin film on mica in the buffer solution (0.1mol/L KCl). Usually, the atomic scale images of the Au thin film surface can be obtained using UHV-STM or Electro-Chemical STM. In this experiment, the herringbone structure on a terrace was successfully observed even in liquid, as shown in **Figure 9(a)**. Furthermore, the periodic structure corresponding to the atomic array could be visualized with the size of $3 \times 3 \text{ nm}^2$ on a flat area of the surface as shown in **Figure 9(b)**.

We also successfully obtained high-resolution images of a highly orientated pyrolytic graphite (HOPG) surface in pure water. While the atomic scale images of the HOPG surface have been obtained using FM-AFM in UHV, it is pointed out that the topographic signal is quite small because of the relatively weak interaction force between the tip and the HOPG surface [6]. **Figure 10** shows an FM-AFM image of the HOPG surface taken in pure water. The peak-to-peak amplitude of the cantilever oscillation was set at 0.2 nm. The periodic structure was visualized corresponding to the periodic structure of the surface, as shown in **Figure 10**. Thus we succeeded in obtaining high-resolution images of HOPG by FM-AFM in liquid as well as in UHV.

With this advanced technique, we also imaged DNA tiles, in which several numbers of DNA strands were self-assembled and packed into two-dimensional patches [7,8]. There have been several studies on high-resolution imaging of DNA molecules in UHV [9]. However, high-resolution imaging of DNA molecules in liquid is strongly required in biological studies. This is because the structure and the properties of the DNA are stable only in physiological solution. The peak-to-peak amplitude of the cantilever oscillation was set at 1.0 nm. **Figures 11(a)** and **11(b)** show a design of a DNA tile used in this experiment and an FM-AFM image of the DNA tiles on mica in a buffer solution, respectively. As shown in **Figure 11(b)**, pairs of double strands aligned in parallel were

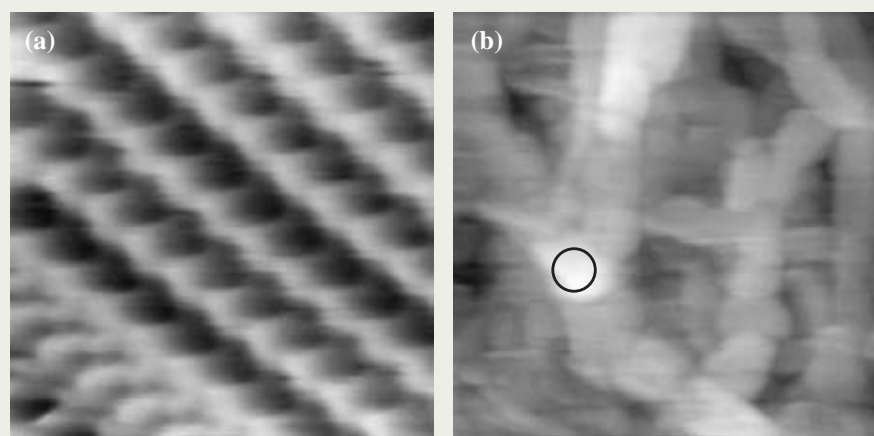


Fig. 7 FM-AFM images of a surface of a polypropylene sheet in UHV. Scan size of (a) and (b) are 5×5 and $200 \times 200 \text{ nm}^2$, respectively.

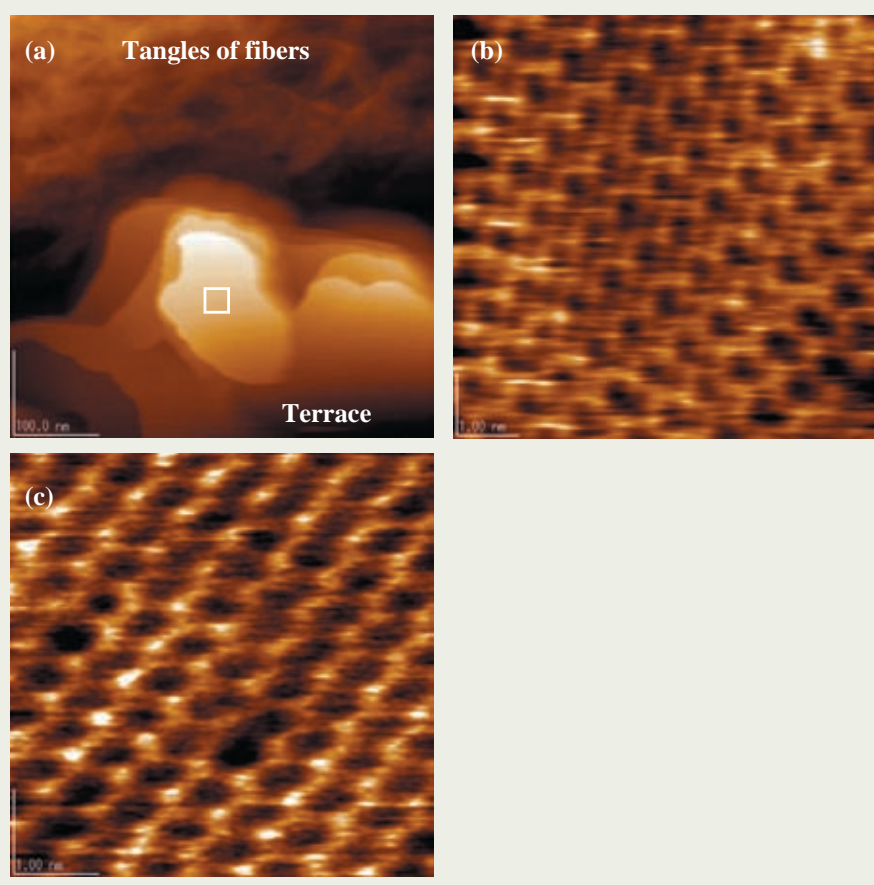


Fig. 8 Topographic images of polypropylene sheet surface taken with the FM detection mode in a buffer solution (0.1mol/L KCl) (a) (b) and in the atmosphere (c). Scan size of (a) and (b)(c) are 500×500 and $10 \times 10 \text{ nm}^2$, respectively.

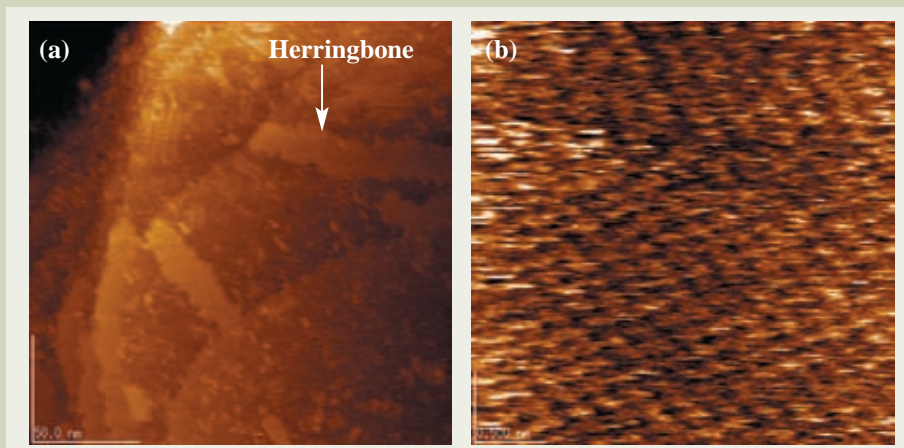


Fig. 9 FM-AFM images of a Au thin film on mica in a buffer solution (0.1 mol/L KCl). Scan size of (a) and (b) are 200×200 and 3×3 nm², respectively.

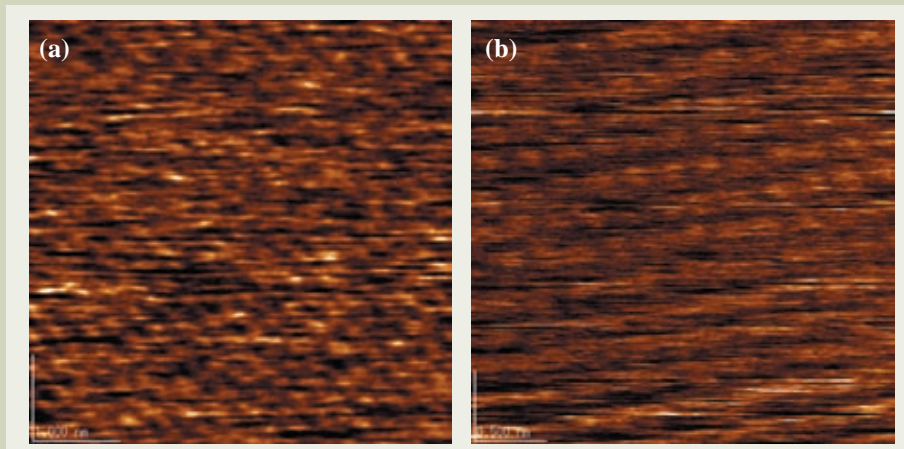


Fig. 10 FM-AFM images of highly orientated pyrolytic graphite (HOPG) surface in pure water. Scan size of (a) and (b) are 5×5 and 3×3 nm², respectively.

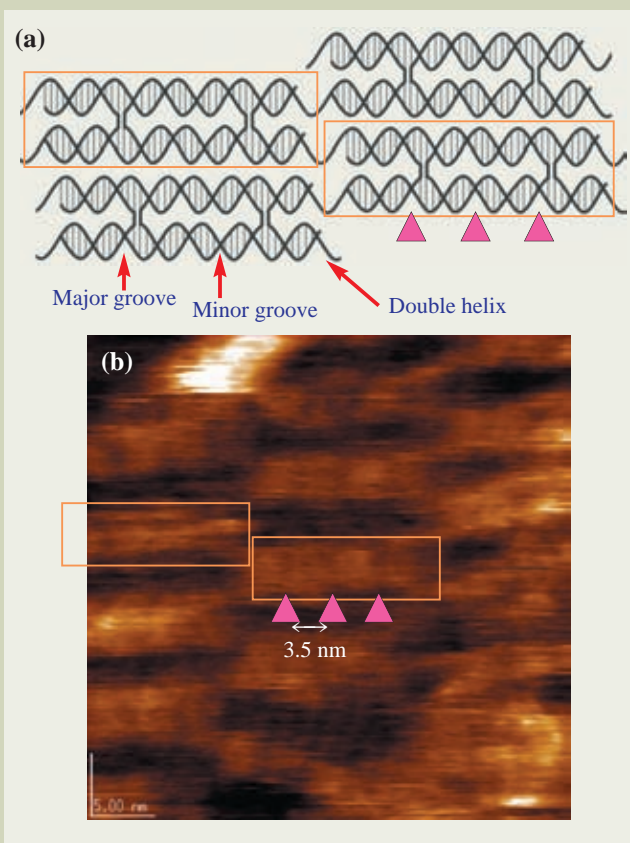


Fig. 11 (a) The design of a DNA tile used in this experiment, (b) FM-AFM image of the DNA tile on mica in a buffer solution. Scan size is 38×38 nm².

imaged as one big strip surrounded by the orange rectangles. A periodic structure with a 3.5 nm pitch, which is consistent to the periodicity of the DNA double helix model, can be clearly seen in the strip. The periodicity of DNA obtained in a previous UHV observation [9] was 4.2 nm. This difference in the periodicity is probably caused by the drying process in the specimen preparation for UHV observation.

Conclusion

We succeeded in improving our commercial AFM for high-resolution imaging of various materials in liquids. With this AFM, high-resolution images of a polypropylene sheet and an Au thin film were reproducibly obtained in liquid. The spatial resolution in these images was comparable to that in the typical images of the same samples taken in UHV. Furthermore, the double strand structure of the DNA double helix was observed in liquid, which had not been obtained in UHV. The present success in obtaining high-resolution images of the several sample surfaces in liquid indicates that the liquid environment is a quite suitable and promising environment to perform high-resolution AFM imaging. Thus it can be the alternative to the UHV environment for high-resolution FM-AFM observation.

Acknowledgements

We wish to express our appreciation to Dr. Furuta at Kobe Advanced-ICT Research Center for supplying DNA.

References

- [1] T. R. Albrecht, P. Grutter, D. Home, and D. Rugar: *J. Appl. Phys.* **69**, 668 (1991)
- [2] S. Kitamura, K. Suzuki, and M. Iwatsuki: *Jpn. J. Appl. Phys.* **37**, 3765-3768 (1998)
- [3] T. Fukuma, K. Kobayashi, K. Matsushige, and H. Yamada: *Appl. Phys. Lett.* **87**, 034101 (2005)
- [4] T. Fukuma, K. Kobayashi, K. Matsushige, and H. Yamada: *Appl. Phys. Lett.* **86**, 193108-1 (2005)
- [5] M. Iwatsuki, K. Suzuki, S. Kitamura, and M. Kersker: *Microsc. Microanal.* **5**, 208-215 (1999)
- [6] S. Kawai, H. Kawakatsu: *Phys. Rev.* **B 79**, 115440 (2009)
- [7] M. Tagawa, K. Shohda, K. Fujimoto, T. Sugawara, and A. Suyama: *Nucleic Acids Res.* **35**, (21), e140 (2007)
- [8] DNA tiles used in the liquid FM-AFM observation was synthesized and supplied by Dr. Ken'ya Furuta of Kobe Advanced-ICT Research Center, NICT, Kobe.
- [9] Y. Maeda, T. Matsumoto, H. Tanaka, and T. Kawai: *Jpn. J. Phys.* **38**, L1211-L1213 (1999)

JEM-2100: Applications in Nanotechnology

Judith Grinblat

Bar-Ilan Institute of Nanotechnology and Advanced Materials

This article sums up a two-year experience of employing a JEOL JEM-2100 (LaB₆) high resolution electron microscope for structural characterization of nano-materials. The instrument was integrated with a scanning device comprising ADF and BF detectors and with an EDS system for elemental analysis. Despite the fact that the microscope was installed in a small room without a special basement, with a standard air-conditioner, and no special precautions were taken to avoid variations in air temperature or to attenuate sound-and-vibration disturbances, the microscope has provided excellent around the clock performance.

In the HRTEM mode it was possible to achieve lattice resolution of 1.17 Å; the resolution capability of the instrument afforded by STEM was about 10nm. The capabilities of the system are demonstrated in a few examples of nano-materials research applications.

Introduction

It is widely recognized that transmission electron microscopy is one of the central techniques used for characterization of nano-materials. Recent advances and improvements in the field of high resolution electron microscopy and microanalysis tools allowed the achievement of remarkable progress in research and development of materials on the nanometer scale. Today most nano-laboratories are equipped with modern electron microscopes that allow one to combine HRTEM, STEM, HAADF-STEM, EELS and EDS within a single instrument. Ultimate performance of such systems strongly depends on the properties and characteristics of the electron source. The latest generations of the microscopes are usually based on a field emission gun which, in comparison with thermionic electron sources, is characterized by substantially higher electron current density, better coherency, smaller energy spread and, therefore, has an obvious advantage in forming a fine and bright electron probe. This allows one to obtain not only high quality high resolution images, but also affords better analytical sensitivity for EDS and EELS analysis that manifests itself in providing rich local chemical information with better spatial resolution. In the absence of a field emission gun, a high resolution transmission electron microscope with a conventional LaB₆ gun can also be very effective in performing most of the routine works aimed at the characterization of nano-materials structure.

In this paper we report on our experience in use of JEOL JEM-2100 (LaB₆) electron microscope with HT pole-pieces that was installed at the Bar-Ilan Institute of Nanotechnology and Advanced Materials

(BINA) in 2008. The instrument equipped with Noran System Six EDS system for elemental analysis and integrated with a scanning device comprising ADF and BF detectors, became a multi-disciplinary "workhorse" providing services for investigations in the nano-field encompassing a wide variety of topics. Below we demonstrate the excellent performance of the microscope and present some results showing its contribution to our studies of nano-materials.

The Microscope room and the operating environment

The installation of the microscope was completed in August 2008. It was installed on the ground floor without any special separation from the building foundation, in a room which barely meets the minimal accommodation requirements. The AC fields at the site were within the acceptable norm (less than 1 m Gauss), the HT tank and power supply block were placed at the distance of about 1.5 m from the microscope column. Water chiller and UPS unit generating noise and heat were set outside the room. The main problem that we faced was that of cooling the room without causing significant air flow that would disturb the microscope performance. We installed a standard air-conditioning unit set at about 21 °C with the outlets arranged to blow the cooled air away from the microscope column.

Although no particular precautions were undertaken to attenuate acoustic noise coming from the computers and cooling systems of the electronic equipment and despite slight variations in the air temperature of the room, the microscope provided excellent around the clock performance. This is demonstrated in **Figure 1a** which shows the high resolution image of TiO₂ nano-particles coated with an amorphous Al₂O₃ layer obtained by atomic

layer deposition. As follows from the Fourier transform (see inset) taken from the area outlined by the square, the lattice fringes with spacing as fine as 1.17 Å could be observed. Such lattice resolution achieved with our instrument appears to be even better than that specified in the official table of the key-features published for JEM-2100 (LaB₆) microscope (lattice resolution 0.14 nm).

The ability of the instrument to detect image features with faint contrast is demonstrated in **Figure 1b** where the 2-3 nm thick amorphous Al₂O₃ coating of an individual TiO₂ nano-particle is clearly seen.

Another example is related to the performance of the instrument in STEM mode which we usually employ with EDS elemental mapping or line scan to provide information on the chemical composition of very small volumes of material. **Figure 2** shows the STEM image of the cross-section of the amorphous SiO₂ layer deposited on the crystalline Si <100>, prepared by FIB technique [1]. Ge⁺ ions were implanted into the SiO₂ layer and the subsequent annealing process gave rise to the growth of nano-crystalline particles of Ge. The image clearly shows well separated nano-particles of Ge and the line scan profile for the elements Ge (yellow), Si (green) and O (red). According to the size of the smallest particles, we can estimate that the resolution capability of the instrument afforded by STEM is about 10 nm.

Applications in nano-materials research

The Bar-Ilan institute of Nanotechnology & Advanced Materials (BINA) is engaged in advanced scientific research and technological applications in the field of nano-science and technology. The institute includes six research centers: Nano-Materials, Nano-Medicine, Nano-Energy, Nano-Photonics, Nano-Magnetism and

Bar-Ilan University, Ramat Gan 52900 ISRAEL

grinby@mail.biu.ac.il

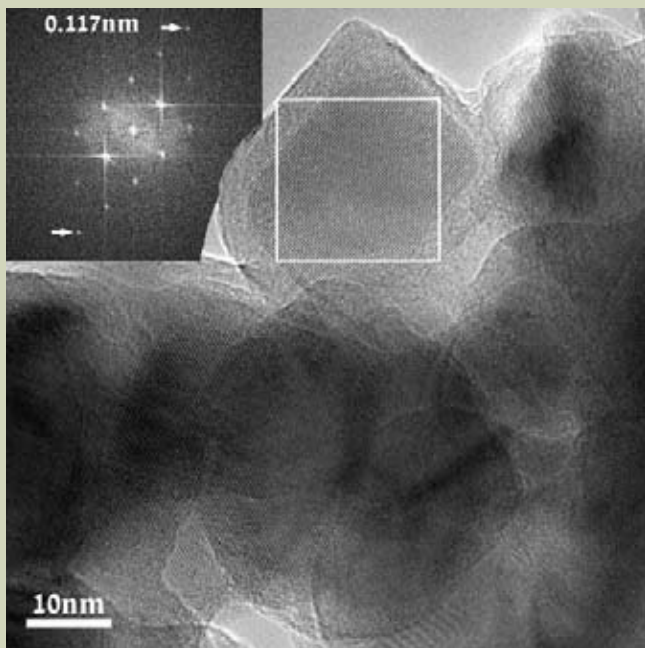


Fig.1a(left) High Resolution electron micrograph of crystalline TiO_2 nano-particles coated with an amorphous layer of Al_2O_3 . The inset is the Fourier transform of the portion of the image marked by the white square.

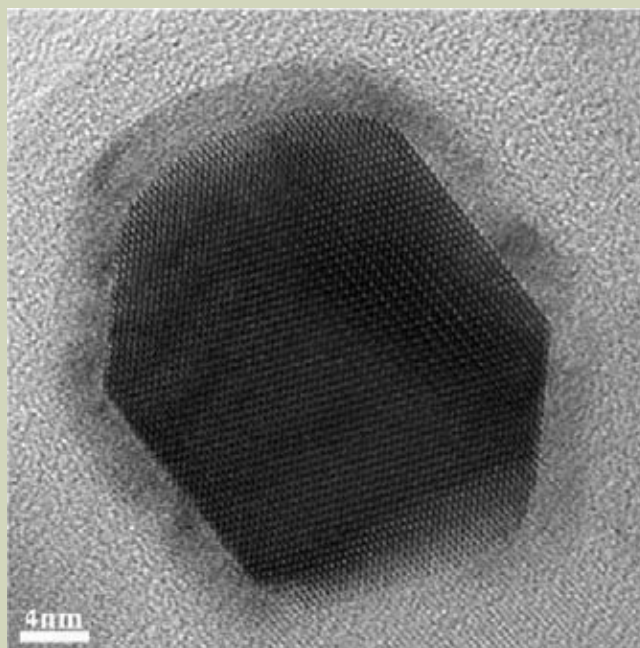


Fig.1b(right) High resolution image of an individual TiO_2 nano-particle coated with an amorphous layer of Al_2O_3 .

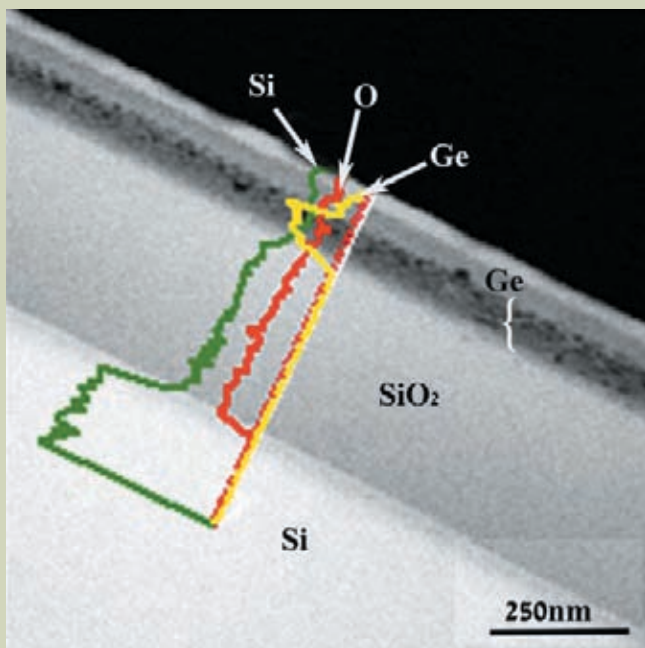


Fig.2 STEM bright field image of the cross-section of the amorphous SiO_2 layer deposited on the crystalline $[100]\text{Si}$. Nano-crystalline particles of Ge formed by implantation of Ge^+ ions and subsequent annealing are clearly seen in SiO_2 layer. Elemental Line Scans are shown for: Ge- yellow, Si-Green and O-red.

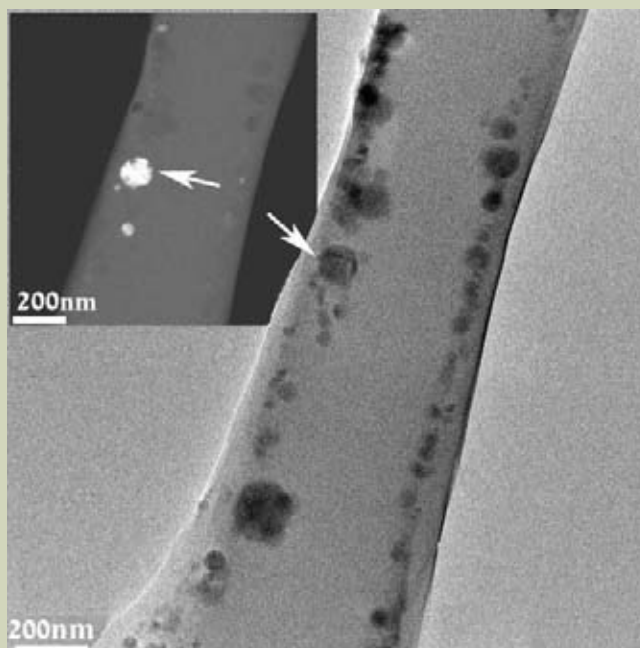


Fig.3 Bright field electron micrograph of a fiber coated with Al_2O_3 nano-particles. The inset is the dark field image of the fiber showing a few crystalline nano-particles of Al_2O_3 .

Nano-Clean-tech. Forty research groups from a variety of disciplines (such as chemistry, physics, life science and engineering) are active within these centers.

It will be difficult in the framework of this paper to refer to the great variety of routine investigations conducted at BINA. Instead, a few examples of non-standard applications will be given.

Characterization of the antibacterial Al_2O_3 nano-composite coatings [2].

This example represents research in which

nanotechnology was involved in creating unusual properties in textile material, such as antibacterial properties. For this purpose nano-particles of Al_2O_3 were deposited on fabrics by sonochemical irradiation technology [3].

From the coated cotton material, specimens for microscopic examination were prepared using the epoxy embedding technique and ultra microtome cutting.

A JEM-2100 (LaB_6) electron microscope was used to analyze the particles' morphology and size. Two particular features characterize this study: (a) the low-dose imaging technique was applied because of instability of the epoxy cross

sections under the electron beam, (b) it was impossible to identify the Al_2O_3 nano-particles by conventional electron diffraction technique, since the diffraction reflections were very weak. Therefore high resolution images of nano-particles showing lattice fringes and Fourier transform of these images were used in the analysis of the particles' structure.

The fiber coated with Al_2O_3 is shown in the TEM micrograph in **Figure 3**. A few individual Al_2O_3 crystalline nano-particles are clearly visualized in the Bright field, and in the Dark field (see inset) images.

The STEM capabilities of the microscope

allowed the application of an elemental mapping technique for analysis of the distribution of Al_2O_3 nano-particles over a coated material. **Figure 4** demonstrates the results of Al-mapping which, in fact, shows the Al-containing particles covering the fiber (Al-blue).

The identification of the nano-particles was based on the analysis of their high resolution images. An example is given in **Figure 5** showing a high resolution image taken from the particle marked by the arrow in Figure 3. Inset (a) represents the magnified portion of the image outlined by the white square. The distances measured between lattice fringes were 0.28 nm, 0.25 nm and 0.25 nm matching, respectively, the interplanar spacings d_{220} , d_{131} , and d_{311} in the orthorhombic δ - Al_2O_3 structure (the dimensions of the unit cell are $a = 7.934 \text{ \AA}$, $b = 7.956 \text{ \AA}$, $c = 11.75 \text{ \AA}$, [4]). Inset (b) is the computed Fourier transform of the image in inset (a) which, like a diffraction pattern, was indexed on the basis of the unit cell of δ - Al_2O_3 structure.

Investigation of materials for advanced lithium-ion batteries [5,6]

The JEM-2100 (LaB₆) microscope was used in the study of a variety of electrode materials for rechargeable Li-ion batteries. The materials based on the LiMPO_4 compounds ($M = \text{Fe, Mn, Co, or Ni}$) [7] are considered as particularly promising, and among them mixed-transition-metal olivine compounds, such as $\text{Li}(\text{Mn,Fe})\text{PO}_4$, exhibit excellent performance. Intensive investigations of these materials were carried out at Bar-Ilan University by the electrochemistry group, one of the leading groups in the field. We present herein some results of the electron microscopic study of the structure of a carbon coated $\text{LiMn}_{0.8}\text{Fe}_{0.2}\text{PO}_4$ compound which was synthesized by a solid-state reaction [5]. Presumably, the carbon coating enables the active mass to have excellent electronic conductivity and also serves as a barrier against detrimental surface reactions between the active mass and solution species.

The high resolution electron micrograph in **Figure 6** shows a typical carbon-coated nano-particle of the $\text{LiMn}_{0.8}\text{Fe}_{0.2}\text{PO}_4$ compound. The core-shell structure of the nano-particle is clearly seen: the core is the crystalline $\text{LiMn}_{0.8}\text{Fe}_{0.2}\text{PO}_4$ compound and the thin shell is a coating layer of graphitic carbon (~5 nm thick). It is worth noting that the contrast of the image enables good visualization of the carbon layer coating the $\text{LiMn}_{0.8}\text{Fe}_{0.2}\text{PO}_4$ nano-particle, despite the background due to the presence of carbon substrate.

The EDS spectrum (**Figure 7**) taken from a ~25 nm area shows that Mn, Fe, P, O and C are all present in the sample. An atomic ratio of 3.6:1 calculated for Mn and Fe is in good agreement with the expected ratio of 4:1 found in high resolution SEM.

The structure of the nano-particle was identified using the computed Fourier transform of the portion of the image within marked area (white square in Figure 6).

The "reflection spots" on the Fourier transform (inset in Figure 6) were successfully indexed in terms of the orthorhombic unit cell [6] ($a = 10.414 \text{ \AA}$, $b = 6.081 \text{ \AA}$, $c = 4.73 \text{ \AA}$) that

represents the structure of both LiFePO_4 and LiMnPO_4 compounds. Because these compounds are structurally similar they could not be distinguished in the high resolution image of the core of the particle. It was therefore suggested that the material should be considered as a solid solution of LiMnPO_4 and LiFePO_4 compounds which are integrated and interconnected

with one another at the atomic level.

The study of the structure of nano-composite solar cells [8,9]

Development of nano-composite solar cells as an alternative to existing silicon photovoltaic devices has become a very attractive sub-

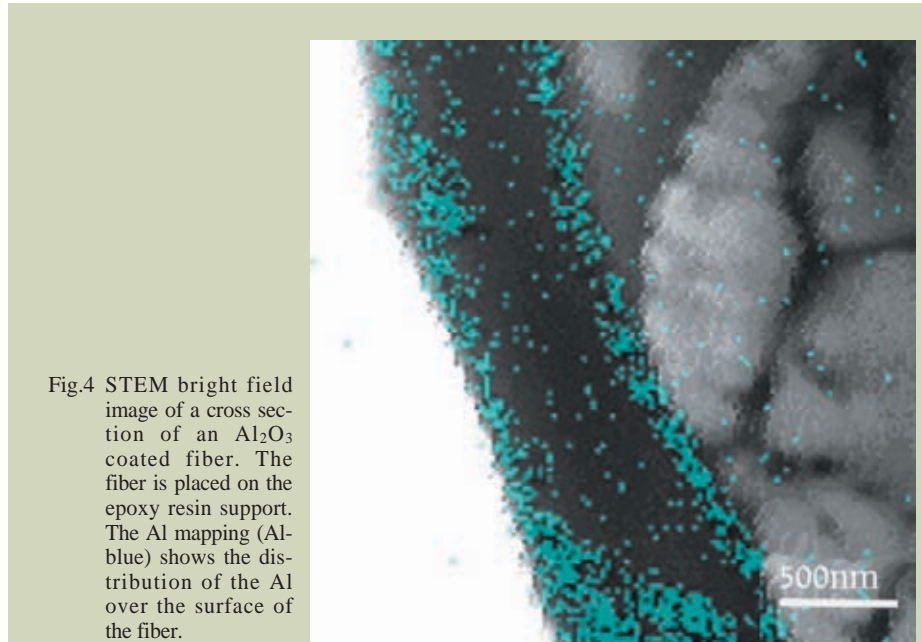


Fig.4 STEM bright field image of a cross section of an Al_2O_3 coated fiber. The fiber is placed on the epoxy resin support. The Al mapping (Al-blue) shows the distribution of the Al over the surface of the fiber.

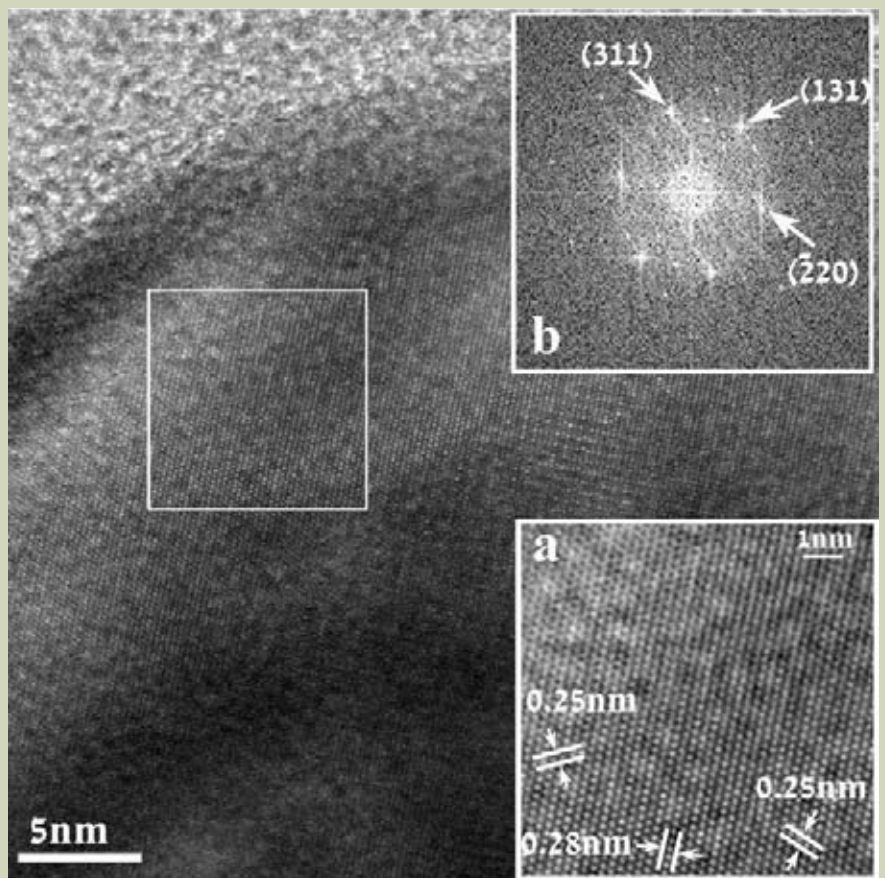


Fig.5 High resolution electron micrograph of the Al_2O_3 particle marked by the arrow in Figure 3. Inset (a) shows the magnified image of the area outlined by the white square. Inset (b) is the indexed Fourier Transform taken from the area shown in inset (a). The indexing corresponds to the structure of an Al_2O_3 compound.

ject. In the nano-composite solar cell, quantum dots can act as photo-absorbers which inject charge carriers from their excited state into adjacent electron and hole conducting media.

In the present work, quantum dots of CdS were deposited by chemical bath deposition onto the surface of mesoporous film (core

material) consisting of interconnected TiO₂ nano-crystals. In order to improve the performance of the solar cells, an additional thin layer of amorphous TiO₂ was deposited onto the quantum dots-sensitized core.

There was a significant challenge to characterize the morphology, chemistry and crystallographic structure of all constituents of the

obtained nano-composite material because the extremely small size of the CdS and TiO₂ nano-particles, about 5-10 and 20-40 nm respectively. Moreover, it was important to identify the amorphous TiO₂ layer which was approximately 2 nm thick. These tasks were successfully fulfilled using our JEM-2100 LaB₆ electron microscope.

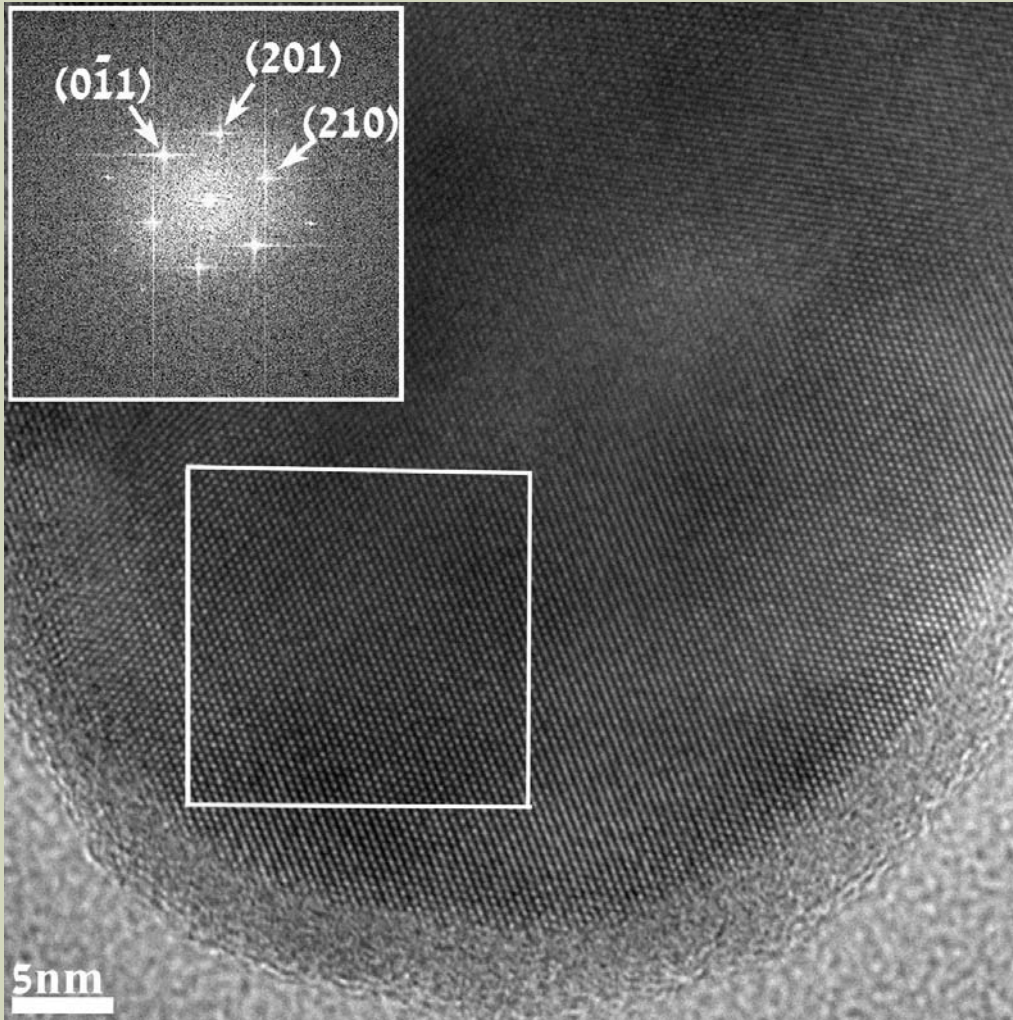


Fig.6 High resolution micrograph of a carbon coated nano-particle of LiMn_{0.8}Fe_{0.2}PO₄. A 5 nm thick carbon coating is clearly seen. The inset is the computed Fourier Transform taken from the marked area, showing sets of reflections corresponding to the interplanar spacing, d_{210} , d_{201} and d_{011} in the orthorhombic structure of LiMn_{0.8}Fe_{0.2}PO₄.

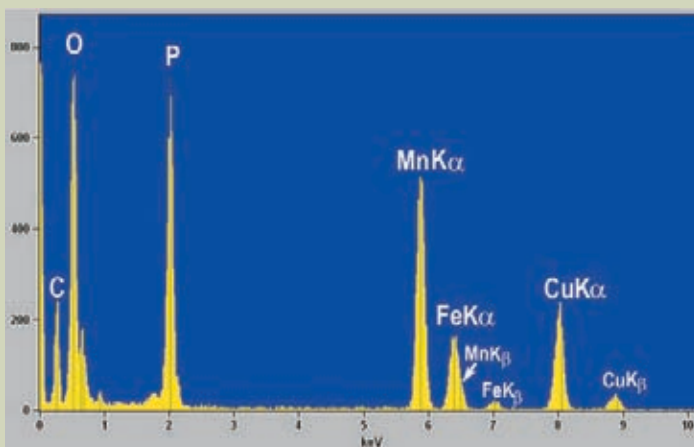


Fig.7 EDS spectrum recorded from nanoparticles of LiMn_{0.8}Fe_{0.2}PO₄, showing characteristic peaks of elements C, O, P, Mn and Fe. The Cu peak is from the specimen grid.

Figure 8 represents a high resolution electron micrograph taken from mesoporous TiO₂ film sensitized with the quantum dots of CdS. In this micrograph TiO₂ and CdS crystalline nano-particles display typical lattice-fringe contrast, and the amorphous TiO₂ shell is also distinguishable, exhibiting a faint contrast, slightly brighter than the rest of background. The Energy dispersive X-ray spectrum obtained with the relatively large electron probe (30 nm in diameter) shows the presence of Ti, Cd, S and O elements in the film. However, the brightness of the LaB₆ electron source was not high enough to allow using sub-nanometer probe size in order to identify individual nano-particles of TiO₂ and CdS quantum dots. Therefore, Fourier analysis of the lattice images was the only available tool to provide identification of TiO₂ and CdS nano-particles. This is illustrated in the two insets, (a) and (b), showing Fourier transform patterns taken from the areas numbered, correspondingly, 1 and 2 in the image. The pattern in the inset (a) was indexed on the basis of a tetragonal unit cell of anatase TiO₂ ($a = 3.78 \text{ \AA}$, $c = 9.5 \text{ \AA}$), while the pattern in the inset (b) was unambiguously indexed in terms of a hexagonal structure describing CdS (cell parameters: $a = 4.15 \text{ \AA}$, $c = 6.73 \text{ \AA}$). This was sufficient proof of the presence of CdS and TiO₂ nano-particles in the sample.

Analysis of magnetic iron and iron oxide particles entrapped within nano-porous microspheres. [10]

In this study transmission electron microscopy was used for analyzing the mor-

phology, elemental content and structure of the magnetic micro-particles entrapped within nano-porous microspheres. Nano-porous materials are widely used as adsorbents, catalyst supports and biocompatible materials. Incorporating magnetic components within the porous material can give rise to many new applications, such as cell separation, enzyme immobilization, diagnostics, molecular biology, MRI contrast agents, drug targeting etc.

In this work, uniform magnetic microspheres were synthesized by entrapping iron salts into the nano-pores of the microspheres fabricated from cross-linked poly-divinyl benzene (PDVB) [10]. The microspheres were then annealed in air at 250 °C, and in argon atmosphere at 500 °C and 800 °C. **Figure 9** shows the STEM bright field images with the iron mapping (iron in red) of the microspheres annealed at 250, 500 and 800 °C. It can be seen that increasing the annealing temperature results in a decrease in the size of the microspheres.

The structure of the iron containing particles was investigated in TEM mode using either conventional selected area diffraction (SAD) technique or Fourier analysis of high resolution images, depending on the size of the particles.

Inset (a) in **Figure 10** is an electron micrograph of a typical microsphere with entrapped particles that was prepared at annealing temperature 500 °C; the enlarged area outlined by the white square is shown in inset (b). The EDS elemental analysis of this area with a probe of 25 nm has shown the presence of iron, oxygen and carbon. The high resolution image and the corresponding Fourier transform taken from the particle marked by the arrow in inset (b) are shown in insets (c) and (d), respectively. The Fourier pattern was

indexed in terms of the unit cell of Fe₃O₄ (cubic FCC $a = 8.35 \text{ \AA}$).

Summary

The capabilities of high resolution transmission electron microscope JEOL JEM-2100 with a conventional LaB₆ gun allow the effective employment of the instrument in most of routine structure studies of nano-materials. Nano-particles as small as 5-10 nm can be unambiguously identified by Fourier analysis of high-resolution images combined with elemental X-ray microanalysis. This is demonstrated through several examples of investigations in the field of nano-technology that were carried out at Bar-Ilan Institute of Nanotechnology and Advanced Materials. Indexing of the Fourier transform patterns was successfully used for identifying the Al₂O₃ nano-particles of antibacterial coatings, the LiMn_{0.8}Fe_{0.2}PO₄ nano-particles in materials for rechargeable batteries, the TiO₂ nano-particles with CdS quantum dots in nano-composite solar cells and Fe₃O₄ nano-particles entrapped within nano-porous microspheres fabricated from PDVB. The STEM facility of the microscope coupled with elemental mapping technique allowed analysis of the distribution of Al₂O₃ nano-particles in antibacterial coatings and viewing nano-sized particles of Ge in amorphous SiO₂ layer. We have also demonstrated the ability to observe the fine details with low-contrast, such as the 5 nm carbon layer deposited on the LiMn_{0.8}Fe_{0.2}PO₄ particles and the 2 nm thick layer of amorphous Al₂O₃ on TiO₂ crystalline nano-particle.

Acknowledgement

The author wishes to thank Prof. M.

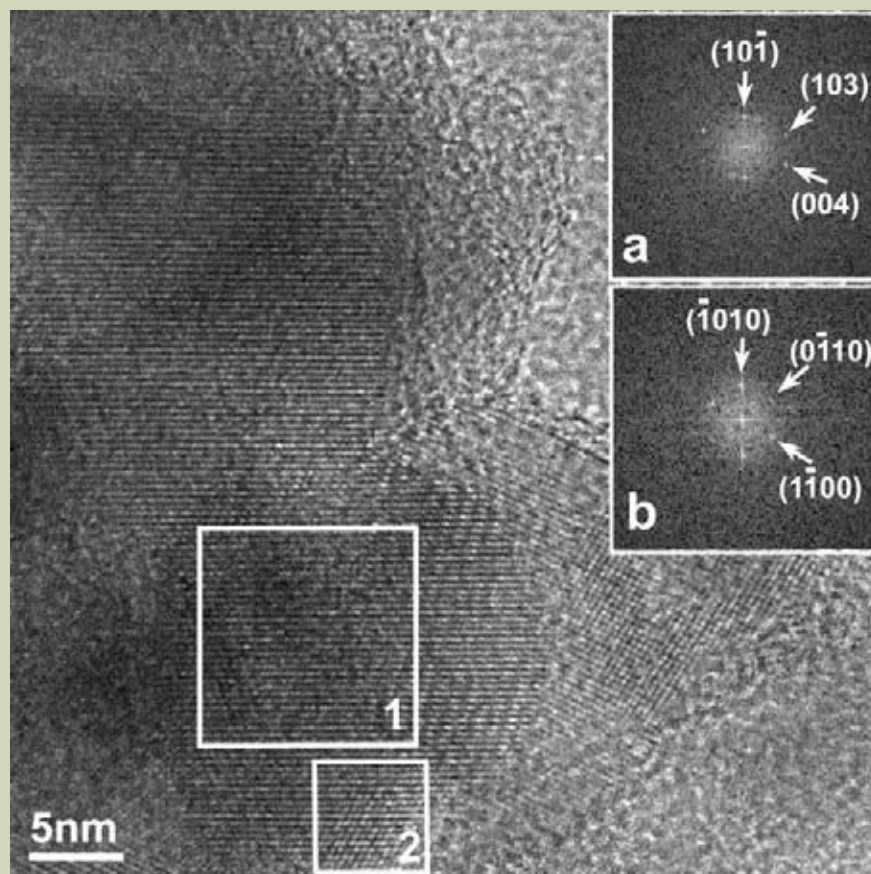


Fig.8 HRTEM image taken from a mesoporous TiO₂ film sensitized with quantum dots of CdS. Insets (a) and (b) are Fourier transform patterns taken from the areas numbered 1 and 2 respectively. The pattern in inset (a) was indexed on the basis of tetragonal unit cell of anatase TiO₂, and the pattern in inset (b) was indexed in terms of hexagonal structure of CdS.

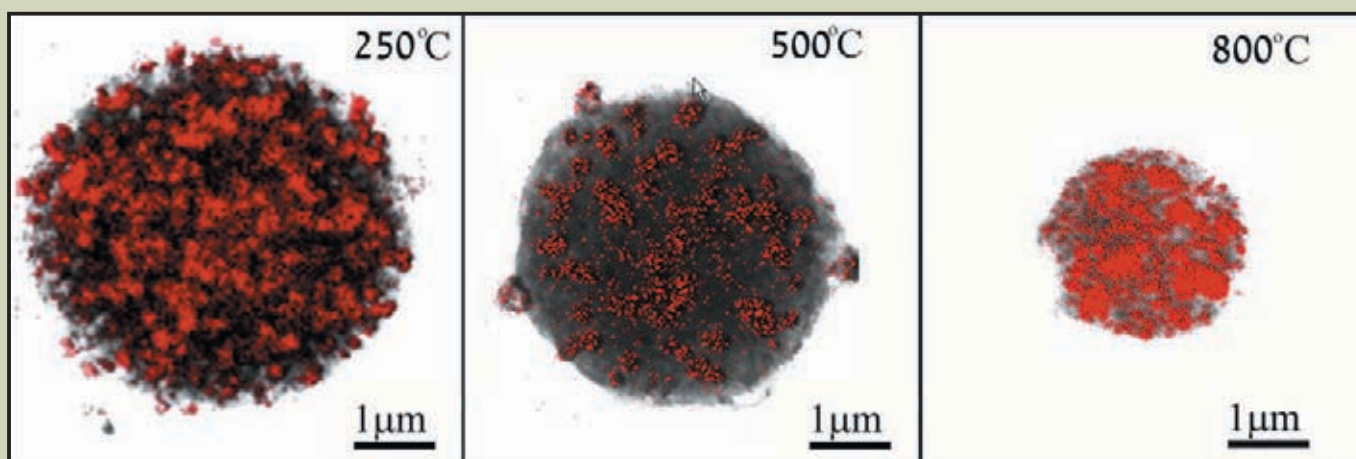


Fig.9 Scanning transmission electron micrographs displaying the Fe-K α distribution map within the microspheres fabricated from PDVB with entrapped nano-particles of iron oxide (red). The images correspond to annealing temperatures 250, 500 and 800 °C. Increasing the annealing temperature results in a decrease in the size of the microspheres.

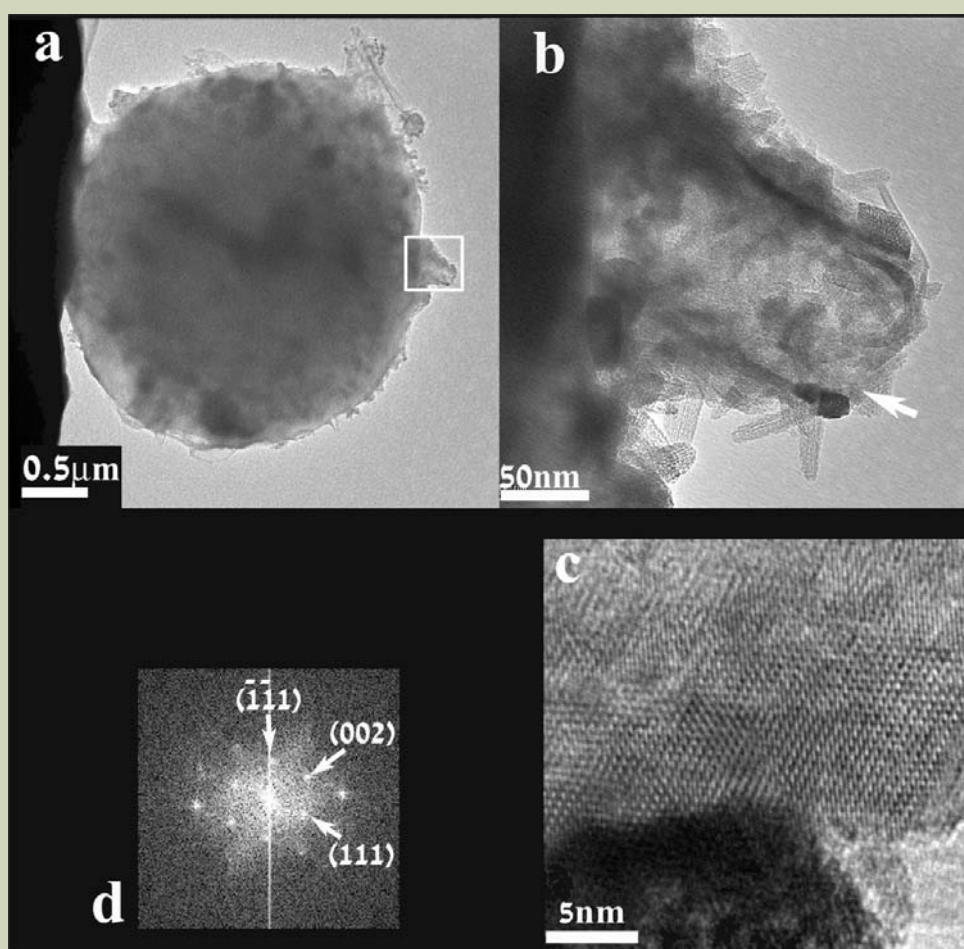


Fig.10 Electron micrograph representing an individual PDVB microsphere with nano-pores containing iron (annealing temperature is 500 °C). Insets show: (a) the general view of the microsphere; (b) the enlarged area outlined by white square in the inset (a); (c) the high resolution image of the particle marked by arrow; (d) Fourier transform taken from the high resolution image. The indexing of the Fourier pattern shows that particle is Fe₃O₄.

Talianker for his valuable assistance in writing this article. The author acknowledges Mr. S. Levy, Dr. I. Perlshtein, Dr. S. K. Martha, Dr. B. Markovsky, Mr. M. Shalom and Mr. D. Amara for their cooperation and contributions to this paper. They appear as authors in each referenced paper. Special thanks to Prof. D. Aurbach for his encouragement and support and to Dr. M. Ben-Tzion who offered valuable editorial comments.

References

- [1] Levy, S.; Shlimak, I.; Chelly, A.; Zalevsky, Z.; Lu, T.; *Physica B*, **404**, 5189, (2009).
- [2] Perelshtein, I.; Applerot, G.; Perkas, N.; Grinblat, J.; Hulla, E.; Wehrsuetz-Sigl, E.; Hasmann, A.; Guebitz, G.; Gedanken A.; *Green Chemistry*, In Press.
- [3] Gedanken, A. *Ultrasonic Sonochemistry*, **11**, 47 (2004).
- [4] Pattern # No. 046-1215, Powder diffraction database PDF-2 (Set 53, Release 2003), International Centre for Diffraction Data, Newton Square PA, (2003).
- [5] Martha, S. K.; Grinblat, J.; Haik, O.; Zinigrad, E.; Drezen, T.; Miners, J.H.; Exnar, I. Kay, A.; Markovsky, B.; Aurbach, D.; *Angew. Chem. Int. Ed.* **48**, 8559, (2009).
- [6] Martha, S. K.; Markovsky, B.; Grinblat, J.; Gofer, Y.; Haik, O.; Zinigrad, E.; Aurbach, D.; Drezen, T.; Wang, D.; Deghenghi, G.; Exnar, I.; *J. Electrochem. Soc.*, **156**, A541 (2009)
- [7] Chung, S.-Y.; Bloking, J. T.; Ching, Y.-M.; *Nature Materials*, **1**, 123, (2002).
- [8] Shalom, M.; Ru'hle, S.; Hod, I.; Yahav, S.; Zaban, A.; *J. Am. Chem. Soc.*, **131**, 9876, (2009)
- [9] Shalom, M.; Dor, S.; Ru'hle, S.; Grinis, L.; Zaban, A.; *J. Phys. Chem. C*, **113**, 3895 (2009).
- [10] Amara, D.; Grinblat, J.; Margel, S.; *J. Materials. Chem.*, **20**, 1899, (2010).

Development of JMS-S3000: MALDI-TOF/TOF Utilizing a Spiral Ion Trajectory

Takaya Satoh

MS Business Unit, JEOL Ltd.

We have developed the JMS-S3000, matrix assisted laser/desorption ionization time-of-flight mass spectrometer (MALDI-TOFMS). An innovative ion optical system, which achieved a spiral ion trajectory, surpassed basic specification of the reflectron ion optical system presently used in most commercially available TOFMSs. Furthermore, we have developed the TOF-TOF option for the JMS-S3000. In the case of attaching the TOF-TOF option, a spiral ion optical system is adopted for the first TOFMS, whereas a reflectron ion optical system with offset parabolic reflectron is adopted for the second one. Utilizing the spiral trajectory ion optical system, the JMS-S3000 provides unprecedentedly high mass resolution and high precursor ion selectivity. In this paper, we demonstrate not only the high mass resolution of more than 60,000 (FWHM) at m/z 2093 but also achievement of high mass resolution over a wide mass range. In addition, we present the high selectivity that enables selection of monoisotopic ions of precursor ions. By selecting only monoisotopic ions of precursor ions, one signal peak corresponding to each fragmentation channel is observed on a product ion spectrum. Consequently, the analysis of the product ion spectrum is made clearer.

Introduction

The time-of-flight mass spectrometer (TOFMS) is one of mass spectrometry techniques, which include the quadrupole mass spectrometer, the magnetic sector mass spectrometer, the ion trap mass spectrometer and the Fourier transform ion cyclotron resonance mass spectrometer. In the case of TOFMS, ions of various m/z values, which are generated in the ion source, are accelerated to the detection plane by a pulse voltage applied from a starting time of data acquisition. Since the time-of-flight of ions at the detection plane are proportional to the square root of their m/z values, the ions generated in the ion source can be separated. One of the TOFMS feature is fast measurement, which is due to the unnecessary of scan for any physical parameters such as electric or magnetic fields. Recently, not only a single type mass spectrometer, but also a tandem type mass spectrometer connected with the quadrupole mass spectrometer (Q/TOF) or tandemly connected two TOFMSs (TOF/TOF) are available.

The mass resolution of TOFMS is expressed

by $T/2\Delta T$, where ΔT is the time-of-flight distribution of the ion group with the same m/z value (ion packet) at the detection plane (that is, spatial distribution of the ion packet in the flight direction at the detection plane) and, T is centroid of the time-of-flight distribution. Since TOFMS was invented in 1964 [1], its mass resolution has been improved by increasing T and decreasing ΔT . In 1955, a unique acceleration technique was developed, which focuses the initial space and energy distributions at the detector surface in the flight direction. Applying this technique, the mass resolution was increased by decreasing ΔT [2]. Furthermore, in the early 1970s, a new technique was developed. In this technique, the focus position defined by the above-mentioned acceleration technique is chosen as the start point, and an ion optical system that is composed of ion mirror [3] or electrostatic sectors [4] is placed at the post stage. This innovation made it possible to increase the time-of-flight T without increasing ΔT , and led to a dramatic improvement of the mass resolution. Recently, most of commercially

available TOFMS instruments use ion mirrors, and their flight paths are 1 to 3 m. For further improvement in the mass resolution of TOFMS, another types of ion optical systems have been proposed. They are the multi-reflecting type [5] and the multi-turn type [6-7] ion optical system where ions fly multiple times on the certain trajectory. These two ion optical systems theoretically achieve an infinitely long flight path in a compact space, and improved the mass resolution. However, they have the limitation of the mass range because ions with large speed (ions with small m/z) lap the ions with small speed (ions with large m/z) when the ions flying on the same trajectory multiple times.

We have developed an original ion optical system that utilizes a spiral ion trajectory. This ion optical system can overcome the "lap" problem present in multi-reflecting and multi-turn type ion optical systems. In addition, it is possible to achieve mass resolution and mass accuracy higher than those of widely used reflectron ion optical systems. In this paper, we describe the design of the spiral trajectory

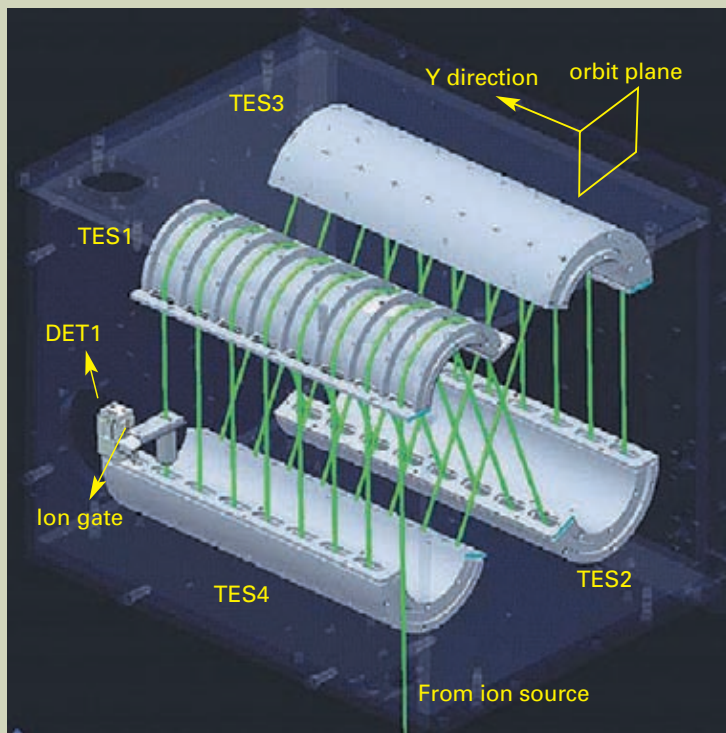


Fig. 1 Spiral ion trajectory ion optical system.

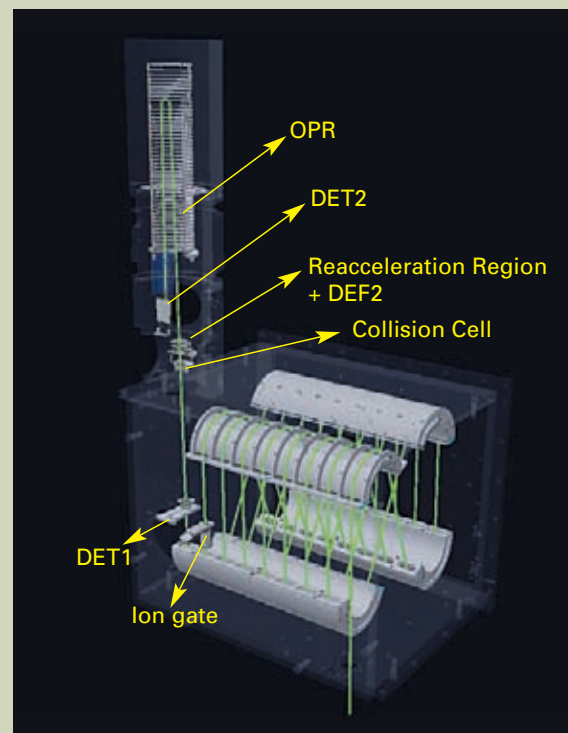


Fig. 2 MALDI-TOF/TOF utilizing the spiral ion trajectory ion optical system.

type ion optical system, and basic performance of a MALDI-TOF/TOF system applying it. The system consisted of the spiral trajectory type ion optical system and reflectron type ion optical system using offset parabolic reflectron for the first and second TOFMSs, respectively. The instrument achieves higher mass resolution, mass accuracy and precursor ion selectivity due to utilizing a spiral ion optical system for the first TOFMS, thus enabling more precise analysis.

Design of the spiral trajectory ion optical system

Multi-turn type ion optical system technique was applied for development of the spiral trajectory ion optical system. Especially, a combination of the "perfect focusing" and "multi-turn" [12] techniques developed at Osaka University, which achieved highest mass resolution in the world, was considered the most suitable for development of the spiral trajectory ion optical system. For conversion of a multi-turn type ion optical system for a spiral trajectory ion optical system, it is necessary to move ion trajectory perpendicular to the orbit plane. In order to achieve this, we have designed the system so that ion injection is slightly tilted to the orbit plane. The advantage of the design is that there is no need for the mechanism to transfer the ions to the next layer. There are concerns about degradation of mass resolution due to the trajectory deviation from a multi-turn type ion optical system. However, the effect should be negligible by keeping the injection angle to several degrees.

Practically, we have designed the spiral trajectory ion optical system based on MULTUM II [7] construction, which consists of four toroidal electrostatic sectors (cylindrical

electrodes with two Matsuda plates). The schematic of the ion optical system is shown in Fig. 1. To achieve a spiral trajectory, we have constructed a layered toroidal electric field (TES) by placing (number of cycles + 1) Matsuda plates into the cylindrical electrostatic sectors. The Matsuda plates are arranged within certain equal distances L_y in the space L_x between the external and internal electrodes. The three types of voltages applied on TESs 1 to 4 is that of the internal electrode, external electrodes and Matsuda plates. Corresponding voltages are supplied to every Matsuda plates, internal and external electrodes of TESs 1 to 4.

Also, four TESs were placed so that they correspond to MULTUM II when looked from the orbit plane. Y direction was set perpendicular to the periodic orbit plane. In development of the MALDI-TOF/TOF, we have made Y direction to horizontal. The TES1 in the Fig. 1 shows the external electrode is removed so that it can be seen the Matsuda plates are equally spaced. Ions fly through the center of the space, formed by L_x and L_y . Ion passes the same layer of TESs 1 to 4, and after passing the TES 4, it enters to the next layer of TES 1. The process is repeated for several cycles; the ion thus draws a spiral trajectory and reaches the detector (DET1) (Green line in the Figure 1 represents the ion trajectory). The injection angle θ into the layered toroidal electric field can be expressed as follows,

$$\tan \theta = (L_y + L_m) / L_c \dots \dots \dots (1)$$

where, L_m is the thickness of a Matsuda plate and L_c is the one cycle length.

As mentioned above, owing to the usage of four TESs of the same structure in its construction, the ion optical system can achieve a com-

plicated trajectory within a simple structure.

Production of MALDI-TOF/TOF utilizing spiral trajectory ion optical system

We have developed MALDI-TOF/TOF utilizing the spiral trajectory ion optical system. It consisted of the first TOFMS using the spiral trajectory ion optical system and the second TOFMS using the reflectron ion optical system. The mass spectrum measurement in the first TOFMS is referred as spiral mode, and the product ion spectrum measurement in the second TOFMS as TOF/TOF mode.

An schematic of the system is shown in Fig. 2 (ion source and the detector DET1 of the first TOFMS are omitted). Spiral trajectory is set to eight cycles of 2.093 m per each. A distance between central trajectories of the adjacent layers is 58 mm, an injection angle is 1.6 degree according to equation (1). Y direction is set as horizontal, so the injection angle is achieved by tilting the extraction direction of the ion source 1.6 degrees from a horizontal plane.

In the spiral mode, ions fly a spiral trajectory and are detected with the spiral mode detector (though not specified in Fig. 2, it is located similarly to DET1 in Fig. 1). Ion gate is placed in the 7th cycle. It allows eliminating high-intensity matrix ions, which are outside of the data acquisition m/z range.

In TOF/TOF mode, selection width of the ion gate is made narrower and monoisotopic ions of precursor ions are selected out of all isotopic ions of them. It is possible to mechanically move the spiral mode detector out of the trajectory so that precursor ions can be introduced into the collision cell. Ions, that entered a collision cell, collide with rare gas inside of the cell with a kinetic energy of approximately

20 keV, and generate fragment ions. Precursor ions and fragment ions are mass-separated in a reflectron ion optical system that combines an offset parabolic reflectron (OPR) [13] and a reacceleration mechanism. OPR is a reflectron connecting a linear and parabolic electric fields. It allows simultaneous observation of ions, from low m/z fragment ions up to precursor ions. In addition, in order to increase transmission of ions, fine adjustment of the ion trajectory is enabled by installing two deflectors (DEF1 and DEF2) on both sides of the collision cell.

Evaluation of MALDI-TOF/TOF with spiral trajectory ion optical system utilized

Figure 3 shows mass spectrum of six types of peptide mixtures (in order of m/z increase: Bradykinin fragment 1-7, Angiotensin II, Angiotensin I, P14R, ACTH fragment 1-17, ACTH fragment 18-39). The mass spectrum of Angiotensin II and ACTH fragment 1-17 are also displayed as an enlarged image. Mass resolution is 58000 (FWHM) and 73000 (FWHM) respectively. The mass error of ACTH fragment 1-17 is 0.16 ppm, when internal calibration is performed among five peptides except ACTH fragment 1-17. It became clear from the above mentioned facts that distance of flight for spiral trajectory ion optical system is 17 m, which is 5 times longer than that of the conventional reflectron type ion optical systems. This allows enhance-

ment of mass resolution and mass accuracy.

Figure 4 shows the relation between m/z value and mass resolution when mass resolution is adjusted with ACTH fragment 1-17. Figure 4 shows that it is possible to achieve high mass resolution simultaneously in a wide m/z range. This overcomes the problem of MALDI-TOFMS utilizing conventional reflectron type ion optical system that could achieve high mass resolution only in a narrow m/z range.

Figure 5.a shows a product ion spectrum diagram of Poly (oxypropylene), acquired in TOF/TOF mode. Selected precursor ions are monoisotopic ions from $[M+Na]^+$ series with m/z 1027. A numbers of fragmentation channels from sodium ions as fragment ion to precursor ion are observed. The enlarged spectrum around m/z 780 is shown in Fig. 5.b. The system is able to select only monoisotopic ions of precursor ions, therefore each fragmentation channels can be observed as one peak without any isotopic peaks. Two peaks in Fig. 5.b indicate different fragmentation channels. It indicates that 2u different fragmentation channels can be clearly separated. Figure 5.c displays an image of the same m/z range as in Fig. 5.b when measured with conventional MALDI-TOF/TOF. Precursor ion selectivity of traditional TOF/TOF is insufficient so that the fragment ions from all isotopic ions of precursor ions are analyzed in the second TOFMS. Thus every fragmentation channels of product ion spectrum include isotopic peaks. As a result, when m/z values of monoisotopic ions of two fragment channels are close, such as 2 u, their isotopic peaks are overlapped and are

impossible to be clearly identified. The high precursor ion selectivity originated from the spiral trajectory ion optical system used in this system makes the structural analysis of chemical compounds much easier.

Conclusion

This paper reports on the development of the spiral trajectory ion optical system. Also, the paper describes the development of MALDI-TOF/TOF, which combines a spiral trajectory ion optical system and reflectron type ion optical system utilizing offset parabolic ion mirrors. Innovative ion optical system introduced to the JMS-S3000 has overcome preexisting problems related to conventional MALDI-TOF and MALDI-TOF/TOF. Thus, the JMS-S3000 is expected to play a significant role in various areas.

References

- [1] W. E. Stephens. *Phys. Rev.*, **69**, 691 (1946)
- [2] W.C.Wiley and I. H. McLaren, *Rev. Sci. Instrum.*, **26**, 1150 (1955).
- [3] B. A. Mamyurin, V. I. Karataev, D. V. Shmikk and V. A. Zagulin, *So. Phys. JETP*, 3745(1973).
- [4] W. P. Poschenrieder, *Int. J. Mass Spectrom. Ion. Phys.*, **6**, 357 (1972).

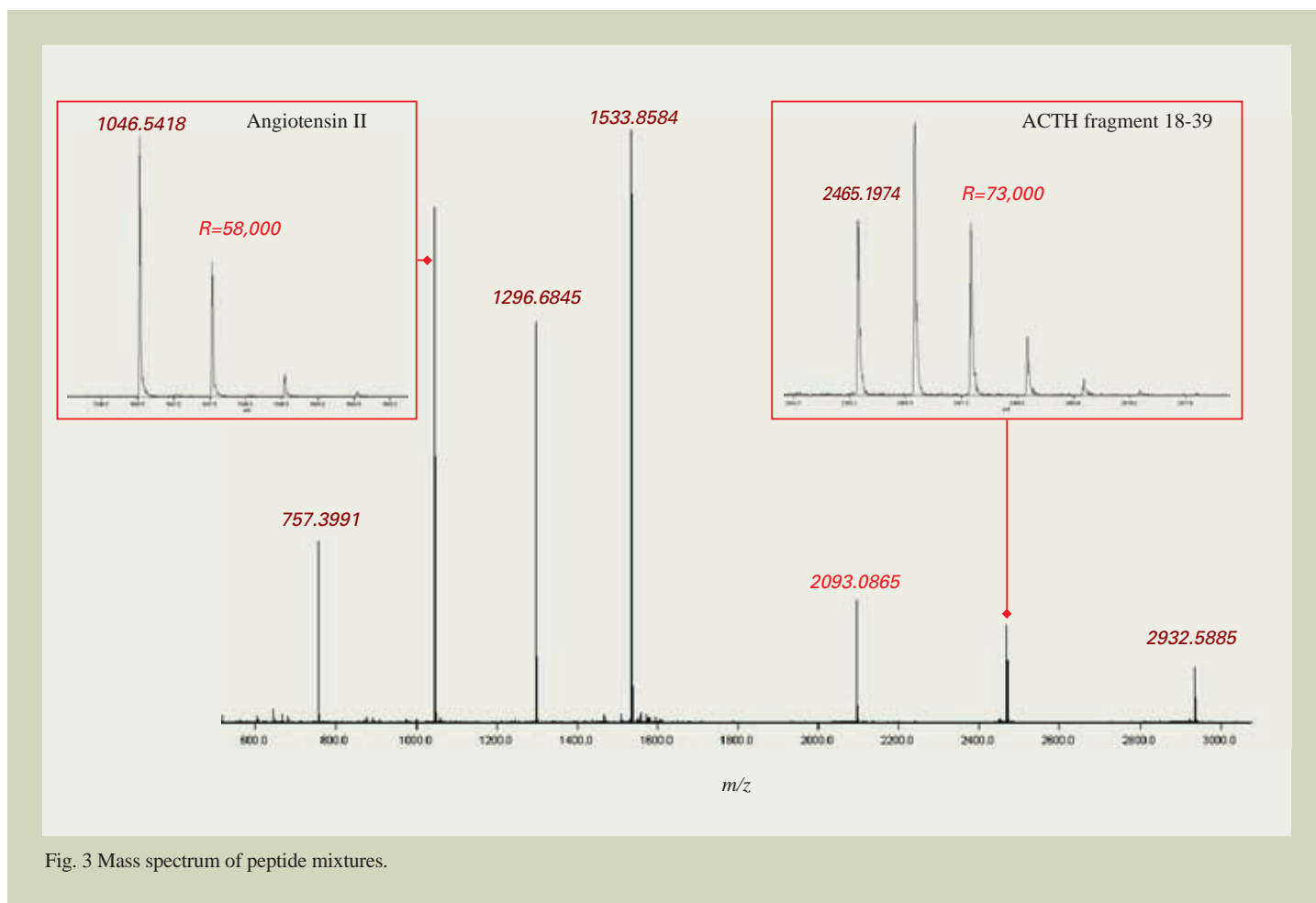


Fig. 3 Mass spectrum of peptide mixtures.

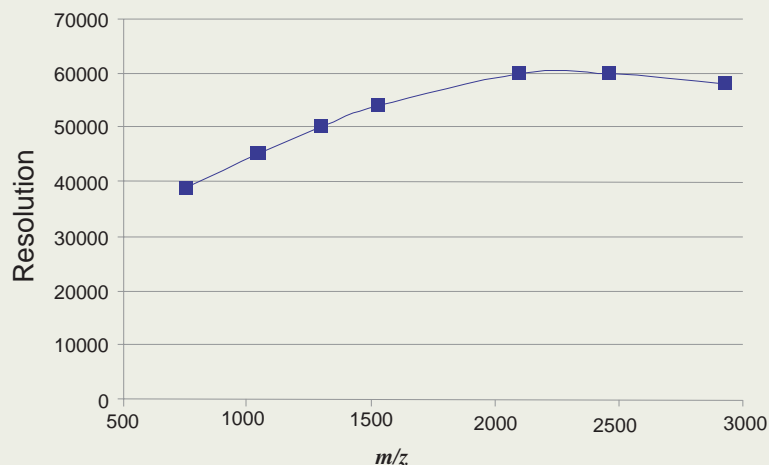


Fig. 4 Relation between m/z value and mass resolution.

a. Full product ion spectrum.

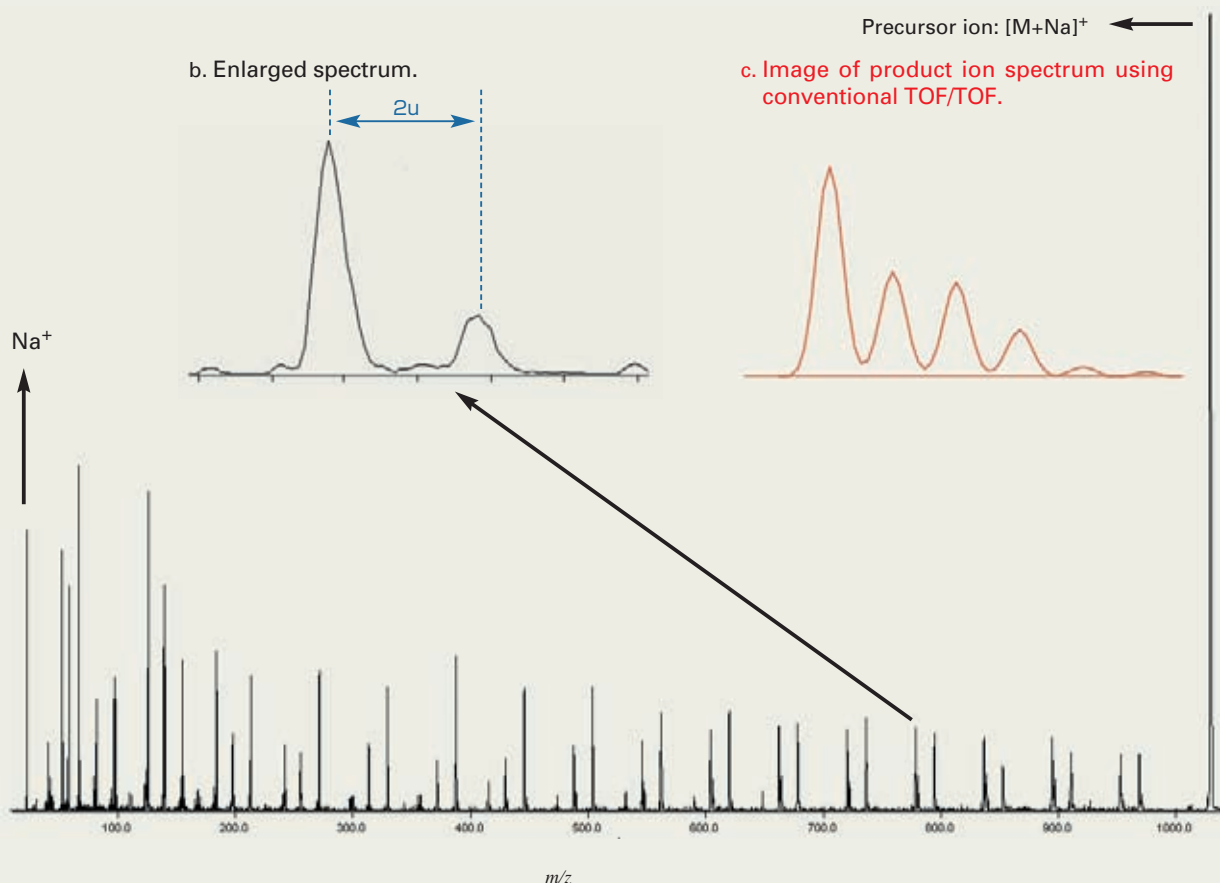


Fig. 5 Product ion spectrum of Poly(oxypropylene).

[5] H. Wollnik and A. Casares, *Int. J. Mass Spectrometry*, **227**, 217 (2003).
 [6] M. Toyoda, M. Ishihara, S. Yamaguchi, H. Ito, T. Matsuo, R. Reinhard and H. Rosenbauer, *J. Mass Spectrom.*, **35**, 163 (2000).
 [7] D. Okumura, M. Toyoda, M. Ishihara and I. Katakuse, *J. Mass Spectrom. Soc. Jpn.*, **51**, 349 (2003).

[8] M. Yavor, A. Verentchikov, J. Hasin, B. Kozlov, M. Gavrik and A. Trufanov, *Physics Procedia* 1 391 (2008)
 [9] T. Satoh, H. Tsuno, M. Iwanaga, Y. Kammei, *J. Am. Soc. Mass Spectrom.*, **16**, 1969 (2005).
 [10] T. Satoh, H. Tsuno, M. Iwanaga, and Y. Kammei, *J. Mass Spectrom. Soc. Jpn.*, **54**, 11 (2006).

[11] T. Satoh, T. Sato, and J. Tamura, *J. Am. Soc. Mass Spectrom.* **18**, 1318 (2007).
 [12] M. Ishihara, M. Toyoda and T. Matsuo, *Int. J. Mass Spectrom.*, **197**, 179 (2000).
 [13] E. N. Nikolaev, A. Somogyi, D. L. Smith, C. Gu, V. H. Wysocki, C. D. Martin and G. L. Samuelson, *Int. J. Mass Spectrom.*, **212**, 535 (2001)

Rapid Characterization of Bacteria Using ClairScope™ and SpiralTOF™

Kanae Teramoto

Advanced Technology Department, JEOL Ltd.

In many fields such as clinical diagnosis and food inspection, there is a demand for rapid, reliable and simple-to-use methods for characterizing bacteria. This paper explores the use of two new and innovative instruments called ClairScope™ and SpiralTOF™ for this rapid characterization. The JASM-6200 ClairScope™ integrates an optical microscope (OM) with a scanning electron microscope (SEM) where it is possible to observe samples in solution, in an open system, by the SEM at atmospheric pressure. This type of sample would typically require extensive sample pretreatment that would take a day or more with conventional SEM techniques. With the recently developed ClairScope™, fine morphological observation can be performed directly in solution with simple sample pretreatment of one hour or less. The JMS-S3000 SpiralTOF™, is a matrix-assisted laser desorption/ionization mass spectrometer (MALDI-MS) with a spiral ion trajectory. With sample pretreatment as fast as a few minutes, the SpiralTOF™ can characterize ribosomal proteins and phospholipids with high accuracy. Ribosomal proteins are biomarkers for phylogenetic classification, and phospholipids are used for chemotaxonomic analysis. The combination of ClairScope™ and SpiralTOF™ are found to be powerful instruments for the characterization of bacteria.

Introduction

Rapid characterization methods are in demand for bacteria, which are simple to use and reliable, in a variety of fields such as clinical diagnosis, food inspection, and in environmental energy industries. Bacterial characterization methods can be divided into two categories: analysis of phenotype and genotype. Phenotype analysis includes a morphological study and chemotaxonomy where analysis of bacterial cell components such as proteins and lipids are analyzed. Genotype analysis includes gel electrophoresis and DNA sequencing using a sequencer.

In many cases, a skilled operator can identify the species of bacteria using an optical microscope combined with supplemental information. However, optical microscope (OM) has limited resolution and with bacterial size typically smaller than a few micrometers, detailed structural information cannot be obtained. The use of scanning electron microscope (SEM) overcomes this resolution limitation but often requires long sample pretreatment such as dehydration and fixation that can take a day or even longer.

A chemotaxonomy, based on biochemical analysis, is effective in investigating characteristics of bacterial strains. Yet with current methodology, sample preparations are cumbersome. Also, these methods tend to be affected by differences in culture conditions, sample preparation techniques and measurement conditions which can lead to results that are not as reproducible as desired. The reduction in cost, improved throughput and larger databases are making DNA analysis methods more popular. However, in principle, errors in amplification and sequencing cannot be avoided. Therefore, using polyphasic methods to characterize bacteria is of prime importance.

In this paper, possibilities of new rapid characterization methods for bacteria were studied based on both phenotype and genotype. *Escherichia coli* NBRC 3301 was used as a model strain. The JASM-6200 ClairScope™ (atmospheric scanning electron microscope: ASEM) [1], was used to observe the morphology of the bacteria at atmospheric pressure. The JMS-S3000 SpiralTOF™, a matrix assisted laser desorption/ionization mass spectrometer (MALDI-MS) [2] with a spiral ion trajectory, was used to analyze the ribosomal proteins and phospholipids.

Morphological Observation of Bacteria with the JASM-6200 ClairScope™

The configuration of the JASM-6200 ClairScope™ is shown in **Fig. 1**. This microscope consists of an inverted SEM that incorporates a thin-film (silicon nitride, SiN)-windowed ASEM specimen dish on top. The film with a thickness of 100 nm allows transmission of the electron beam and also maintains a vacuum in the ASEM. These features enable SEM observation according to the following procedure: an ASEM specimen dish with the sample is placed on the ClairScope™, the sample is scanned with the electron beam from underneath through the thin SiN film, and then backscattered electrons emitted from the sample are detected. The ClairScope™ also includes a wide field OM just above the ASEM specimen dish for observation of the same field of view. This innovative microscope enables observation of samples such as bacteria, in solution at atmospheric pressure, using both optical and SEM imaging. Rapid and simple SEM observation can be achieved without the long dehydration and fixation

sample treatments typically required with conventional SEMs.

In this study, the *E. coli* NBRC 3301 was grown in Luria-Bertanimedium at 30°C for 8 h. The *E. coli* NBRC 3301 was harvested by centrifugation then washed twice with phosphate-buffered saline (PBS). They were re-suspended in the PBS and put on the ASEM specimen dish that was coated with poly-L-lysine. At this point, the sample was fixed with 2% paraformaldehyde/1% glutaraldehyde in PBS for 10 min. In addition, the sample was stained with 0.6% platinum blue [3] for 1 h. ASEM images of *E. coli* NBRC 3301 are shown in **Fig. 2**. Even with such a short sample pretreatment time, the ClairScope™ provided high resolution images where rod-shaped *E. coli* NBRC 3301 smaller than 2 μm were clearly visualized.

Although information obtained through imaging with the ClairScope™ can look different from that obtained by conventional SEM or transmission electron microscope, this new SEM not only allows for rapid observation but also enables much simpler and faster sample pretreatment prior to imaging for high throughput analyses. Also, with the recent advancement in fluorescent labeling, complimentary information can be obtained through the OM and correlating the information from both the OM and ASEM can play an important role in the characterization of bacteria.

Analysis of Ribosomal Proteins and Phospholipids with the JMS-S3000 SpiralTOF™

The JMS-S3000 SpiralTOF™ is shown in **Fig. 3** with its ion optical system. This instrument is an advanced MALDI TOFMS, for the analysis of a wide range of samples such as lipids, synthetic polymers, peptides, and pro-

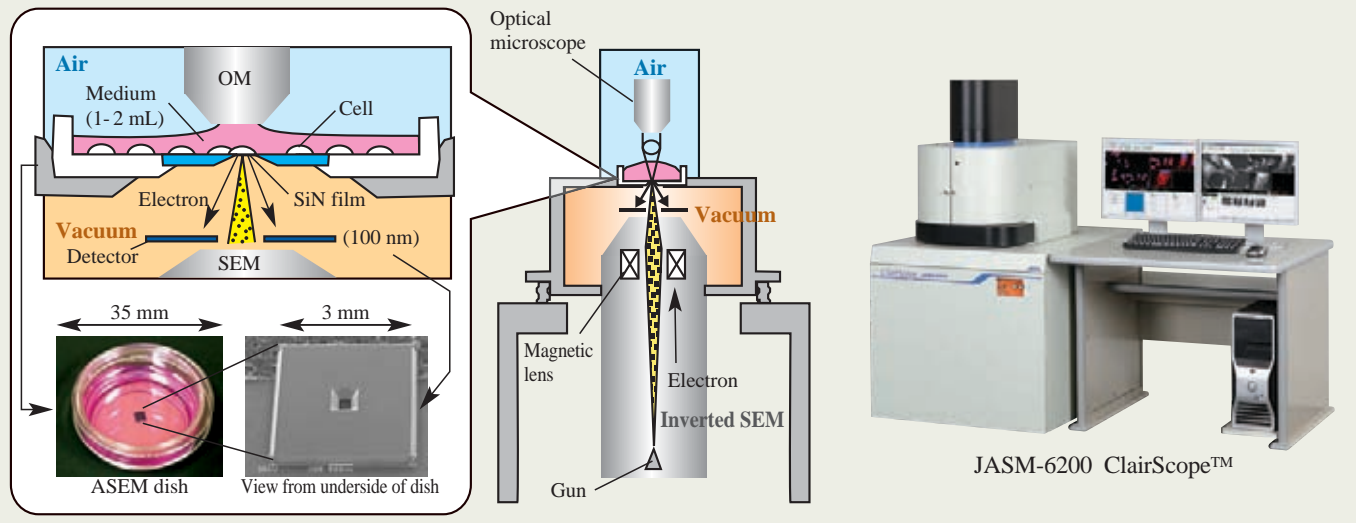


Fig. 1 The configuration of ClairScope™. Optical microscope (OM) is placed opposite to an inverted scanning electron microscope (SEM) (atmospheric scanning electron microscope: ASEM) and a film-windowed dish is placed between OM and ASEM.

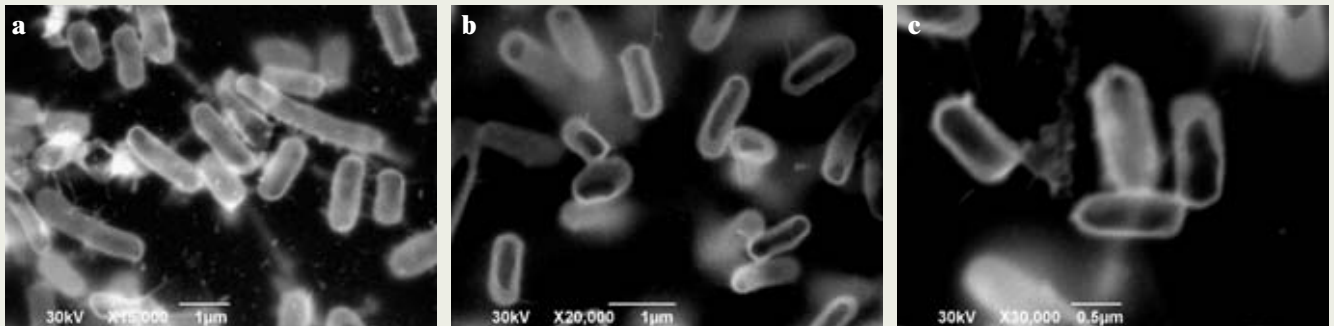


Fig. 2 ASEM images of *E. coli* NBRC 3301. $\times 15000$ (a), $\times 20000$ (b), and $\times 30000$ (c)

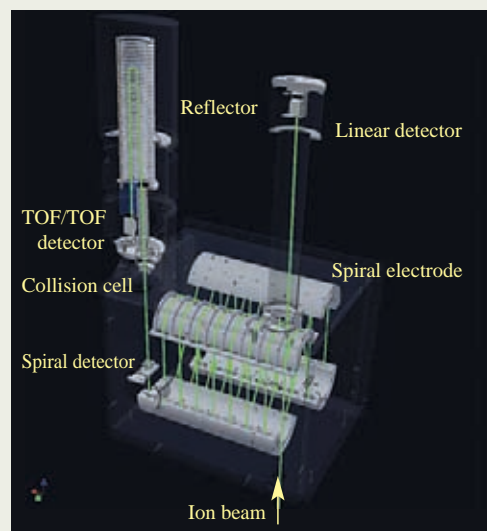


Fig. 3 The configuration of SpiralTOF™. Combined use of the spiral mode (flight length: 17 m) and the linear mode (flight length: 1.2 m) extends the application of this instrument to a wide range of fields. Spiral mode: Mass resolution $>60,000$, Mass accuracy <1 ppm.



JMS-S3000 SpiralTOF™

teins, through the combination of the spiral mode and the linear mode of operation. In particular, the spiral mode has an ion flight length of 17 m which is achieved by the ion optical system having a spiral trajectory. This suppresses beam broadening to prevent degradation of mass resolution and mass accuracy. Therefore, the SpiralTOF™ provides higher mass resolving power and higher mass accuracy than conventional MALDI TOFMS. This paper reports on the analysis of ribosomal proteins in the linear mode and the analysis of phospholipids in the spiral mode.

Analysis of ribosomal proteins with the SpiralTOF™ in linear mode

In recent years, mass spectral patterns obtained by MALDI-MS have been used for rapid identification and classification of bacteria. In this method, ribosomal proteins are observed and their spectra are compared with reference spectra from bacterial strains stored in a library database. This provides identification of bacteria at "species level" which can be

obtained by 16S rRNA gene sequencing [4].

On the other hand, the characteristics of bacteria such as antibacterial activity and toxicity are frequently different at the "strain level". To discriminate bacteria at the strain level, and to classify the bacteria based on genotype, we have used observed masses of ribosomal proteins as biomarkers instead of the mass spectral fingerprints [5-7]. Observed masses of ribosomal proteins in MALDI mass spectra have been precisely assigned with calculated mass from DNA sequence. We have shown that it is possible to discriminate bacteria at

the strain level, using the number of identical peaks. Based on our method, the classification results were comparable to phylogenetic classification based on DNA gyrase subunit B gene sequencing [5, 6].

Sample preparation and data analysis of ribosomal proteins were carried out according to a previous paper [8]. Briefly, the cells were mixed directly with a matrix solution containing sinapinic acid in an organic solvent. Since *E. coli* NBRC 3301 is a gram-negative strain, cell walls are lysed by mixing with this matrix solution. About 1 μL of sample/matrix mixture was spotted on the MALDI target plate. The MALDI-MS measurements were performed using SpiralTOF™ in the linear mode. Fig. 4 shows MALDI mass spectrum for *E. coli* NBRC 3301. In this spectrum, each peak was clearly separated with high intensity, and these observed peaks were assigned as phosphatidylethanolamine (PE) within 0.001 Da (ca. 1 ppm) error. These PEs contain unsaturated double bonds and have carbon numbers from 29 to 36 (Fig. 6). The results were found to be almost the same as those reported by Ishida *et al.* [9]. In this simplified sample pretreatment, separation techniques for samples are not used. This tends to give complex mass spectra consisting of many peaks from different components. Use of a mass spectrometer with insufficient mass resolving power and mass accuracy makes it impossible to separate adjacent peaks and can lead to

errors in assigning peaks and with the final result. On the other hand, the SpiralTOF™, which has high mass resolving power and high mass accuracy, provides a clear separation of adjacent peaks. This yields reliable results, even with automatic assignment of peaks using software from complex mass spectral data. The SpiralTOF™ is expected to play a significant role in analyzing practical samples comprised of many components, since it provides accurate results with simple sample pretreatment methods and data analysis.

Conclusion

There is no complete single method which can fully cover the characterization of bacteria. With this in mind, there is a demand for the development of simple, rapid and reliable methods. In this paper, *Escherichia coli* NBRC 3301 was characterized based on phenotype and genotype using the ClairScope™ and the SpiralTOF™. The ClairScope™ pro-

Compositional analysis of phospholipids with the SpiralTOF™ in spiral mode

The cell components of bacteria are much more diverse than those of eukaryote. Thus, analyzing the components such as lipids, peptidoglycans, and proteins is effective for bacterial characterization at the strain level. This is known as chemotaxonomy. Lipids including fatty acids, phospholipids, sphingolipids, mycolic acids and the isoprenoid quinone group are often studied. In particular, glycerophospholipids are included in all bacterial cells so that analyzing them is valuable. The compositional distribution of hydrocarbon chains, especially carbon numbers and degree of double bonds, as well as the chemical structures of hydrophilic groups are important biomarkers for chemotaxonomy of bacteria.

Ishida *et al.* proposed the on-probe method where whole bacterial cells are deposited directly on to a MALDI target plate, and intact phospholipids from the cells are analyzed by MALDI-MS [9]. This simplified sample pretreatment significantly reduces sample preparation time to several minutes. Since bacteria normally contain several types of phospholipids with different chemical structures, mass spectra peaks for phospholipids frequently show overlaps that are not easily resolved. It is crucial to separate and identify these peaks clearly and precisely for accurate characterization of bacteria. For this purpose, the SpiralTOF™ is especially valuable, since it has high mass resolving

power and high mass accuracy (at $m/z \sim 1,000$, peak of $\Delta M < 0.04$ Da can be separated).

The sample preparation for phospholipids from whole bacterial cells were carried out according to the method established by Ishida *et al.* [9]. Polymerix (Sierra Analytics Corporation) was used for data analysis.

Fig. 5 shows a MALDI mass spectrum of phospholipids extracted from the whole cells of *E. coli* NBRC 3301. Most of the peaks observed in the mass spectrum were assigned as phosphatidylethanolamine (PE) within 0.001 Da (ca. 1 ppm) error. These PEs contain unsaturated double bonds and have carbon numbers from 29 to 36 (Fig. 6). The results were found to be almost the same as those reported by Ishida *et al.* [9]. In this simplified sample pretreatment, separation techniques for samples are not used. This tends to give complex mass spectra consisting of many peaks from different components. Use of a mass spectrometer with insufficient mass resolving power and mass accuracy makes it impossible to separate adjacent peaks and can lead to

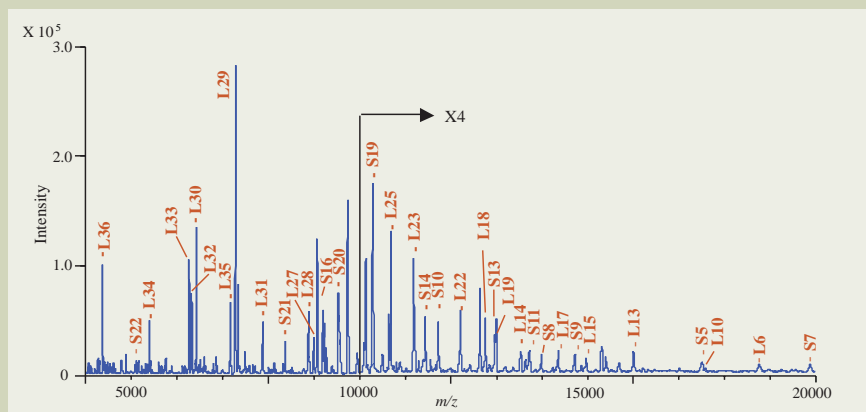


Fig. 4 MALDI mass spectrum of *E. coli* NBRC 3301 (linear mode).

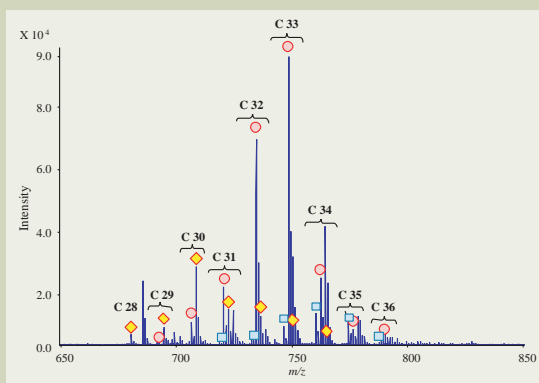


Fig. 5 MALDI mass spectrum of phospholipids extracted from whole cells of *E. coli* NBRC 3301 (spiral mode).
 ◆ PE (saturated), ○ PE (monoene), and □ PE (diene).

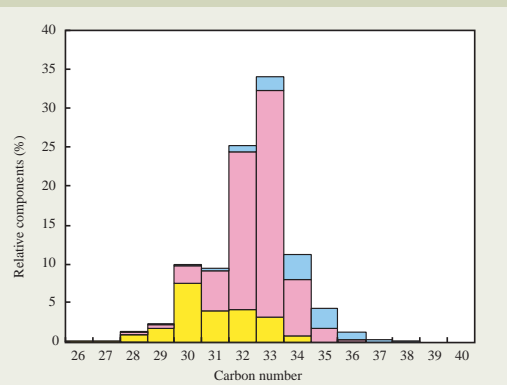


Fig. 6 Composition of PE extracted from whole cells of *E. coli* NBRC 3301.
 ■ PE (saturated), ■ PE (monoene), and ■ PE (diene).

vided morphological observation with simple sample pretreatment methods requiring only one-hour (fixation and staining), versus the treatment methods required with conventional SEM which can take up to ten times longer. The advantage here is rapid morphological observation at high magnifications with very simple and fast sample pretreatment. The ClairScope™ is expected to be especially valuable for slow-growing bacteria including pathogenic ones, since it also requires a small amount of sample.

In addition, the SpiralTOF™ enabled highly reliable analyses of bacteria with pretreatment times that take only a few minutes. The linear mode was used for the analysis of ribosomal proteins. These proteins act as biomarkers for phylogenetic classification of bacteria at the strain level. The spiral mode was used for the analysis of phospholipids, which are biomarkers for chemotaxonomy.

In many cases, the reliability of analyses that use rapid and simple methods is not high.

However, the use of these two new and innovative instruments are not only simple to use, but also provides fast and highly reliable results.

The new methods described in this paper are well suited for high throughput characterization of bacterial samples. First, morphological observation with the ClairScope™ can provide insight such as whether a sample contains bacteria or sometimes whether they are pathogenic combined with some other information. Second, using the SpiralTOF™ in linear mode, ribosomal proteins which are used as biomarkers to distinguish and classify the bacterial samples at the strain level, can be analyzed. This also determines appropriate pre-treatment for chemotaxonomy of relevant strains. Third, components of bacterial cells such as phospholipids and mycolic acids, can be analyzed using the SpiralTOF™ in spiral mode. The combination of these methods will give a broad range of information (Fig. 7) and can provide complementary information for other methods such as

sequence analysis of 16S rRNA gene.

References

- [1] H. Nishiyama *et al.*, *J. Struct. Biol.* **169**, 438-449 (2010).
- [2] T. Satoh *et al.*, *J. Am. Soc. Mass Spectrom.* **18**, 1318-1323 (2007).
- [3] S. Inaga *et al.*, *Arch. Histol. Cytol.* **70**, 43-49 (2007).
- [4] A. Mellmann *et al.*, *J. Clin. Microbiol.*, **46**, 1946-1954 (2008).
- [5] K. Teramoto *et al.*, *Anal. Chem.*, **79**, 8712-8719 (2007).
- [6] K. Teramoto *et al.*, *J. Biosci. Bioeng.*, **108**, 348-353 (2009).
- [7] L. Sun *et al.* *Rapid Commun. Mass spectrom.* **20**, 3789-3798 (2006).
- [8] K. Teramoto *et al.*, *J. Proteome Res.*, **6**, 3899-3907 (2007).
- [9] Y. Ishida *et al.*, *Rapid Commun. Mass spectrom.* **16**, 1877-1882 (2002).

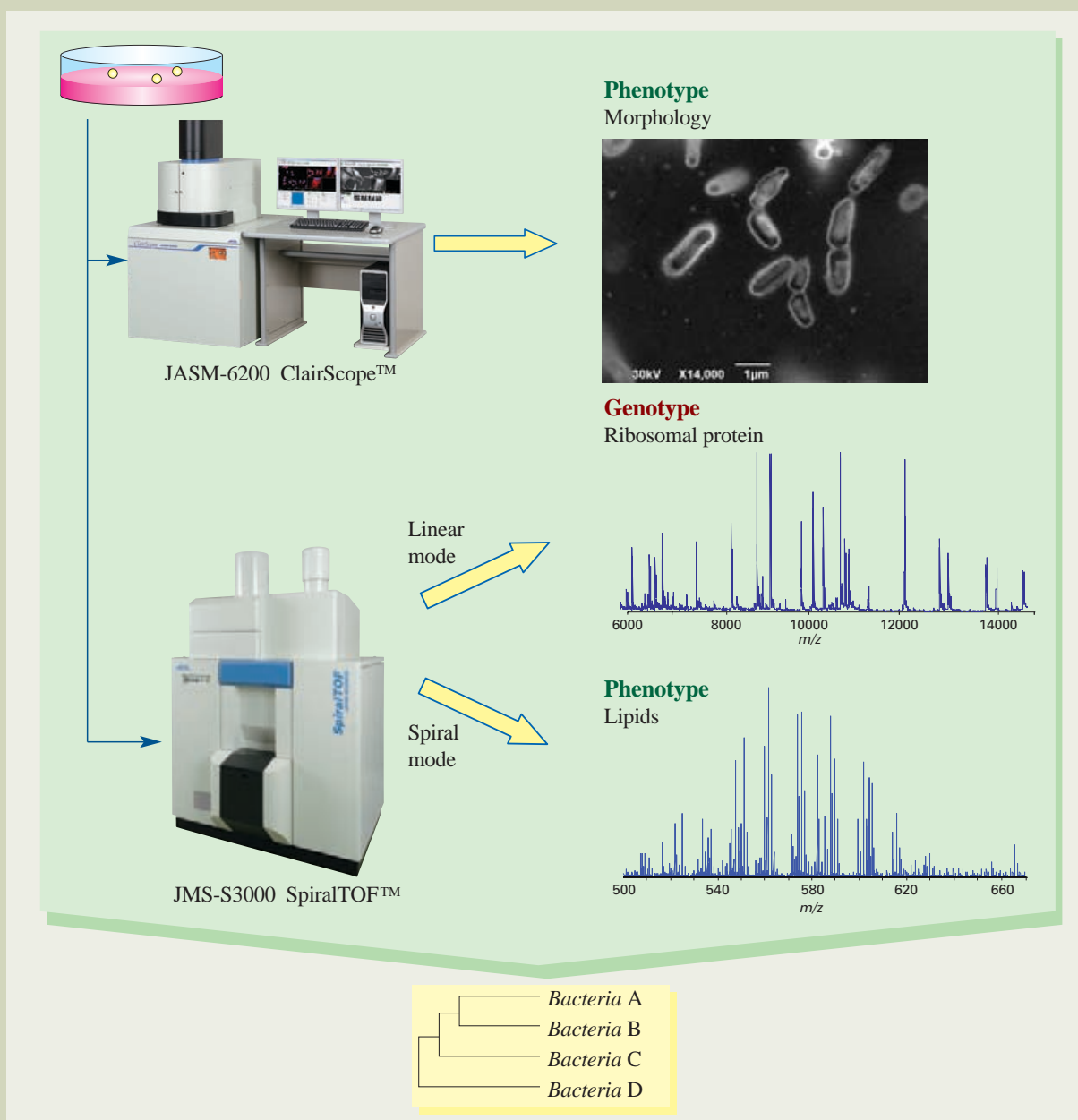


Fig. 7 Conceptual image of rapid characterization of bacteria using both ClairScope™ and SpiralTOF™.

Micro Area Analysis with JXA-8530F (FE-EPMA)

Norihisa Mori

SA Business Unit, JEOL Ltd.

The FE-EPMA, an electron probe micro analyzer (EPMA) equipped with a Schottky field emission (FE) electron gun, is designed to enhance the micro area analysis capability, achieving an analytical area of only $0.1 \mu\text{m}$ in size. Micro area analyses were studied on stainless steel and solder samples with a FE-EPMA to evaluate its spatial resolution, micro particle detection, and ability to quantify micro areas.

Introduction

FE-EPMA, an electron probe micro analyzer (EPMA) equipped with a Schottky field emission (FE) electron gun, is designed to enhance the microarea analysis capability [1], achieving an analytical area of the order of $0.1 \mu\text{m}$ across in size.

Typically the analytical area of EPMA has been about $1 \mu\text{m}$ in both width and depth. The size of an analytical area is determined by the size of the electron probe at the surface and the spread of scattered electrons within the sample. At an accelerating voltage in the range of 15 to 20 kV, the range used most frequently in EPMA, the analytical area is principally determined by the area of electron scattering within the sample, which is typically around $1 \mu\text{m}$ in diameter.

At lower accelerating voltages, the analytical area is reduced because the electron scattering within the sample becomes smaller. However, it is also critical not to decrease the accelerating voltage during high spatial resolution analyses because the size of the electron probe becomes larger at lower accelerating voltages. In EPMA with a tungsten filament, the horizontal spatial resolution does not improve significantly when the accelerating voltage is lowered to 15 kV or less. The use of a LaB_6 gun, with its ability to achieve a finer probe size, is effective for improving the horizontal spatial resolution, but only at accelerating voltages down to 10 kV. [2]

The EPMA can analyze almost all elements at accelerating voltages down to 6 kV, when the characteristic X-ray excitation voltage of all the X-ray lines are considered. Therefore, an EPMA with an FE gun, capable of achiev-

ing the finer probe at lower accelerating voltages and high probe currents needed for analysis, can improve the micro area analysis capability over the traditional EPMA with a tungsten or LaB_6 gun.

We have studied micro area analyses of stainless steel and solder samples with FE-EPMA to evaluate its performance in terms of spatial resolution, micro particle detection, and quantification of micro areas.

FE-EPMA(JXA-8530F)

JXA-8530F (Fig.1) is equipped with a high

brightness Schottky field emission (FE) gun allowing an electron probe to focus on smaller areas than the conventional EPMA. The FE gun achieves a probe size 1/2 to 1/8 smaller when compared to the tungsten or LaB_6 gun. Alternatively, the FE gun can produce a probe current 20 to 100 times higher than the tungsten or LaB_6 gun with the same probe size (Fig.2).

An EPMA is commonly used with a probe current of 10 nA to 100 nA. We therefore compared the images of gold particles acquired with FE, LaB_6 , and tungsten guns at an accelerating voltage of 10 kV and a probe current of 100 nA (Fig. 3). The results show



Fig. 1 JXA-8530F, EPMA with FE gun.

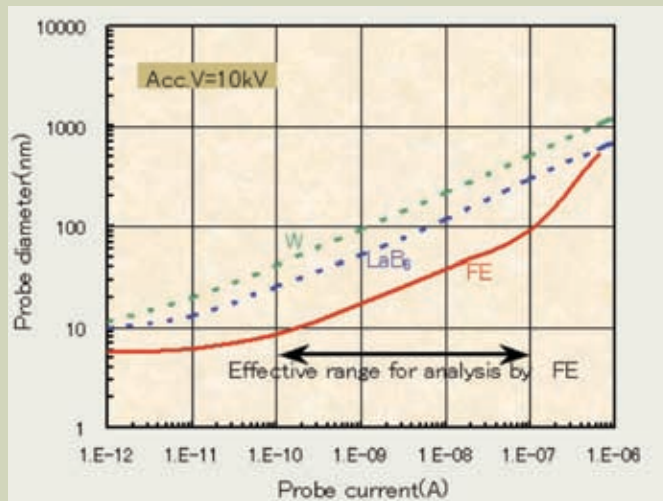


Fig. 2 Probe sizes achieved by JXA-8230 (W, LaB₆ guns) and JXA-8530F (FE gun).

that the FE gun, under conditions frequently used in actual analysis, is definitely superior to the LaB₆ or tungsten gun in terms of spatial resolution.

In addition to the electron gun, the JXA-8530F integrates various features that support high magnification analysis. It uses a two-stage differential pumping system to maintain the vacuum in the electron optics at an optimum level. This prevents changes in the vacuum in the specimen chamber from affecting the gun chamber, thereby achieving probe current stability needed for EPMA analysis. An optional liquid nitrogen trap, sustainable for 10 hours or longer, minimizes the re-absorption of residual gases in the specimen chamber or gases emitted from the sample, allowing samples that are susceptible to gas absorption to be analyzed overnight. Analyzing crystals for low energy X-ray analysis, such as the LDE series and TAPH, are also effective for enhancing the performance at low accelerating voltages.

Spatial resolution of X-ray mapping

To obtain X-ray maps with the highest spatial resolution, the probe size must be the smallest, and the accelerating voltage the lowest. If the accelerating voltage is higher, the area from which X-rays are generated becomes larger due to the electron scattering within the sample, thereby reducing the spatial resolution.

The W type EPMA needs to use a higher accelerating voltage (15 to 20 kV) to obtain the probe current needed for typical analysis, because it cannot achieve a small enough probe size at a lower accelerating voltage. The FE gun, however, can produce a probe size small enough for analysis at 10 kV or lower, achieving much higher spatial resolution.

A lead-free solder sample was analyzed at the same accelerating voltage (8 kV) with three different electron guns (Fig. 4). This

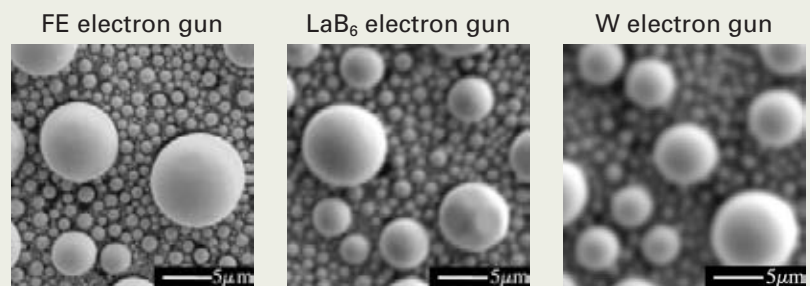


Fig. 3 Gold particles photographed with FE, LaB₆, and tungsten guns. Conditions: Accelerating voltage 10 kV; probe current 100 nA.

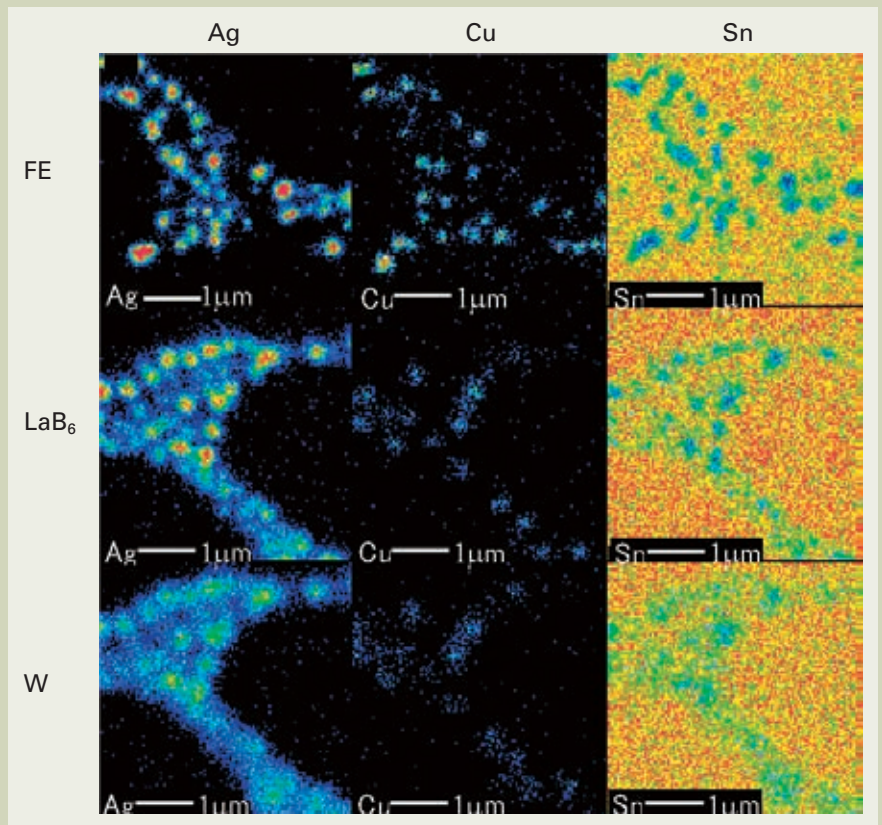


Fig. 4 X-ray images of Ag, Cu, and Sn in lead-free solder. Conditions: Accelerating voltage 8 kV; probe current 10 nA. The FE gun produced X-ray images with the highest spatial resolution. See attached color images.

lead-free solder contains numerous particles, that 1 μm or smaller in size, of either an Ag alloy or a Cu alloy distributed in the Sn matrix. The FE gun, with the smaller probe size, acquired the best X-ray maps with superior spatial resolution.

The spatial resolution of X-ray mapping of a bulk sample is considered to be around 0.1 μm when the FE gun is used at an accelerating voltage optimized for the probe size and the electron scattering within the sample. The appropriate accelerating voltage for the FE gun varies with different samples, but it ranging from 3 to 6 kV. The accelerating voltage should be lower for samples with a smaller mean atomic number, such as oxides. However, for samples with mean atomic number higher than Fe, the accelerating voltage should be set to 5 kV or 6 kV for optimum results.

Thus, the JXA-8530F, with its FE gun, can achieved a spatial resolution of around 0.1 μm by using a low accelerating voltage.

Detecting trace elements and micro particles

The results in the preceding section demonstrate that the JXA-8530F has a spatial resolution significantly better than the conventional EPMA. However, for elemental analyses, other systems are also widely used; those with similar capabilities to the EPMA (JXA-8230/8530F) include the FE-SEM+EDS (JSM-7001F), and those with higher spatial resolution include the AES (JAMP-9500F) and the TEM. The major difference between the EPMA and these other systems is that the EPMA uses wavelength dispersive X-ray spectrometer (WDS) for the elemental analysis. We will focus on two features below that sets WDS apart from the other techniques:

- 1) Superior detection of trace elements
- 2) Accurate quantitative analysis

Item (1) is related to the ability to detect micro particles, which is one of the critical factors in high-resolution analysis. Item (2) will be discussed in the next section.

Figure 5 is a backscattered electron image of stainless steel sample that contains Nb and C. Bright particles and extremely small particles with the size of 0.1 μm or less, are observed in the matrix. Nb and C maps of the stainless steel sample were collected by both WDS and EDS. **Figure 6** shows the results.

The remarkable difference between the WDS and EDS data can be seen in the distribution of particles in the carbon X-ray image. The WDS carbon X-ray image shows numerous small particles, whereas the EDS X-ray image hardly shows any of these particles. This demonstrates the difference in trace element detection between the WDS and the EDS capability.

Figure 7 illustrates how particles that are smaller than the analytical area of the EPMA are detected. Electron beam will scatter once they enter the sample. When the probe is placed onto a particle smaller than the analytical area, the beam will spread beyond the particle boundary. Since the particle size is smaller than the volume of the area being measured, the intensity of the measured X-rays will be lower.

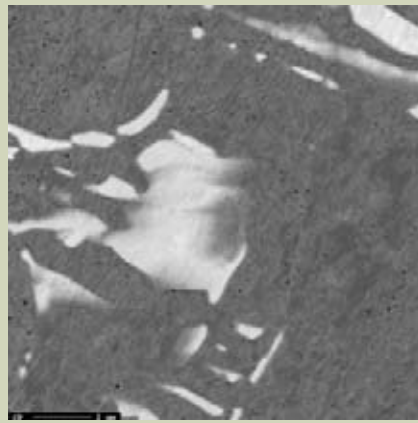


Fig. 5 BE composition image of stainless steel. Numerous black particles 0.1 μm or less present in matrix.

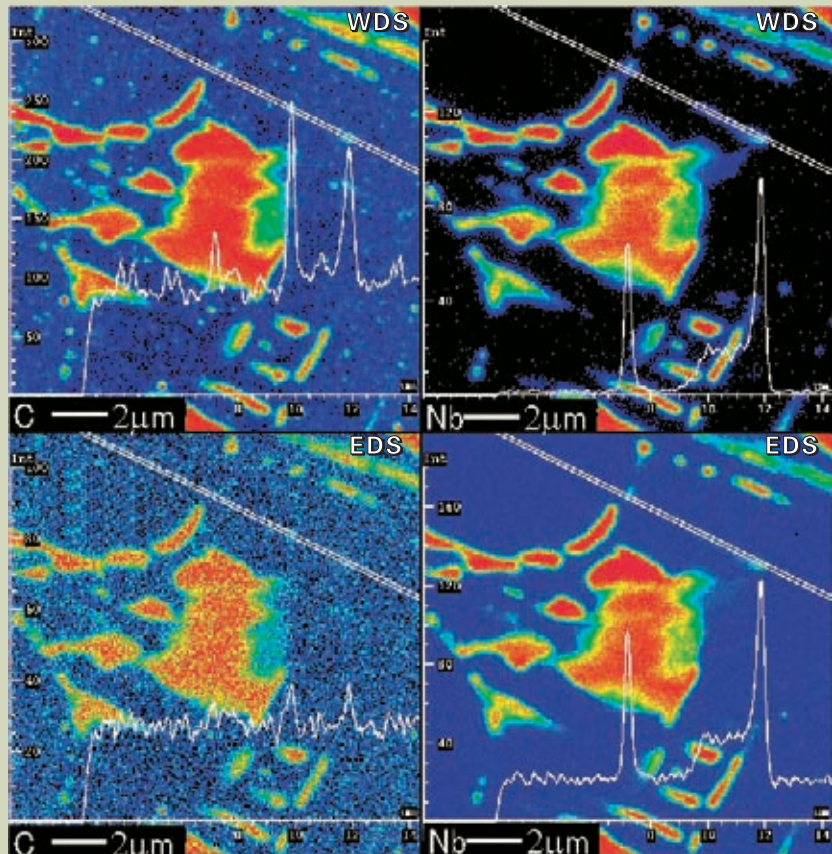


Fig. 6 WDS and EDS analysis of the area of view in Figure 5.

Line profile of straight line in each map.

Conditions: Accelerating voltage 7 kV; probe current 50 nA.

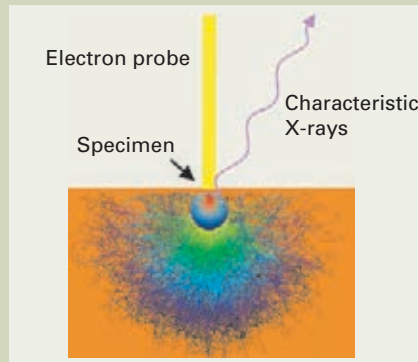


Fig. 7 The X-ray intensity is very low for particles 0.1 μm or smaller, due to the small volume from which these X-rays are being emitted.

	WDS	EDS
C	0.5%	2.7%
Nb	0.3%	1.0%

Fig. 8 Detection limits under mapping conditions used in Figure 6.

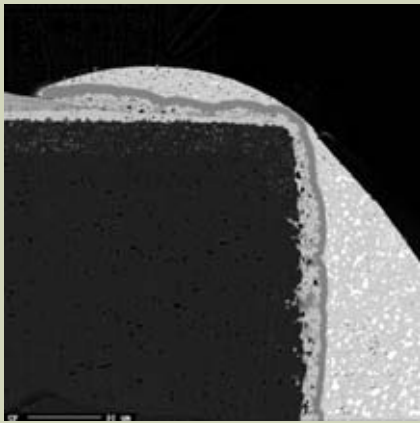


Fig. 9 BE composition image of chip resistor mounted to substrate (cross section).

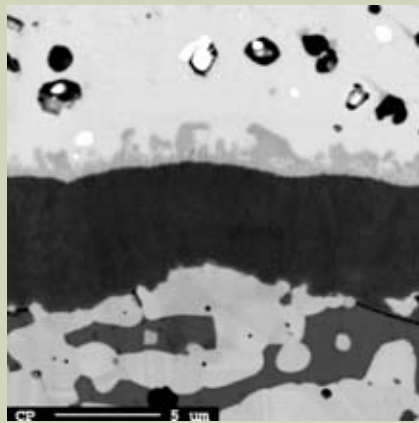


Fig. 10 Magnified image of Figure 9. Alloy layer present at the interface of Ni plating is at center and solder at top.

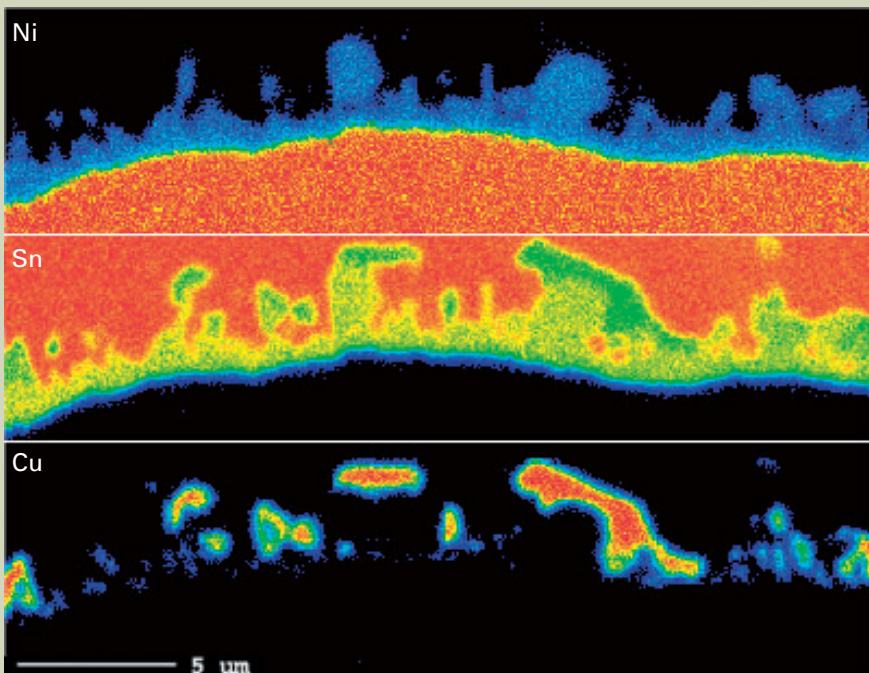


Fig. 11 X-ray image of the interface in Figure 10. Shown are NiSn and CuSn alloys distributed along the interface between Ni plating and solder. Conditions: Accelerating voltage 6 kV; probe current 10 nA.

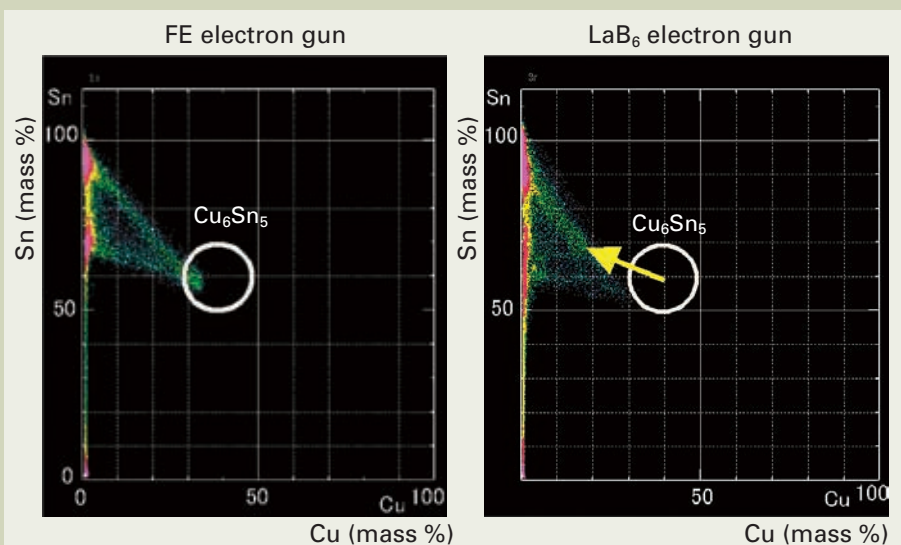


Fig. 12 Phase analysis of the area shown in Figure 11, comparing data acquired by FE and LaB₆ guns

This low X-ray intensity determines whether the trace elements are detectable. Therefore a system effective for analyzing trace elements is also best for analyzing micro particles. This applies to thin film analysis as well.

The detection limit of WDS or EDS is defined as follows:[3]

$$C_{DL} = \frac{3.29a}{\sqrt{\left(ntP \frac{P}{B}\right)}}$$

C_{DL} : Detection limit (mass %)
 a : Correction coefficient (ZAF etc.)
 n : Number of analytical spots
 t : Measurement time (s)
 P : Peak intensity of standard sample
 P/B : P/B ratio of standard sample

The table (Fig.8) shows the results when the parameters for C and Nb are substituted in the formula above. The correction coefficient was assumed to be 1 for this example.

As the table shows, the ability of WDS to detect trace elements in mapping is higher than that for EDS. Thus, WDS is more effective in detecting micro particles than EDS.

AES and TEM systems have higher spatial resolution, but the location of particles is critical; particles must be either on the surface (AES) or inside a thin film (TEM). EPMA, on the other hand, can analyze particles containing trace elements that extend from the surface to a 0.1 to 1 μm depth within the sample by changing the accelerating voltage. The EPMA, with its wider range of analytical depths, is often better at detecting micro particles that exist within a sample than AES or TEM. Other examples of EPMA applications include studies of the distribution of Au scattered as micro particles in solder, and the detection of trace components, on the order of ppm, as impurities in stainless steels.

When WDS, effective for trace element detection as well as micro particle analysis, is combined with an FE gun, the result is a powerful analytical tool.

Spatial resolution in quantitative analysis

One advantage of WDS is its highly accurate quantitative analysis. A solder interface was selected as a test to determine the minimum size area capable of being quantitatively analyzed using WDS.

Figure 9 is a cross section of a chip resistor mounted to substrate. The interface between the Ni and the solder shown in the cross section was mapped. Results of this area analysis (Fig. 11) show that an Ni-Sn alloy layer occurs next to the Ni, Sn layer of solder is then in contact with the Ni-Sn alloy layer, and a Cu-Sn alloy layer occurs discontinuously between the Ni-Sn alloy and Sn layers. The Cu-Sn alloy layer is Cu₆Sn₅ which is a result of a Cu coating on the Ni surface that alloyed with the Sn.

Phase analysis was applied to the Cu₆Sn₅ alloy (Figure 12). The data from the area analysis were quantified and plotted, with the Sn mass concentration in the vertical axis and the Cu mass concentration in the horizontal axis.

When particles 0.2 μm in size are analyzed

at an accelerating voltage of 6 kV, approximately 10% of the X-rays will be emitted from outside of the particles, assuming a focused beam. Therefore, a circle with a radius of 10% was drawn at a point corresponding to the mass concentration of Cu_6Sn_5 on the scattered diagram, and it was assumed that the area within the circle was where the quantitative analysis was performed.

In the data obtained with the FE gun, numerous points occur within the area of the circle. Data obtained with the LaB_6 gun, shows very few points within the circle corresponding to Cu_6Sn_5 , since higher Sn concentrations and lower Cu concentrations were measured due to the larger probe size that interacted with the Sn in the vicinity.

Phase analysis was carried out on another region to examine the Cu-Sn alloy distributed in layers at the interface between the solder and Cu (Figs. 13 and 14). The results show that in this sample, the thickness of the Cu_6Sn_5 alloy layer exceeds 1 μm . The data also shows another layer, 0.2 μm thick, at the interface between Cu and Cu_6Sn_5 . This layer is a Cu_3Sn_1 alloy.

As before, a circle with a radius of 10% was drawn at each of the points corresponding to the mass concentrations of Cu_6Sn_5 and Cu_3Sn_1 on the scattered diagram. There is little difference between the in the distribution of Cu_6Sn_5 data taken with the FE gun and the LaB_6 gun. However, for the 0.2 μm thick layer of Cu_3Sn_1 there are numerous points that plot within the circle in the FE gun data, while no apparent correlation was detected within the data from the LaB_6 gun. This demonstrates that the JXA-8530F can quantitatively analyze a layer only 0.2 μm thick. This is an area that is twice the size of the spatial resolution of X-ray imaging, which is 0.1 μm .

The X-ray emitting area spreads from the probe center. It is safe to assume that the area where 50% of the X-rays are emitted determines the spatial resolution. This has been verified by Monte Carlo simulation and actual measurements [2, 4].

For quantitative analysis where a 10% error is permitted, 90% of the X-rays emitted must come from the specific area being analyzed. The area where 90% of X-rays are emitted will be approximately twice the size of the area where 50% of X-rays are emitted. An area 3 times larger will include most of the X-rays that are emitted and will insure even more accurate quantitative results.

To summarize, the analysis of the solder interface by the JXA-8530F, demonstrates that the spatial resolution of X-ray imaging is about 0.1 μm , whereas for point analysis an area of 0.2 μm is required, if a 10% contribution from the matrix is acceptable, and 0.3 μm is required for high precision quantitative analysis.

Conclusion

The JXA-8530F with an FE gun was used for micro area analysis of stainless steel and solder samples to evaluate its spatial performance. The results of the bulk sample analyses at low accelerating voltage shows that the JXA-8530F is capable of:

- 1) Achieving a spatial resolution of 0.1 μm for X-ray imaging at low accelerating voltages;

- 2) Detecting micro particles even smaller than the defined spatial resolution using WDS effective for trace element detection;
- 3) Quantitative analysis of an area only 0.2 μm in size, subject to a 10% interference from the matrix; a higher accuracy is achieved with an area 0.3 μm in size.

References

- [1] H. Yamada, T. Okumura, T. Kimura, W.

Knoll, *Proc. of ICEM 15th DURBAN*, 343, (2002)

- [2] N. Mori, *Proc. of The 19th International Congress on X-Ray Optics and Microanalysis (Kyoto, 2007)*, p34

- [3] Joseph I. Goldstein, et. al *Scanning Electron Microscopy and Xray Microanalysis*, p 500, (1994)

- [4] Ian Barkshire, Peter Karduck, Werner P. Rehbach, *Silvia Richter Mikrochim. Acta*, **132**, 113, (2000)

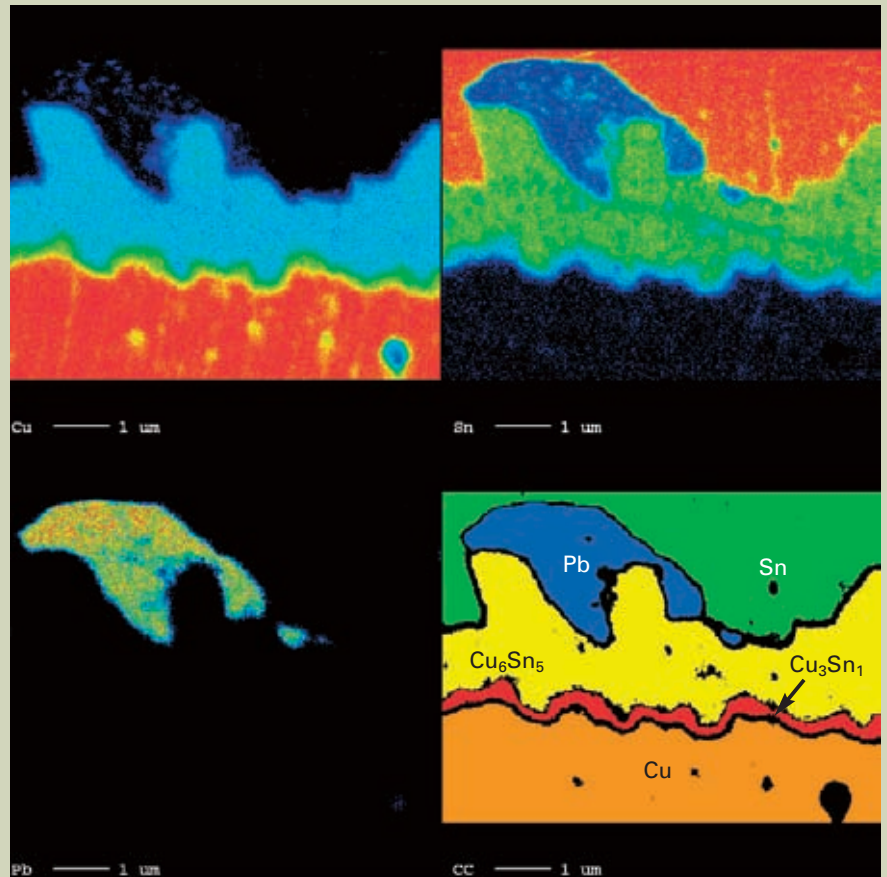


Fig. 13 X-ray image of the interface between solder and Cu. Cu_6Sn_5 and Cu_3Sn_1 alloys occur between the Sn and Cu. The image shows a Cu_3Sn_1 alloy layer 0.2 μm thick. See attached color images.

Conditions: Accelerating voltage 6 kV; probe current 10 nA.

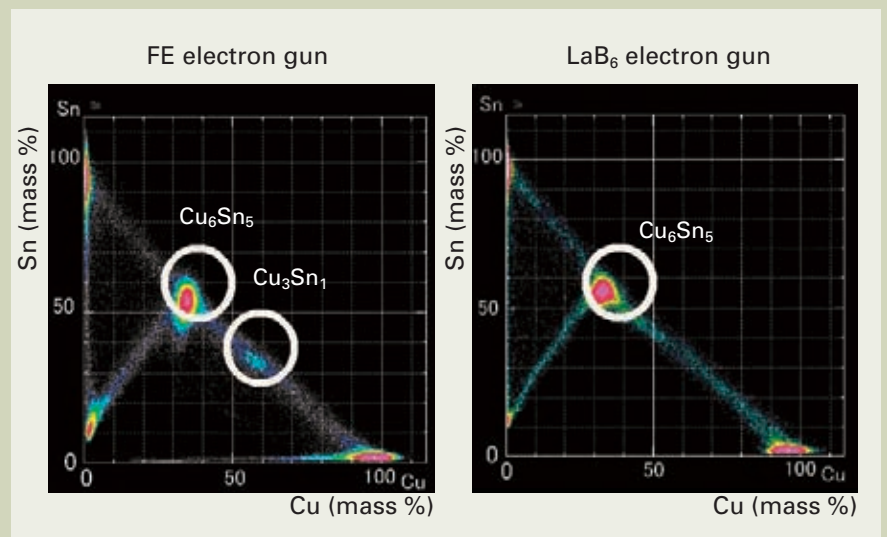


Fig. 14 Phase analysis of Cu-solder interface by FE and LaB_6 guns. The FE gun was able to detect the presence of a Cu_3Sn_1 alloy layer. See attached color images.

Analysis of Insulator Samples with AES

Kenichi Tsutsumi, Nobuyuki Ikeo, Akihiro Tanaka, and Toyohiko Tazawa

SA Business Unit, JEOL Ltd.

Introduction

Auger Electron Spectroscopy (AES) makes it possible to analyze a sample at an extremely shallow region such as about 6 nm from the top surface of the sample, enabling you to analyze elements present in a minute area such as 10^2 nm^2 on the surface if you use the focused electron beam as a probe. However, this attractive feature is limited only to the analysis of conductor and semiconductor samples; on the other hand, for the analysis of insulator samples, it becomes difficult even to observe the secondary electron image of the sample due to charging phenomenon.

However, it does not necessarily mean that you cannot perform the Auger analysis for the insulator sample. Actually, if you have some knowledge and experience, you can perform the Auger analysis even on the insulator sample while suppressing charging by using the sample tilt method; and you can also perform the Auger analysis by taking the advantage of high spatial resolution of $1 \mu\text{m}$ diameter or less depending on the state of the insulator sample. In particular, after introducing the "Ar neutralizer gun" that can irradiate low speed Ar ions about 10 to 30 eV to suppress charging, the charge on the sample surface can be controlled relatively easily, making it possible to greatly expand the applicability of the AES analysis to the insulator samples.

This article presents a guiding principle of the way of thinking for the insulator analysis and summarizes the strategy from the basic principle so that the insulator analysis using the AES can be performed without any sophisticated skill.

Basic Principle for Analyzing the Insulator Sample

Kinetic energy of Auger electron and surface potential

Because the kinetic energy (K) of an Auger electron can be uniquely determined by the type of an element and its transition process, the element can be identified from the energy (Fig. 1). The kinetic energy becomes the value reflecting the difference between the binding energies of the electron shells involved in the Auger transition, so in the case of the $KL_1L_{2,3}$ transition process shown in Fig. 1, the kinetic energy can be expressed as in Eq. (1).

$$K_{KL_1L_{2,3}} = (E_K - E_{L_1}) - E_{L_{2,3}} - \phi \cdots \cdots (1)$$

where, E_x is the binding energy of an electron shell and ϕ is the work function.

This Eq. (1) is used to obtain the kinetic energy of the Auger electron and it is presupposed that the sample surface is kept at the earth electric potential. However, in the case of the insulator sample, because the surface is not kept at the earth electric potential but in an electrically isolated state, the electrostatic energy of the actually measured electron is detected at the value with the surface potential V_S added to the kinetic energy of the Auger electron. Therefore, when you obtain the electrostatic energy U of the electron by taking the surface potential into consideration, it becomes as Eq. (2).

$$U = K - V_{S(x, y, t)} \cdots \cdots (2)$$

where, U is the electrostatic energy of the observed electron, K is the kinetic energy of the Auger electron, and $V_{S(x, y, t)}$ is the surface potential, which is the function of the position (x, y) of the sample surface and the time t , and has a negative sign because the electron has the negative charge.

The energy of the electron measured using the Auger Electron Spectroscopy represents this electrostatic energy U . In the case of the conductor sample, because the surface potential becomes always $V_S = 0$ regardless of the sample position, the equality $U = K$ holds, the measured electrostatic energy corresponds directly to the kinetic energy of the Auger electron. On the other hand, in the case of the

insulator sample, because the sample surface is in an electrically isolated state, even if the analysis position is fixed in place, because the magnitude of the surface potential changes depending on the amount of the incident electrons and the diffusion speed of the charged electrons, the electrostatic energy of the observed electron does not become stable. This is a fatal problem in the Auger analysis. If the shift of the peak position changes by the fluctuation of the surface potential V_S due to the effect of charging in a sufficiently short time compared with the measurement time of the spectrum, it disturbs the accurate spectrum measurement. For example, the peaks become broader as in the superimposed spectrum shown in the right figure in Fig. 2 or a ghost peak appears. In order to perform Auger analysis with high accuracy, you need to search a condition to become $V_S = (\text{constant})$ regardless of the measurement time even if the surface potential V_S does not become zero.

A problem of charging when the electron beam enters the sample surface

This section describes the charging phenomenon when the electron beam enters into the sample. Fig. 3 shows an optical and a secondary electron image of a general printed circuit board on which Au electrodes are wired. In the secondary electron image, the glass epoxy resin portion exhibits a typical secondary electron image of charged material, revealing that the contrast is unstable and the secondary electron

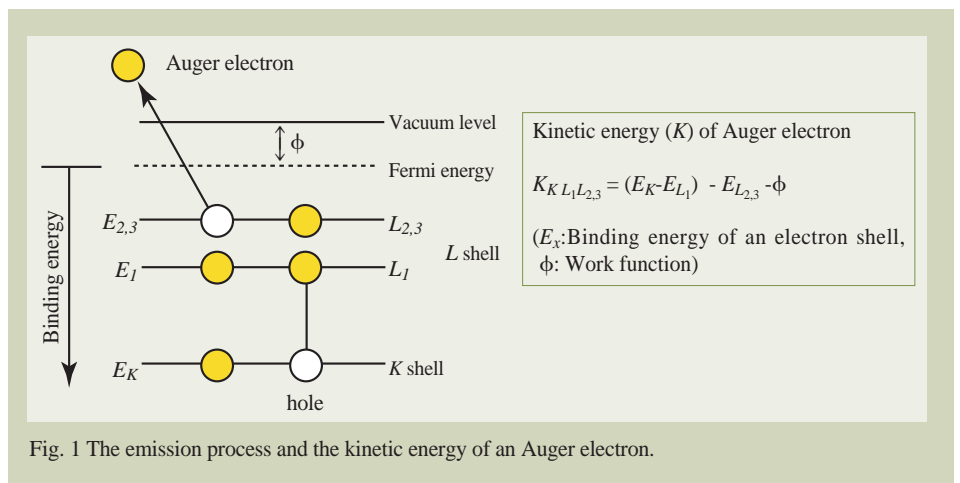


Fig. 1 The emission process and the kinetic energy of an Auger electron.

intensity fluctuates wildly. In order to analyze this phenomenon, the three situations are considered using the model as shown in Fig. 4.

When the electron beam enters the insulator sample surface, after the incident electrons generate secondary electrons including Auger electrons, they escape from the sample as backscattered electrons or remain inside the sample as they are. Let the charge remained on the sample surface be Q_S as shown in Fig. 4, the following equation holds.

$$Q_S = Q_I - (Q_E + Q_D) \dots\dots(3)$$

where, Q_I is the charge entered into the sample as the incident electrons, Q_E is the charge escaped from the sample surface as the secondary and backscattered electrons, and Q_D is the charge leaked out of the sample due to the diffusion of the electrons. On this occasion, if the potential V_S on the insulator sample surface is assumed to form a capacitor between the insulator sample surface and the sample holder in the reverse side, it is expressed by the following equation.

$$V_S = \frac{Q_S}{C_S} = \frac{1}{C_S} \{Q_I - (Q_E + Q_D)\} \dots\dots(4)$$

From Eq. (4), it is found that the surface potential V_S is proportional to Q_S , and that the sign becomes either positive or negative depending on the charge difference between $|Q_I|$ and $|Q_E + Q_D|$. Next, the difference of each parameter according to the difference of Q_S is qualitatively shown in Fig. 5 based on the present model.

Fig. 5 shows three cases: (i) when the surface potential is positive, (ii) when the surface potential becomes negative, and (iii) when the charge becomes too large for the electron beam to enter into the sample surface because the surface potential becomes nearly equal to the accelerating voltage of the electron beam. The reason why the contrast of the secondary electron image becomes unstable or the electron intensity fluctuates wildly to result in obtaining an image that is entirely unmatched with the actual surface shape is mainly because the phenomenon of (iii) occurs. In the case of (iii), the Auger analysis is not possible because the electrons cannot enter into the sample surface.

In the second case (ii), however, you can observe a secondary electron image and measure an Auger spectrum at the beginning because the charge is small compared with the case (iii); Usually, this situation is not stable. As long as the incident charge meets the condition $|Q_I| > |Q_E + Q_D|$, the surface charge increases and eventually results in the state (iii), making it impossible to perform the stable analysis.

As a conclusion, only if the surface potential satisfies $V_S > 0$ as in the case of (i), where the condition $|Q_I| < |Q_E + Q_D|$ is satisfied, the electron beam can always enter the sample surface, making it possible to constantly perform the Auger analysis. If you observe an insulator sample itself or even a conductor sample when it is electrically isolated, you cannot perform a highly reliable measurement unless you create the state in which the surface potential becomes positive as in the case (i) using some method and then perform the Auger analysis. Specifically, to

increase the escaped charge (Q_E) due to the secondary and backscattered electrons, you use the "Sample tilt method", and to increase the leaked charge (Q_D) due to the diffusion, you only apply the "Charge suppression method using the neutralizer gun." The details of these methods will be explained in the later sections.

A problem of charging when detecting the Auger electrons

The previous section has described a problem that the electron beam cannot enter the sample surface, but this section describes a problem that becomes unable to detect Auger electrons after generating them due to the effect of charging.

Auger spectra measured of one of Au electrodes shown in Fig. 3 are shown in Fig. 6. It should be noted here that although Au peaks near 2000 eV in the spectrum before irradiating Ar ions can be normally detected, the electrons with lower energy than 300 eV cannot be detected. Because the Au peaks at the high energy near 2000 eV are detected at the same energy as those of the standard spectrum, it is found that the surface potential of the Au electrode becomes the earth potential (0 V) as described before. On the other hand, the reason why the electrons with the lower energy cannot be detected is that the glass epoxy resin around the Au electrode is charged and that the secondary and Auger electrons generated from the Au electrode surface do not normally enter the detector due to the deflection caused by the electric field generated by the

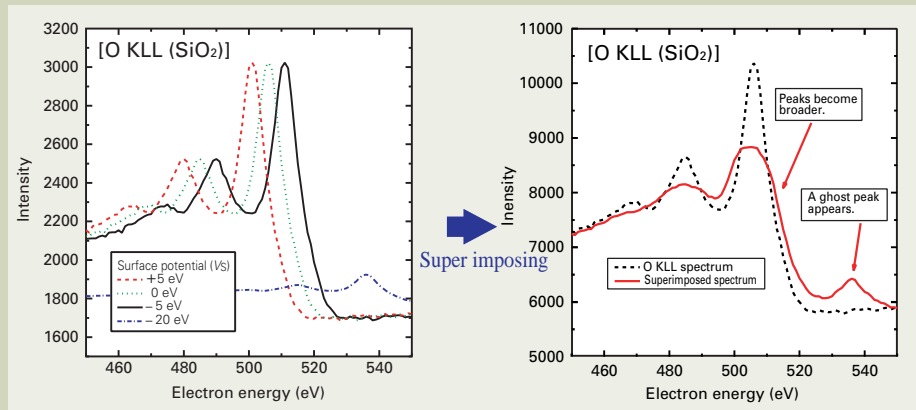


Fig. 2 O KLL (SiO₂) spectrum and its superimposed spectrum when the surface potential V_S is changed (+5, 0, -5, -20 V).

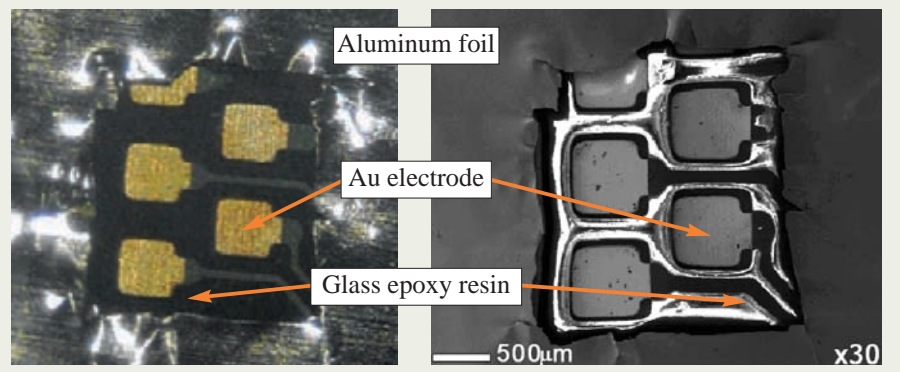


Fig. 3 An optical and a secondary electron image of a printed circuit board masked with an aluminum foil.

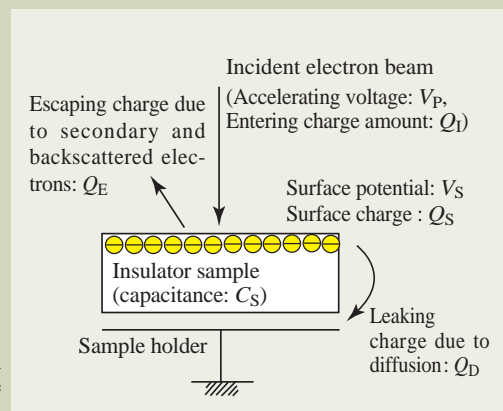


Fig. 4 Charging model when the electron beam is entered on the surface of the insulator sample.

charge accumulated on the glass epoxy resin surrounding the electrode. **Fig. 7** shows schematic diagrams illustrating the two possible cases: (i) when the glass epoxy resin around the electrode is negatively charged and (ii) when it is positively charged.

The diagram of the case (i) illustrates the circumstance in which the electron beam is irradiated on the glass epoxy resin surrounding the sample in order to confirm the analysis points on the sample and measure the secondary electron image, accumulating the electrons to negatively charge the glass epoxy resin. In this case, the negative electric field generated by the charging on the glass epoxy resin deflects the trajectory of the low energy electrons, causing a phenomenon that they do not enter the detector. For this reason, although the Au peaks at the high energy side as shown

in Fig. 6 are not affected by the charging on the glass epoxy resin, it is obtained an abnormal spectrum in which the low energy electrons are not detected.

On the other hand, the case of (ii) is often encountered when Ar ions in stead of electrons accumulate on the glass epoxy resin surrounding the sample to positively charge the glass epoxy resin because you increase the Ar ion current to irradiate the sample using the neutralizer too much. In this case, similarly, the positive electric field generated by the charging on the glass epoxy resin deflects the trajectory of the low energy electrons, causing a phenomenon that they do not enter the detector. Also in this case, although the Au peaks at the high energy side as shown in Fig. 6 are not affected by the charging on the glass epoxy resin, it

gives an abnormal spectrum in which the low energy electrons are not detected.

Method for Suppressing Charging in the Auger Analysis

Sample tilt method

Up to the previous section, it is shown that keeping the surface potential constant is necessary to measure the Auger electrons and that controlling the surrounding charging state is also necessary when detecting the Auger electrons. This section describes the sample tilt method that increases Q_E as a method for creating the state of the surface potential $V_S > 0$,

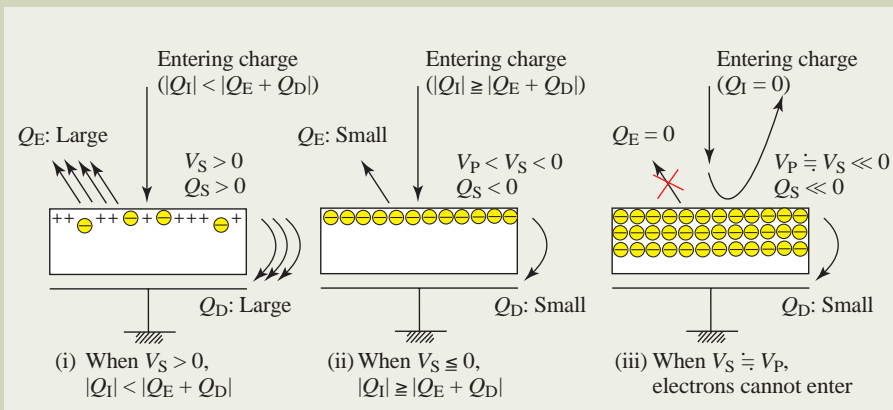


Fig. 5 Surface potential based on the charging model (Fig. 4) and each parameter.

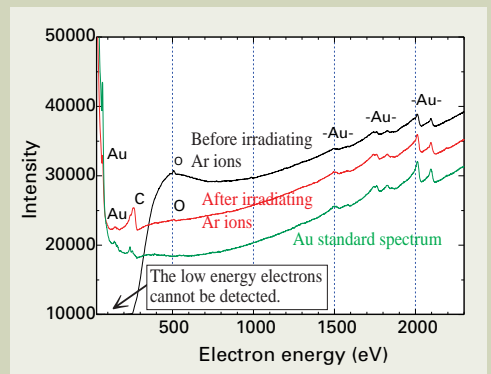


Fig. 6 Auger spectra of the Au electrode in Fig. 3. (Probe condition: 10 kV, 10 nA; sample tilt angle: 30°)

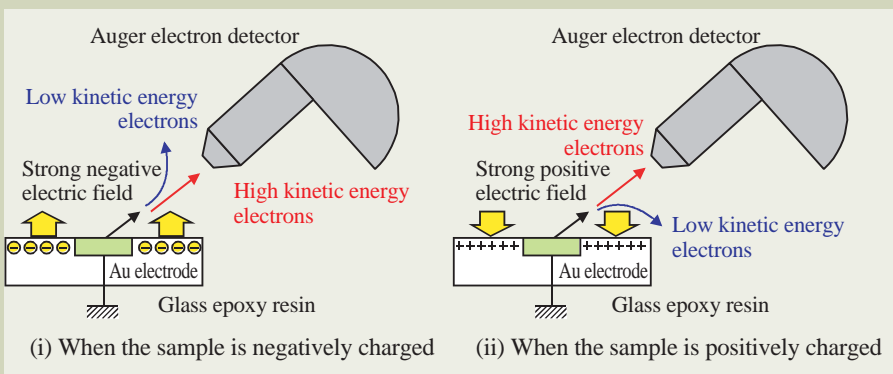


Fig. 7 Low kinetic energy electrons cannot be detected when insulator around the analysis point is charged.

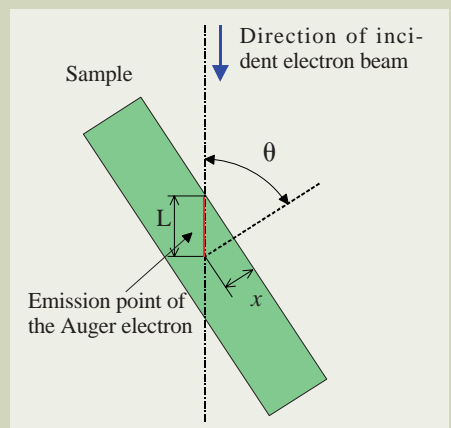


Fig. 8 Sample tilt angle θ from the direction of incident electron beam.

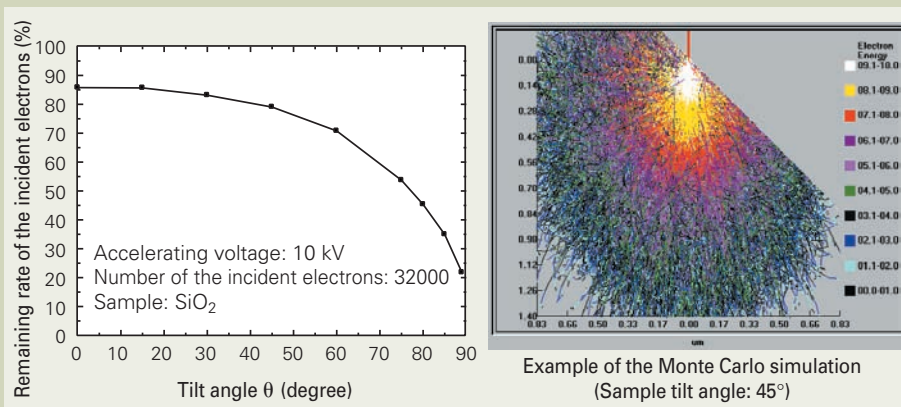


Fig. 9 Remaining rate of the incident electrons when they are entered at the accelerating voltage of 10 kV on the SiO_2 sample.

as in the case (i) in Fig. 5.

If you tilt the sample in the Auger analysis, the emission yield of secondary electrons increases because the incident angle of the electron beam becomes shallow and the region to excite the secondary electrons comes closer to the sample surface. **Fig. 8** shows the relation between the sample tilt angle θ and the incident angle of the electron beam.

When the incident direction of the electron beam is tilted by θ from the vertical direction of the sample, suppose that secondary electrons are generated along the length L as shown in Fig. 8. Supposing that the secondary electrons generated at each point along the length L are absorbed until they escape from the sample surface, the number of the secondary electrons generated from the sample surface is expressed as in Eq. (5). From this equation, it is found that the amount of the generated secondary electrons increases roughly in proportion to $1/\cos\theta$ as you increase the sample tilt angle [1]. Therefore, if you simply tilt the sample, the secondary electrons are generated in larger numbers, enabling you to make the surface potential positive as a result.

$$N = \int_0^{\infty} n e^{-kx} dL = \int_0^{\infty} n e^{-kL \cos\theta} dL = \frac{n}{k} \frac{1}{\cos\theta} \quad \dots (5)$$

- N : The number of secondary electrons generated from the sample surface
- n : The number of secondary electrons generated per unit length
- k : Attenuation coefficient
- x : Distance from the emission point of secondary electrons to the surface ($x = L \cdot \cos\theta$)

When you tilt the sample, not only the secondary electrons are generated in larger numbers, but also you can reduce the charge. **Figure 9** shows the remaining rate of the incident electrons inside the sample obtained from the Monte Carlo simulation.

It is found in Fig. 9 that the amount of electrons escaping from the sample as the backscattered electrons among the incident electrons increases and the amount of electrons remained inside the sample decreases as the sample tilt angle increases. In the case of the insulator sample, the large remaining rate of the incident electrons shows that the sample is strongly charged, and the larger you make the sample tilt angle, the smaller the remaining rate of the incident electrons and the smaller the charge on the sample surface.

As described above, if you tilt the sample, the generated secondary electrons increase and the amount of the incident electrons remaining inside the sample decreases; so if you tilt the sample more than a certain angle, the emission amount of the secondary electrons exceeds the remaining amount of the incident electrons, resulting the sample surface charged positively. This is the method for suppressing charging by the sample tilt method.

Figure 10 shows the secondary electron images of the kapton surface at three sample tilt angles, and **Figure 11** shows the Auger spectra of the sample surfaces. It is found that although unstable contrast and intensity variation characteristic of charging appear up to the tilt angle 60° , at the tilt angle 75° , a relatively stable secondary electron image and the normal Auger spectrum can be obtained.

Charging suppression method using the neutralizer gun

A charging suppression method using the neutralizer gun is a method for suppressing charging produced on the sample surface by irradiating the positively charged low energy (about 10 to 50 eV) Ar ions on the surface of the insulator sample. **Fig. 12** shows the schematic diagram.

Owing to the electron beam irradiated on the insulator sample to confirm the analysis position, charging due to electrons on the insulator surface occurs to produce negative surface

potential. If you irradiate low energy Ar ions on this charged surface, even if it is non-uniformly charged, the Ar ions are attracted in proportion to charge and the charging on the insulator surface is suppressed uniformly. Here, the point to notice is that the beam diameter of the Ar ion beam employed in this neutralization is 50 thousand times larger than that of the electron beam; and even if their beam currents are the same, the current densities are entirely different, so the Ar ion beam cannot suppress the charging at the position just on which the electron beam is irradiated. The purpose of the neutralization is solely to

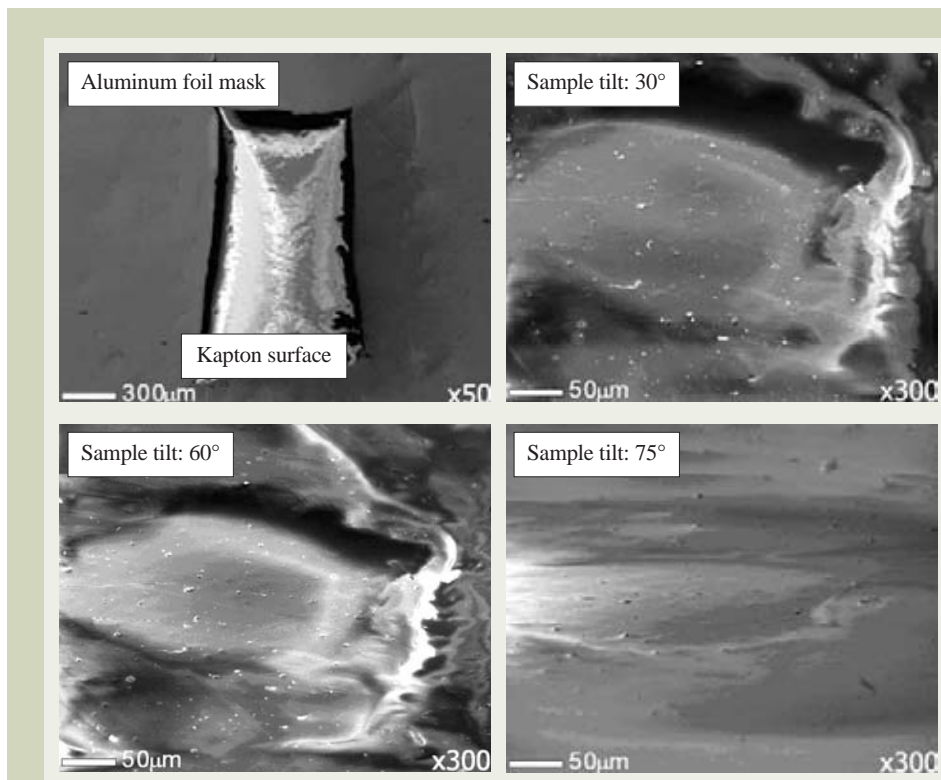


Fig. 10 Sample tilt angles and the appearances of the secondary electron images of the kapton surface. (Probe condition: 5 kV, 5 nA; neutralizer gun ON: 20 eV)

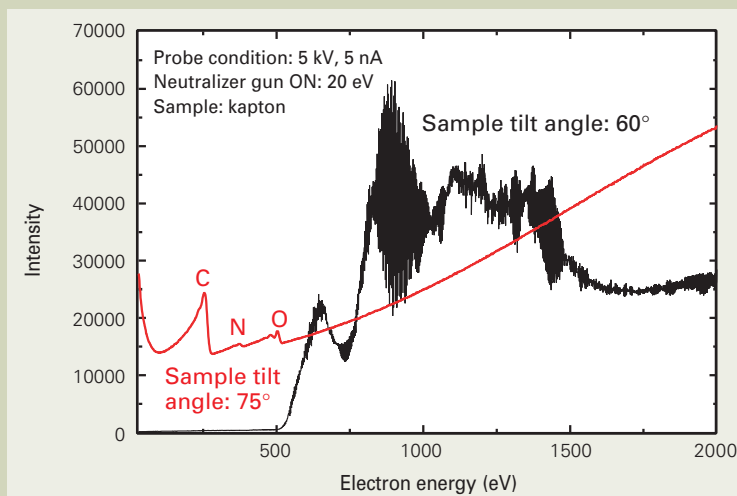


Fig. 11 Auger spectra of the kapton surface in Fig. 10. (Probe condition: 5 kV, 5 nA; neutralizer gun ON: 20 eV)

act Ar ions for the circumference around the analysis position to suppress the surrounding non-uniform charging [2].

In addition, the Ar ions have a role to absorb and diffuse the electrons, which are hard to diffuse and disappear inside the sample, on the sample surface by appropriately distributing on the charged sample surface. In other words, this low-speed Ar ion irradiation method corresponds to a method for increasing the amount of Q_D to create the state of the surface potential $V_S > 0$, as in the case (i) in Fig. 5, and has a large role to alleviate the charging phenomenon as shown in Fig. 13.

Confirming the charging state using the Auger spectrum

Although the charging on the sample is suppressed using two methods: "Sample tilt method" and "Charging suppression method using the neutralizer gun," you can judge whether the charge suppression is sufficient or insufficient from the Auger spectrum. Fig. 14 shows the Auger spectrum of the ungrounded electrode surface, and Fig. 15 shows the Auger spectrum of the grounded electrode surface. Looking at Fig. 14, it is found that all Au peaks in the spectrum of the ungrounded

electrode surface are shifted forward higher energy and do not appear at their original positions. This is because the gold electrode is negatively charged by the electron beam, causing a negative surface potential and all the secondary electrons generated there are measured at higher energy by the surface potential according to Eq. (2).

As described above, if you continue to enter the electron beam on the condition where the surface potential is negative, the surface potential gradually grows in the negative side and does not also remain stable so that you cannot measure a reproducible spectrum. In this way, if a negative surface potential is formed on the sample surface, you need to adjust the measurement condition by applying the sample tilt method, decreasing the accelerating voltage, and performing other methods so that the Au peaks of the measurement target surely become the shifted states (positive surface potentials) to the low energy side than the original energy values.

On the other hand, as shown in Fig. 15, for the Auger spectrum of the grounded electrode surface, all Au peaks are measured at normal positions irrespective of the condition where the neutralizer gun is on or off, revealing that the gold electrode surface is the earth potential. In addition, by turning on the neutralizer gun, the charging on the glass epoxy resin surrounding the Au electrode disappears and the normal Auger spectrum is obtained. When you measure an Au electrode like this occasion, you can judge whether the Au electrode is grounded or not from the information that whether all the Auger peaks are detected at the original peak positions or not.

Concluding Remarks

In the Auger analysis, from the feature of conducting the element analysis at a few nm from the surface, you cannot use the charge prevention processing by the surface conductor coating that is generally employed in the SEM and EPMA. In addition, in the Auger analysis, because the incident probe is electrons and the detection signal is also electrons, if the sample is charged even a little, the spectrum deforms, making it difficult to analyze the sample. It is shown, however, that if you understand what happens on the sample surface and properly deal with the problem, you can perform the Auger analysis. For example, the problem that you cannot analyze an electrode on a printed circuit board is often caused by the fact that the Au electrode of the measurement target is not grounded even while you have placed too much trust in the charging suppression method using the neutralizer gun. We hope you find the methods presented in this article informative.

References

- [1] K. Tsutsumi, Y. Nagasawa, and T. Tazawa, "Auger Analysis Using Low Angle Incident Electrons", *JEOL News*, **42E**, No.1, 40, (2007).
- [2] K. Tsutsumi, T. Suzuki, and Y. Nagasawa, "Effective Methods to Prevent Charging in Auger Electron Spectroscopy", *JEOL News*, **36E**, No.1, 66, (2001).

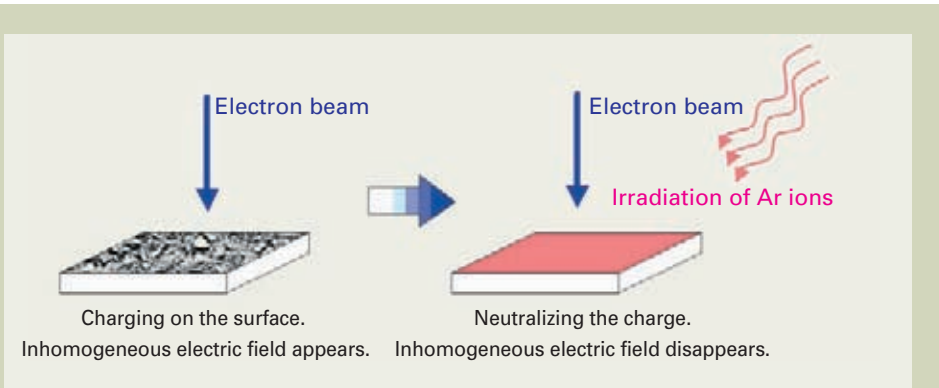


Fig. 12 Schematic diagram of a suppression method of charging using Ar ions.

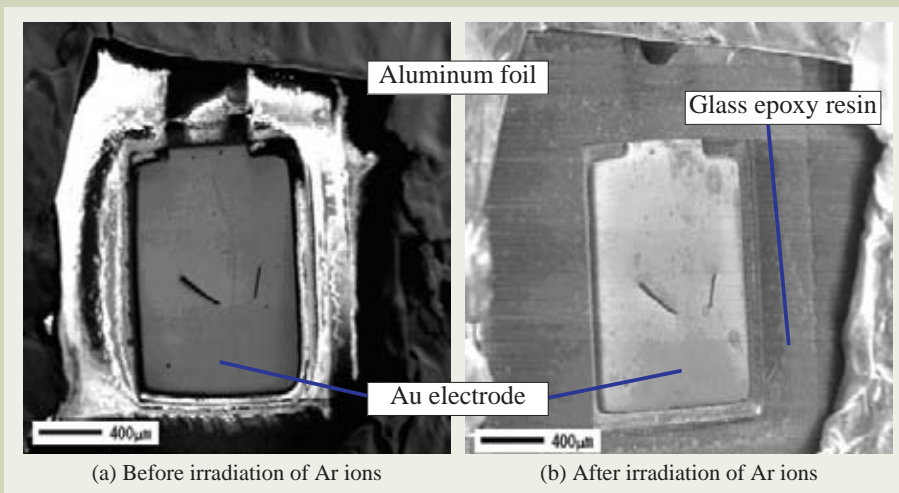


Fig. 13 Variation of the secondary electron images before and after the neutralization process in the Au electrode. (Probe condition: 10 kV, 10 nA; sample tilt angle: 45°)

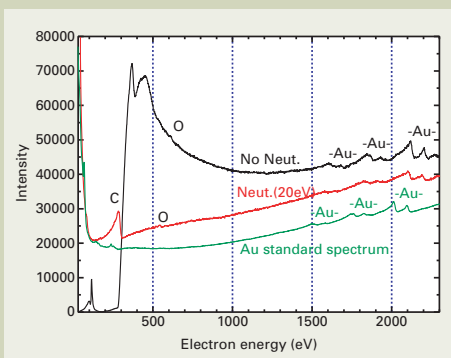


Fig. 14 Auger spectra of the ungrounded Au electrode surface. (Probe condition: 10 kV, 10 nA; sample tilt angle: 30°)

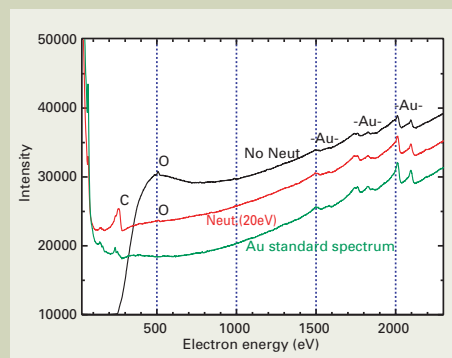


Fig. 15 Auger spectra of the grounded Au electrode surface. (Probe condition: 10 kV, 10 nA; sample tilt angle: 30°)



Certain products in this brochure are controlled under the "Foreign Exchange and Foreign Trade Law" of Japan in compliance with international security export control. JEOL Ltd. must provide the Japanese Government with "End-user's Statement of Assurance" and "End-use Certificate" in order to obtain the export license needed for export from Japan. If the product to be exported is in this category, the end user will be asked to fill in these certificate forms.

JEOL JEOL Ltd.

1-2 Musashino 3-chome Akishima Tokyo 196-8558 Japan Sales Division Telephone:+81-42-528-3381 Facsimile:+81-528-3386

<http://www.jeol.com/>

ARGENTINA
COASIN S.A.C.I.J.F.
Virrey del Pino 4071,
1430 Buenos Aires
Argentina
Telephone: 54-11-4552-3185
Facsimile: 54-11-4555-3321

AUSTRALIA & NEW ZEALAND
JEOL(AUSTRALASIA) Pty.Ltd.
Suite 1, L2 18 Aquatic Drive
- Frenchs Forest NSW 2086
Australia
Telephone: 61-2-9451-3855
Facsimile: 61-2-9451-3822

AUSTRIA
LABCO GmbH
Dr.-Tittremmel-Gasse 8
A-3013 Pressbaum, Austria
Telephone: 43-2233-53838
Facsimile: 43-2233-53176

BANGLADESH
A.G. CHOWDHURY SCIENCE & SYNERGY PVT. LTD.
House No. 12, Road No. 5A
Sector No. 11, Uttara Dhaka - 1230
Bangladesh
Telephone: 880-2-9980790, 8953450, 8953501
Facsimile: 880-2-8854428

BELGIUM
JEOL (EUROPE) B.V.
Planet II, Gebouw B
Leuvensesteenweg 542,
B-1930 Zaventem
Belgium
Telephone: 32-2-720-0560
Facsimile: 32-2-720-6134

BRAZIL
JEOL Brasil Instrumentos Cientificos Ltda.
Av. Itaberaba, 3563
02739-000 Sao Paulo, SP Brazil
Telephone: 55-11-3983 8144
Facsimile: 55-11-3983 8140

CANADA
JEOL CANADA, INC.
(Represented by Soquelec, Ltd.)
5757 Cavendish Boulevard, Suite 540,
Montreal, Quebec H4W 2W8, Canada
Telephone: 1-514-482-6427
Facsimile: 1-514-482-1929

CHILE
TECSIS LTDA.
Avenida Kennedy 5454 - Piso 5
Vitacura, Santiago, Chile
Telephone: 56-2-401-8520
Facsimile: 56-2-410-8541

CHINA
JEOL LTD., BEIJING OFFICE
Room B1110/11, Wantong New World Plaza
No. 2 Fuchengmenwai Street, Xicheng District,
Beijing 100037, P.R.China
Telephone: 86-10-6804-6321/6322/6323
Facsimile: 86-10-6804-6324

JEOL LTD., SHANGHAI OFFICE
Shanghai Equatorial Hotel Office Building 803,
65 Yanan Road West, Shanghai 200040, P.R. China
Telephone: 86-21-6248-4868/4487/4537/4404
Facsimile: 86-21-6248-4075

JEOL LTD., GUANG ZHOU OFFICE
N3104, World Trade Center Building
371-375, Huan Shi East-Road, Guang Zhou,
510095, P.R.China
Telephone: 86-20-8778-7848
Facsimile: 86-20-8778-4268

JEOL LTD., WUHAN OFFICE
Room 3216, World Trading Bldg.
686 Jiefang Street, Hankou, Wuhan, Hubei 430032
P.R.China
Telephone: 86-27-8544-8953
Facsimile: 86-27-8544-8695

JEOL LTD., CHENGDU OFFICE
1807A Zongfu Building,
NO. 45 Zhongfu Road, Chengdu, Sichuan, 610016
P.R. China
Telephone: 86-28-86622554
Facsimile: 86-28-86622564

CYPRUS
JEOL (EUROPE) SAS
Espace Claude Monet, 1 Allee de Giverny
78290, Croissy-sur-Seine, France
Telephone: 33-13015-3737
Facsimile: 33-13015-3747

EGYPT
JEOL SERVICE BUREAU
3rd Fl. Nile Center Bldg., Nawal Street,
Dokki, (Cairo), Egypt
Telephone: 20-2-3335-7220
Facsimile: 20-2-3338-4186

FRANCE
JEOL (EUROPE) SAS
Espace Claude Monet, 1 Allee de Giverny
78290, Croissy-sur-Seine, France
Telephone: 33-13015-3737
Facsimile: 33-13015-3747

GERMANY
JEOL (GERMANY) GmbH
Oskar-Von-Miller-Strasse 1a, 85386
Eching, Germany
Telephone: 49-8165-77346
Facsimile: 49-8165-77512

GREAT BRITAIN & IRELAND
JEOL (U.K.) LTD.
JEOL House, Silver Court, Watchmead,
Welwyn Garden City, Herts AL7 1LT, U.K.
Telephone: 44-1707-377117
Facsimile: 44-1707-373254

GREECE
N. ASTERIADIS S.A.
56-58 S. Trikoupi Str. P.O. Box 26140
GR-10022, Athens, Greece
Telephone: 30-1-823-5383
Facsimile: 30-1-823-9567

HONG KONG
FARMING LTD.
Unit 1009, 10/F, MLC Millennia Plaza
663 King's Road, North Point, Hong Kong
Telephone: 852-2815-7299
Facsimile: 852-2581-4635

INDIA
BLUE STAR LTD. (HQ: Mumbai)
Analytical Instrments Department,
Sahas' 414/2 Veer Savarkar Marg
Prabhadey Mumbai 400 025, India
Telephone: 91-22-6666-4000
Facsimile: 91-22-6666-4001

BLUE STAR LTD. (Delhi)
Analytical Instruments Department,
E-44/12 Okhla Industrial Area,
Phase-II, New Delhi 110 020, India
Telephone: 91-11-4149-4000
Facsimile: 91-11-4149-4005

BLUE STAR LTD. (Calcutta)
Analytical Instruments Department,
7, Hare Street Calcutta 700 001, India
Telephone: 91-33-2213-4133
Facsimile: 91-33-2213-4102

BLUE STAR LTD. (Chennai)
Analytical Instruments Department,
No. 46, Garuda Building,
Cathedral Road, Chennai 600 086, India
Telephone: 91-44-4244-4000
Facsimile: 91-44-4244-4190

INDONESIA
PT. TEKNOLABindo Penta Perkasa
Komplek Gading Bukit Indah Blok I/11
Jl. Bukit Gading Raya Kelapa Gading Permai,
Jakarta 14240, Indonesia
Telephone: 62-21-45847057/58/59
Facsimile: 62-21-45842729

ITALY
JEOL (ITALIA) S.p.A.
Centro Direzionale Green Office
Via dei Tulipani, 1
20090 Pieve Emanuele (MI) Italy
Telephone: 39-02-9041431
Facsimile: 39-02-90414343

KOREA
JEOL KOREA LTD.
Dongwoo Bldg. 7F, 458-5, Gil-Dong,
Gangdong-Gu, Seoul, 134-010, Korea
Telephone: 82-2-511-5501
Facsimile: 82-2-511-2635

KUWAIT
YIACO MEDICAL Co.K.S.C.C.
P.O. Box 435
13005-Safat, Kuwait
Telephone: 965-24842322/24814358
Facsimile: 965-24844954/24836812

MALAYSIA
JEOL(MALAYSIA) SDN.BHD.(359011-M)
205, Block A, Mezzanine Floor,
Keliana Business Center
97, Jalan SS 7/2, Kelana Jaya,
47301 Petaling Jaya, Selangor, Malaysia
Telephone: 60-3-7492-7722
Facsimile: 60-3-7492-7723

MEXICO
JEOL DE MEXICO S.A. DE C.V.
Av. Amsterdam #46 DEPS. 402
Col Hipodromo, 06100, Mexico D.F.
Mexico
Telephone: 52-5-55-211-4511
Facsimile: 52-5-55-211-0720

PAKISTAN (Karachi)
ANALYTICAL MEASURING SYSTEM (PVT) LTD.(AMS LTD.)
14-C Main Sehar Commercial Avenue Lane 4,
Khayaban-e-Sehar
D.H.A-VII, Karachi-75500, Pakistan
Telephone: 92-21-35345581/35340477/35346057-8
Facsimile: 92-21-35345582

PANAMA
PROMED S.A.
Parque Industrial Costa del Este
Urbanizacion Costa del Este
Apartado 0816-01755, Panama, Panama
Telephone: 507-303-3100
Facsimile: 507-303-3115

PHILIPPINES
PHILAB INDUSTRIES INC.
7487 Bagtikan Street, SAV Makati,
1203 Metro, Manila Philippines
Telephone: 63-2-898-7218
Facsimile: 63-2-897-7732

PORTUGAL
Izassa Portugal Lda.
R. do Proletariado, 1
2790-138 CARNAXIDE, Portugal
Telephone: 351-21-424-73-00
Facsimile: 351-21-418-60-20

RUSSIA
JEOL LTD. Moscow Office
Krasnoprotarskaya Street, 16,
Bld. 2, Entrance 5, 127473, Moscow,
Russian Federation
Telephone: 7-495-748-7791
Facsimile: 7-495-748-7793

SAUDI ARABIA
ABDULREHMAN ALGOSAIBI G.T.C. (Riyadh)
King Abdulaziz Avenue,
P.O. Box 215, Riyadh 11411, Saudi Arabia
Telephone: 7-495-748-7791
Facsimile: 7-495-748-7793

SCANDINAVIA
JEOL (SKANDINAVISKA) A.B.
Hammarbacken 6A, Box 716, 191 27 Sollentuna
Sweden
Telephone: 46-8-28-2800
Facsimile: 46-8-29-1647

SERVICE & INFORMATION OFFICE
JEOL NORWAY
Ole Deviks vei 28, N-0614 Oslo, Norway
Telephone: 47-2-2-64-7930
Facsimile: 47-2-2-65-0619

JEOL FINLAND
Ylakaupinkuja 2, FIN-02360 Espoo, Finland
Telephone: 358-9-8129-0350
Facsimile: 358-9-8129-0351

JEOL DENMARK
Naverland 2, DK-2600 Glostrup, Denmark
Telephone: 45-4345-3434
Facsimile: 45-4345-3433

SINGAPORE
JEOL ASIA PTE. LTD.
2 Corporation Road #01-12 Corporation Place
Singapore 618494
Telephone: 65-6565-9989
Facsimile: 65-6565-7552

SOUTH AFRICA
ADI Scientific (Pty) Ltd.
370 Angus Crescent,
Northlands Business Park, 29 Newmarket Road
Northriding, Ranburg, Republic of South Africa
Telephone: 27-11-462-1363
Facsimile: 27-11-462-1466

SPAIN
IZASA S.A.
Argoneses, 13, 28100 Alcobendas,
(Poligono Industrial), Madrid, Spain
Telephone: 34-91-863-0500
Facsimile: 34-91-863-0545

SWITZERLAND
JEOL (GERMANY) GmbH
Oskar-Von-Miller Strasse 1,
85386 Eching, Germany
Telephone: 49-8165-77346
Facsimile: 49-8165-77512

TAIWAN
JIE DOING CO., LTD.
7F, 112, Chung Hsiao East Road,
Section 1, Taipei, Taiwan 10023
Republic of China
Telephone: 886-2-2395-2978
Facsimile: 886-2-2322-4655

For Semiconductor Products:
JEOL TAIWAN SEMICONDUCTORS LTD.
11F-1, No. 346, Pei-Da Road, Hsin-Chu City 300,
Taiwan, Republic of China
Telephone: 886-3-523-8490
Facsimile: 886-3-523-8503

THAILAND
BECTHAI BANGKOK EQUIPMENT & CHEMICAL CO., Ltd.
300 Phaholyothin Rd. Phayathai, Bangkok 10400,
Thailand
Telephone: 66-2-615-2929
Facsimile: 66-2-615-2350/2351

THE NETHERLANDS
JEOL (EUROPE) B.V.
Liweweg 4, NL-2153 PH Nieuw-Vennep,
The Netherlands
Telephone: 31-252-623500
Facsimile: 31-252-623501

TURKEY
TEKSER LTD.STI.
Acibadem Cad. Erdem Sok. N° 6/1
34660, Uskudar, Istanbul, Turkey
Telephone: 90-216-3274041
Facsimile: 90-216-3274046

UAE
BUSINESS COMMUNICATIONS LLC. (Abu Dhabi)
P.O. Box 2534, Abu Dhabi UAE
Telephone: 971-2-6348495
Facsimile: 971-2-6316465

BUSINESS COMMUNICATIONS LLC. (Dubai)
P.O. Box 233, Dubai, UAE
Telephone: 971-4-2220186
Facsimile: 971-4-2236193

USA
JEOL USA, INC.
11 Dearborn Road, Peabody, MA 01960, U.S.A.
Telephone: 1-978-535-5900
Facsimile: 1-978-536-2205/2206

JEOL USA, INC. WEST OFFICE
5653 Stoneridge Drive Suite #110
Pleasanton, CA 94588, U.S.A.
Telephone: 1-925-737-1740
Facsimile: 1-925-737-1749

VENEZUELA
GOMSA Service and Supply C.A.
Urbanizacion Montalban III
- Residencias Don Andres - Piso 7 - Apartamento 74
Avenida 3, entre calles 7 y 6
Montalban, Caracas, Venezuela
Telephone: 58-212-443-4342
Facsimile: 58-212-443-4342

VIETNAM
TECHNICAL MATERIALS AND RESOURCES IMPORT-EXPORT JOINT STOCK
COMPANY(REXCO)
Hanoi Branch,
No. 13-Lot 12 Trung Yen, Trung Hoa Street, Cau Giay Dist, Hanoi, Vietnam
Telephone: 84-4-562-0516, 17/562-0535
Facsimile: 84-4-853-2511